ABSTRACT

Title of Document: PROBING ATMOSPHERIC AEROSOL AND GAS PROPERTIES WITH PHOTOACOUSTIC SPECTROSCOPY

Pedro Antonio Bueno, Jr., Doctor of Philosophy, 2011

Directed By:
Professor, Michael R. Zachariah,
Department of Mechanical Engineering and Chemistry
Professor, Russell R. Dickerson,
Department of Atmospheric and Oceanic Science and Chemistry

Absorption by atmospheric aerosols is the wild card for global climate change. Issues regarding atmospheric gases and aerosols have been at the forefront and the work presented within is directed at those issues. Specifically, work has been performed in order to help understand the issue of absorption in the atmosphere and whether this contributes towards positive forcing or warming of the atmosphere. In the process of conducting this research a custom, first-principles photoacoustic spectrometer was improved, calibrated and used extensively in order to obtain knowledge of the interaction of light with atmospherically relevant gases and make the first measurements of absorbing aerosols. The absorption cross-section of uncoated and coated soot was measured and quantified and found to be consistent

with other work where amplifications on the order of nearly 100% were observed with uncertainty levels much lower than previously reported. Soot was also found to be optically thin where the total mass of the soot contributes to the absorption. Consequential to the soot work, the photoacoustic spectrometer developed to measure the absorption was utilized as a high precision greenhouse gas sensor. The photoacoustic spectrometer was found to produce results on the absorption of CO_2 to within 3% of the theoretically predicted line profile Moreover, the photoacoustic spectrometer was used to determine measurable coating thicknesses of less than 10 nanometers on 100 nm soot particles.

PROBING ATMOSPHERIC AEROSOL AND GAS PROPERTIES WITH PHOTOACOUSTIC SPECTROSCOPY

By

Pedro Antonio Bueno, Jr.

Dissertation submitted to the Faculty of the Graduate School of the
University of Maryland, College Park, in partial fulfillment
of the requirements for the degree of
Doctor of Philosophy
2011

Advisory Committee:
Professor Michael R. Zachariah Chair
Professor Russell R. Dickerson Co-Chair
Professor John M. Ondov
Professor Neil V. Blough
Visiting Professor George W. Mulholland
Professor Sheryl H. Ehrman (Dean's Representative)

Foreword

The research began several years ago with the infrastructure of the main experiment. The development of custom-built differential mobility analyzers as well as coating apparatus took several years to properly understand and control the ebbs and flows of the system. Understanding pressure gradients, flow trains, how to cut stainless steel tubing, etc. took years to properly get a handle on. After the plumbing and DMAs were built, soot generation was the issue. Learning to properly handle the soot and move the soot took time and was finally mastered. Coating then became the issue. Several iterations of the coating apparatus appeared over the years and finally, in the summer of 2009, a final design was agreed upon. That design is detailed in Chapter 3. The final step was the analysis portion. This was the key to the puzzle.

As with most situations in life, "you can't always get what you want, but if you try sometimes, you might find, you get what you need" (Rolling Stones et al 1969). Acquiring an analysis instrument was difficult, but in the fall of 2007 collaboration with Dr. Joseph Hodges and Dr. Keith Gillis at the National Institute of Standards and Technology, Gaithersburg, MD was developed. Drs. Hodges and Gillis had built a first principles photoacoustic spectrometer and wanted to expand their work with gases to aerosols. This was a perfect opportunity for our expertise with aerosols to mesh with their expertise with photoacoustics. With the help of Dr. Daniel Havey, the PAS system was expanded and photoacoustics was found to be the perfect complement to the aerosols production that was developed over several years.

Dedication

I dedicate this work to the most important people in my life. Julia, my beautiful wife, Simon, my eldest son, Jude and Felix, my middle sons and to Violet, my daughter, this is for you. For no other reason would I undertake this toll, if not to make your lives a little better. I love you.

And to my mother, father, in-laws and family, this goes out to you as well. Your support and love made me the person I am. Thank you.

Acknowledgements

I would like to thank the support and mentorship from my advisors Professors Michael R. Zachariah and Russell R. Dickerson. I began at the University of Maryland as a student working for Russ, only knowing I wanted to do something that would help mankind. Atmospheric chemistry seemed like a good vehicle for this goal. Russ's direction and instruction helped me develop the critical thinking skills I would need to conduct my research and allowed me the creativity to keep my research interesting. In year 2 of my graduate career, Dr. Zachariah entered the picture as my co-advisor. Due to the nature of the work, I transitioned over to Dr. Zachariah's group in order to learn the skills necessary to build and conduct high quality aerosol research. Under the direction of both Drs. Dickerson and Zachariah, the two worlds of atmospheric chemistry and aerosol physics combined in order to produce the work detailed herein.

I would also like to thank Dr. George W. Mulholland for his extensive mentoring and dedication to making this work quality work. Dr. Mulholland was in no way required to spend the amount of time he did with me and I am forever grateful. Dr. Mulholland's tutelage and knowledge of smoke (i.e. soot) was indispensible and I can only say "Thank you George."

Furthermore, I would like to acknowledge and thank Drs. Joseph T. Hodges, Keith A. Gillis and Daniel K. Havey for their collaboration and accessibility to the breadth of their spectroscopic experience. Joe, Keith and Dan opened up a new world

to me, without them this work could never have been completed. Dan, not only were you my guide when learning photoacoustic spectroscopy, but you are my friend. I would also like to thank Dr. James Whetstone at the National Institute of Standards and Technology. His willingness to help me acquire the necessary to tools to complete my work will not be forgotten.

I would also like to acknowledge all the professors who took the time to teach me something I didn’t know (which is a lot). I may never take a class again, but the lessons learned will not be lost.

Professors John M. Ondov, Neil V. Blough and Sheryl H. Ehrman, thank you for serving on my committee and holding me to the standards by which the University of Maryland deems necessary to be awarded the degree of Doctorate of Philosophiae.

Thank you to my friends and colleagues at the University of Maryland and the National Institute of Standards and Technology. Your companionship has been invaluable.

And finally, I would like to acknowledge the Department of Energy’s National Institute for Global Environmental Change Prime Award # DE-FC02-03ER63613 for the financial support that made this research possible.

Table of Contents

List of Tables

List of Figures

Figure 3.12: Photograph of the photoacoustic cell used in these experiments.

Figure 3.14: Measured acoustic resonance (red line and markers) and fit (blue lines and markers) to complex resonance function corresponding to laboratory air at T = 300 K, p = 98.5 kPa. Fitted values include $f0$ = 1638.22 Hz and g = 29.2 Hz. Upper panel: u and v measurements (symbols) and fits (lines). Bottom panel: fit residuals for u and v components.[11]

Figure 4.1. A schematic of a simple PAS experiment using the NIST spectrometer is shown.

Figure 4.2. An acoustic resonance fit for CO_2 yielding f_0 = 1273.6 Hz and Q = 28.8 is presented. The complex resonance function $x+iy=\frac{-Af}{f^2-(f_r+ig_r\sqrt{\tilde{f}/f})^2}+B+C(f-\tilde{f})$ was fit to the data as described in Gillis *et al.*[11]

Figure 4.3. Power normalized Allan deviations (square root of the Allan variance[12]) are shown for absorption measurements at line center of the $^{P}P(9)$ transition at 13,091.710 cm^{-1} in the O_2 *A*-band at 300.0 K and 100.8 kPa (blue) and for 100 nm ± 1 nm soot particles at 100.3 kPa and 295.9 K (red). Measurements of the O_2 *A*-band utilized a 765 nm single-mode external cavity diode laser with peak-to-peak modulated power of ~ 3 mW; soot aerosol measurements utilized a 405 nm multimode diode laser with ~ 200 mW of peak-to-peak power. Instrumental detection limits for 60 s averaging times are 4×10^{-10} $W\cdot cm^{-1}$ for gases and 2×10^{-9} $W\cdot cm^{-1}$ for aerosols.

Figure 4.4. Differences between measured and modeled absorption coefficients for measurements of two CO_2 transitions within the $(30^01)\leftarrow(00^01)$ combination band are presented. Modeled absorption coefficients utilized Voigt profiles with the line parameters of Toth *et al.*[13] PAS measurements were made on humidified CO_2 at 298.9 K and 99.88 kPa with signal-to-noise ratios of ~1800:1 for 2 mW of peak-to-peak modulated laser power. Presented error bars correspond to relative combined standard uncertainties (outer bars) containing contributions from random components (inner bars) and systematic uncertainties in system constant,[11] temperature, pressure, and power.

Figure 4.6. Measured relative changes in absorption coefficient are presented for measurements of 150 nm and 200 nm soot particles coated with < 10 nm thick shells of dibutyl phthalate (DBP); this is the smallest amount we can currently apply. Presented uncertainties correspond to $\sigma\alpha_{measured}/\sqrt{n}$ where $\sigma\alpha_{measured}$ is the standard deviation of the measured absorption coefficient and n is the number of observations.

Figure 4.5. Measured PAS signals normalized for power and counts are shown for flowing samples of 100 nm ± 1 nm soot particles. A coincidence correction to measured particle concentrations was performed to account for particle shielding effects in a condensation particle counter by iteratively solving the equation $\frac{N_T}{N_M} = e^{(-N_T q t_c)}$ until results converged to better than 0.5%[14]; here N_T is the true particle concentration, N_M is the measured particle concentration, q is the volumetric flow rate, and t_c is the measurement time for a condensation particle counter. Our measured long-term (5 h) 1σ measurement precision is 1.5% despite dynamic soot particle number densities

Figure 4.7. Minimum detectable average DBP coating thickness on 100 nm soot particles as a function of peak-to-peak laser power is shown. "Current Data" point represents the typical operating conditions, ~60,000 particles-cm^3 and 0.2 W peak-to-peak power, utilized in the present work. Lorenz-Mie theory calculations for coated spheres were performed using the code of Bohren and Huffman.[15] We assumed $m_1 = 1.55 + 0.8i$ and $m_2=1.5 + 0i$ for the complex index of refraction for soot and DBP, respectively. Predicted absorption enhancements over a range of shell thicknesses were calculated for samples of 10^5, 10^3, and 10^1 particles·cm^{-3} and compared against our measured detection limit of $\alpha_{min}W_{PP} = 2\text{x}10^{-9}$ W·cm^{-1} for a 60 s averaging time.

Figure 5.1: Comparison of climate forcing from IPCC for several greenhouse components. Note that absorbing aerosols are lost within the total aerosol and the nearly 100 % uncertainty on the aerosol bar.

Figure 5.2: Transmission electron micrograph of a soot agglomerate denoting fractal structure of soot.

Figure 5.3: Possible mixing states of absorbing aerosols in the atmosphere as proposed by Jacobson 2003.

Figure 5.4: The SDAM and TDMA experimental set up as used in this study. Soot can follow two different paths after size selection with DMA_1. Soot can pass through a second aerosol neutralizer for uncoated measurements or can pass through the coating apparatus and then DMA_2 for PAS analysis. Both paths ultimately arrive at a CPC for counting. The SDMA experimental set up is the same with the exception of the second neutralizer and second DMA.

Figure 5.5: Particle distributions for 100 nm uncoated soot (solid thick line) and multiple representative coated soot distributions (dashed lines) during the SDMA mode. Each set of dashed lines is a different coating thickness for the same core size. Inset shows the full flame distribution measured using a single DMA.

Chapter 1: Introduction

1.1 Global Climate Change

1.1.1 Overview

The Earth's energy flow is a balance of shortwave solar energy impinging on the Earth's surface and consequential longwave reradiated energy leaving the Earth's surface. This balance has its natural ebbs and flows and is influenced by many factors such as cloud coverage, land types and human activity. Under normal conditions equilibrium exists between the energy in and the energy out. This balance affects and controls weather and climate. But when there is a perturbation, this equilibrium is shifted. Since the industrial revolution, human progress has been the largest perturbation to this energy balance[6].

The energy flow is typically estimated at two locations, the top of the atmosphere (TOA) and at the Earth's surface. These estimates are based on satellite measurements as well as ground-based measurements. At the TOA, the measurement of incoming shortwave radiation is based on the amount of energy incident on the TOA less the reflected shortwave energy (by clouds, for example). In order to maintain the total equilibrium, the incoming shortwave solar energy is balanced by the surface-atmosphere reradiated longwave energy. The solid Earth acts as a blackbody radiator where the energy absorbed is reradiated as long wave (thermal) energy. A blackbody radiator is a mass that radiates a maximum amount of energy per wavelength (λ) at a given temperature. This characteristic is independent of the make-up of the emitter. This energy output is a function of λ, absolute temperature and surface area of the emitter. The counter balance to this blackbody emission is that a blackbody also absorbs all energy that impinges on it. The solid Earth can be approximated as a classic blackbody radiator.

The energy that is reradiated by the Earth is then trapped by the atmospheric blanket surrounding the Earth. The atmosphere, comprised predominantly of N_2, O_2 and a myriad of other gases (e.g. CO_2, Ar, CH_4, H_20, O_3 etc.) traps much of the longwave radiation that the Earth re-emits. The atmosphere's ability to trap Earth's emitted energy creates an energy forcing. The forcing is defined as the difference in the flux of energy at the TOA with and without the greenhouse components. The greenhouse components are comprised of gases and particles that interact with the incoming and outgoing radiation. The greenhouse components have a tendency to trap longwave radiation emitted by the Earth and scatter or transmit the incoming solar radiation. This forcing, however, requires that there be a net zero energy flow at the TOA and at the Earth's surface. This trapped energy allows life to continue as understood. A cartoon of this balance is seen in Fig. 1.1, Trenberth *et al.*[5] have condensed the Earth's energy flow system into a succinct set of paths, incoming and outgoing.

Of notable importance in Fig. 1.1 is the net absorbed energy by the Earth. That net absorbed energy is 0.9 W/m^2 a positive value indicating the Earth is slowly warming. More energy is trapped in the atmosphere than is released. Whether this net increase over the last many years is due to a natural cycle or anthropogenic causes is not the issue explored in this work. What is explored is how the forcing described is affected by certain atmospheric components, which have increased in the last 150 years. An example of this increase can be seen in Fig. 1.2.

1.1.2 Atmospheric Forcing

Forcing, both positive (warming) and negative (cooling) are the instruments driving climate change. When the balance between the incoming and outgoing energy is shifted, a climate effect may be observed. This effect can be episodic, such as a volcanic eruption's impact on the aerosol content in the atmosphere, which typically has a negative forcing on the atmosphere since most of the aerosols are injected into the stratosphere where both the absorbing and scattering aerosols prevent the incoming solar energy from entering the troposphere. This is considered a temporary affect since the eruption time is finite as well as the amount of aerosol and gases emitted. In the case of anthropogenic emissions of gases and aerosols, the effect is not so temporal because the emissions are ongoing and the majority of the emissions has been in existence since the industrial revolution and is kept within the troposphere.

The most common example of climate forcing is that of CO_2 and the "Greenhouse Effect". When discussing the greenhouse effect, most typically, CO_2 comes to mind. What anthropogenic CO_2 does is thicken the blanket at the TOA. Carbon dioxide has the benefit of absorbing longwave radiation and keeps this thermal energy close to the Earth's surface. The downside to carbon dioxide's characteristic absorption spectrum is that if too much CO_2 is present, then too much thermal energy is absorbed and a net increase in the mean temperature occurs. While this is just one greenhouse constituent, it presents the clearest argument that anthropogenic emissions do indeed contribute to global climate change. Fig. 1.3

shows modeled results by Hansen et al 2005 for the case where the atmospheric CO_2 concentration ($[CO_2]$) is doubled over a period of 120 years and the effect of that doubling is noted for both the mean global temperature change (ΔT ºC) based on the initial $[CO_2]$ in 1880, and the impact on the net radiative forcing due to CO_2. In all cases, both the positive forcing (warming effect) and mean global temperature increase, and it is well known that the atmospheric CO_2 has increased since the late 1800's.[16]

Greenhouse aerosols, much like greenhouse gases, drive the climate forcing in the atmosphere. Because atmospheric aerosols are less ubiquitous than greenhouse gases, less is known about them because many of them are unique to their source and are often temporal. Moreover, the chemistry of the aerosols is so dynamic and complicated that mere observations and identification are difficult. Atmospheric aerosols have both natural and anthropogenic sources. As mentioned earlier, volcanic aerosol is a natural, but typically short-lived event and NaCl based aerosols are also natural and occur from sea spray. Anthropogenic aerosols have many different sources, including industry, biomass burning and fossil fuel use. The impact that atmospheric aerosols have on the climate and weather is under great scrutiny as of late. Many studies have taken place and are under way to attempt to quantify the impact of both scattering and absorbing aerosols.[17, 18, 19, 20, 21] This is a vast problem that requires many components in order to clarify the issues at hand. The work presented within attempts to contribute a small piece of quantified knowledge to the global climate change pie, so-to-speak.

1.2 Interaction of Light with Gases and Particles

The interplay between light and matter is the fundamental phenomenon occurring in the research presented within this dissertation. This subject matter has a very long and broad history and will be discussed for the systems specific to this work. Regardless of the matter in question, when light is incident upon matter that contains both positive and negative charges, the electric field found inside the matter is set in motion, oscillatory motion, to be precise. This oscillation corresponds to the electric field from the incident light. The electric charges in the matter are accelerated and consequently radiate electromagnetic radiation in all directions. This electromagnetic radiation or second stage radiation is the energy that is scattered or absorbed by matter as shown in Fig. 1.5. If the incident energy is reradiated without conversion, then the energy has been scattered. If the energy is transformed in some way, then some or all of that energy has been absorbed and is reradiated in a different form, such as thermal energy.

1.2.1 Atmospheric Gases

As mentioned earlier, life as we know it exists because of the energy flow from the sun to the Earth and back into space. It is not, however, as simple as that. How this energy, in the form of light, interacts with both the atmosphere and its content is critical in the manifestation of hospitable conditions for life. Atmospheric gases act to both protect us from and contain the energy from the sun. With respect to how these gases protect, one merely needs to discuss the ozone layer. This extremely thin layer of ozone in the stratosphere is effective at absorbing and preventing shortwave radiation (approximately 300 nm and less) from reaching the surface of the Earth.

Light in that wavelength range is harmful to the human condition as well as many ecosystems. Carbon dioxide, on the other hand, helps keep longwave radiation near the surface of the Earth to keep conditions a comfortable 300 K on average. But what exactly happens when a photon finds a gas molecule? What connection is made?

To treat this material to the level appropriate for the work presented, the molecules discussed can be considered simple harmonic oscillators with a single inherent oscillation frequency. The molecule is considered to consist of electrons bound by a much heavier nucleus. The connection between the electrons and the nuclei is like a spring with a spring constant that is related to the inherent oscillation frequency. When this electron-nucleus system is confronted by a wavelength of light of some angular frequency, the electron undergoes a harmonic oscillation in response to the oscillating electric field from the light. Because the nucleus is much more massive, it does not move and acts as a rigid base for the spring between itself and the electron to compress and expand. The displacement of the positively charged nucleus to the negatively charged electron creates a dipole. Or rather a dipole is induced. This oscillating dipole emits electromagnetic radiation. This is the basis for light scattering with a molecule. The issues explored in Chapter 4 delve into the interaction of light with CO_2. In this case, a line profile at a given temperature and pressure is measured in order to compare with theory. This line profile is a result of having a fine tuned light source of discrete energy, which resonates with the molecule in question. This is resonance scattering. The result of having a driving frequency very close to the resonance frequency is a line profile. Typically a Lorentz profile is observed which when integrated over all optical frequencies is related to the cross-section of the molecule. A Lorentz profile accounts for the presence of other molecules leading to pressure broadening. Pressure broadening is due to the collisions of molecules with other molecules and the exchange of energy between the molecules. Broadening due to the velocity and mass of the molecules is Doppler broadening and it can account for the direction in which the molecules are travelling when they encounter the incident light. In order to account for Doppler broadening and pressure broadening (Lorentz profile), a Voigt profile is used. A Voigt profile accounts for both pressure and Doppler broadening. These profiles are the theoretically predicted outcome of the gases to which the experimental results are compared and an example can be seen in Fig. 1.6.

These line profiles are of great interest and importance, because when combined with the concentration of the molecule in question describes the spectral dependence of how these gases will interact with light, i.e. how much will these gases scatter or absorb light, therefore, how much impact they will have in the atmosphere in terms of global climate change.

1.2.2 Atmospheric Particles

Like gases interact with solar radiation, so do particles in the atmosphere. There is a complexity to atmospheric particles, however, because they are more difficult to pinpoint in terms of sources, concentrations and chemistry. Having knowledge of how a specific particle interacts with incoming light is critical in understanding the Earth's energy flux. Like CO_2 blankets the top of the atmosphere and maintains the reradiated thermal energy near the surface of the Earth, particles can both scatter and absorb the light. Depending on the color and location of the particles, they can influence climate forcing both negatively (as in $(NH4)_2SO_4$) and positively (as in soot).

While the process of how light interacts with particles is the same at the molecular level as for gases, the difference is how the characteristic interaction of the light with the particles is defined. Typically, no line profile exists for particles, what is discussed is the absorption or scattering cross-section. This cross-section is a parameter that determines how much of the light impinging on the particle interacts with said particle.

Mie theory is applied to describe the interaction of light with small particles, paralleling the use of line profiles to describe molecular absorption discussed in the previous section. Mie theory described the intensity of the interaction of light with particles at specific indices of refraction and wavelengths. Mie theory is an exact solution to the theories put forth by Lorentz and Maxwell in the early 1900's for the interaction of an electromagnetic wave with a sphere. It requires the assumption that the particle in question is spherical and the index of refraction of that particle is known. This solution can be applied to any combination of radius and wavelength and requires the sum of an infinite series of expansions of the electromagnetic field equations, which will not be shown in this dissertation but can be found in Bohren and Huffman's text, *Absorption and Scatter of Light by Small Particles*.[15] The interplay between light and spherical particles is known, but for non-spherical particles, is not as well known. For the purposes of this work, a first order approximation is taken where all particles are considered spherical or a spherical surrogate is used when discussing Mie solutions. Mie solutions were calculated using a computer code found in Bohren's text[22], Appendix A and compiled into LabView software.

What both the line profile for gases and Mie theory for particles allow is the determination of the cross-section of the species. This cross-section when combined with the number concentration is an absolute measure of how an ensemble of particles or molecules of gas interact with the incident light. That is the focus of the research presented herein.

1.3 Figures

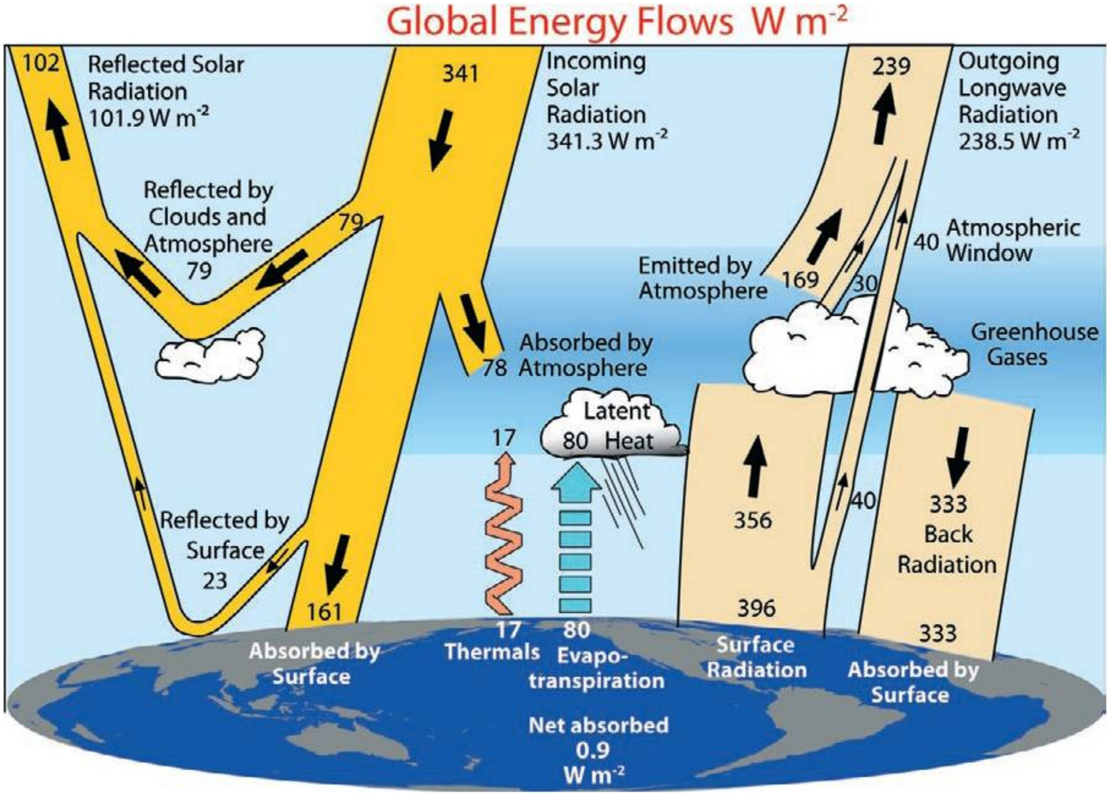

Figure 1.1: Taken directly from Trenberth et al.[5]. A summary of the Earth's energy budget showing a net positive forcing indicating global warming.

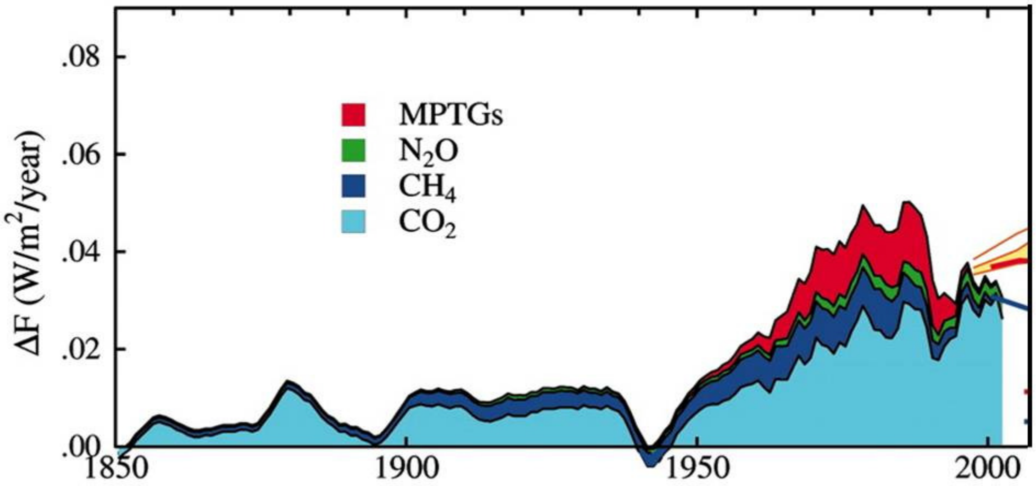

Figure 1.2: A 150 year trend in greenhouse gases (CO_2, CH_4, N_2O and Montreal Protocol trace gases (MPTGs)) showing a clear increase since the Industrial Revolution. Adapted from Hansen and Sato.[6].

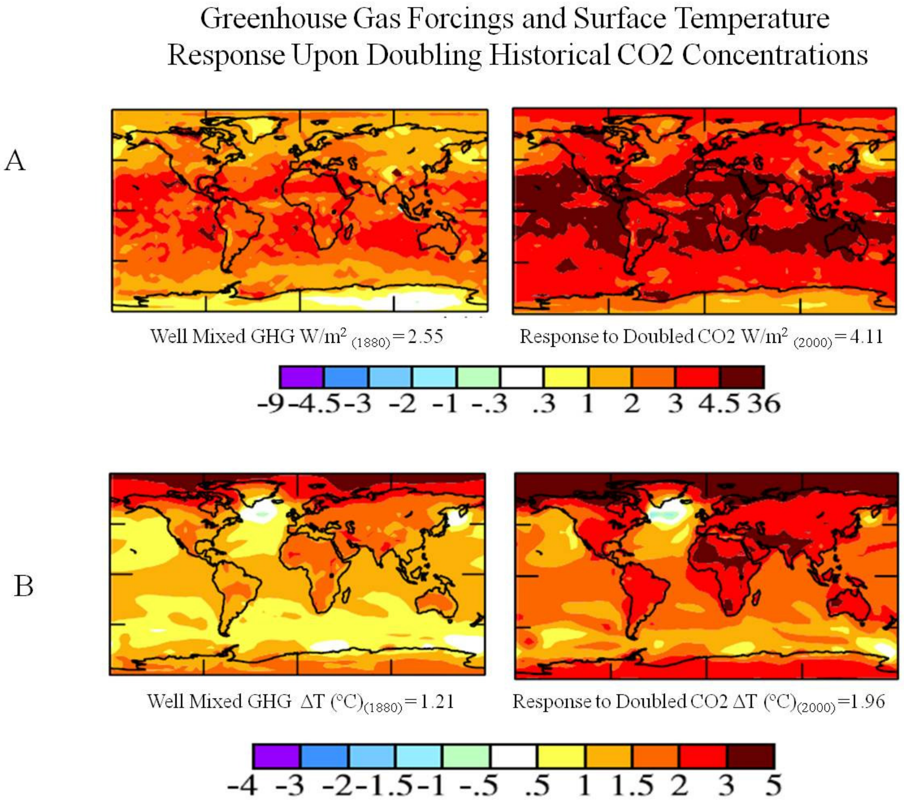

Figure 1.3: Modeled effects of doubling the atmospheric [CO_2] based on an initial concentration of 291 ppm in 1880 on the forcing (A) and on the predicted equilibrium global temperature (B) which is based on the predicted temperature change over the 120 year time span given the initial starting condition of the [CO_2]. Adapted from Hansen et al.[7]

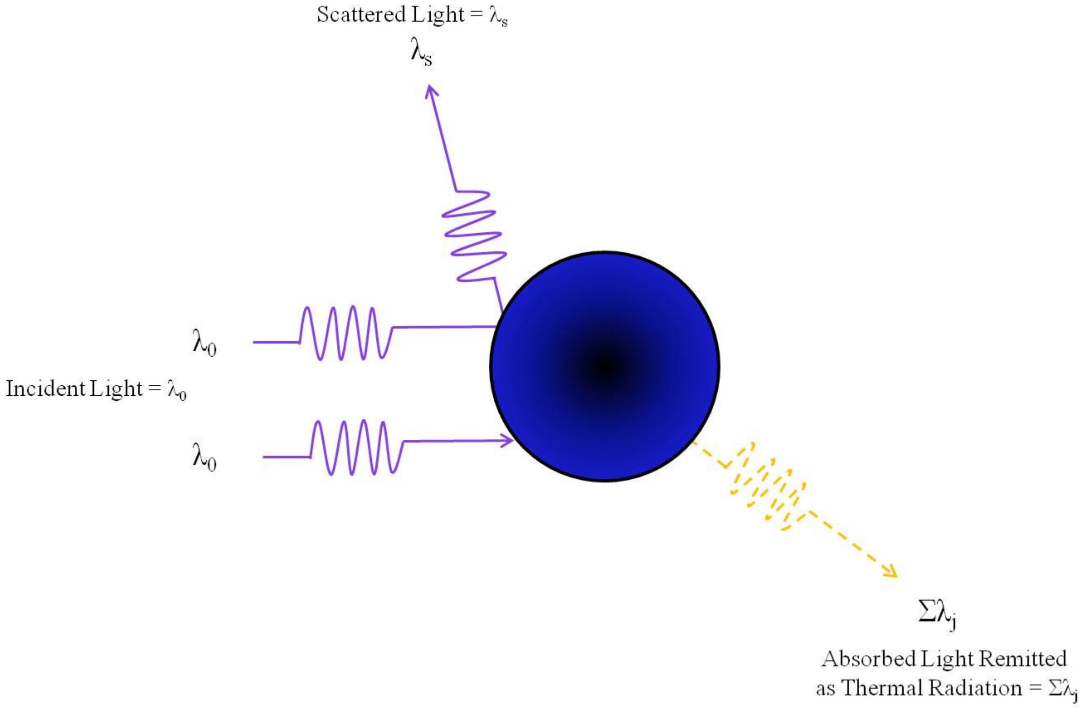

Figure 1.4: Mechanisms of light interaction with particles explored in this work. Based on work of Seinfeld and Pandis.[8]

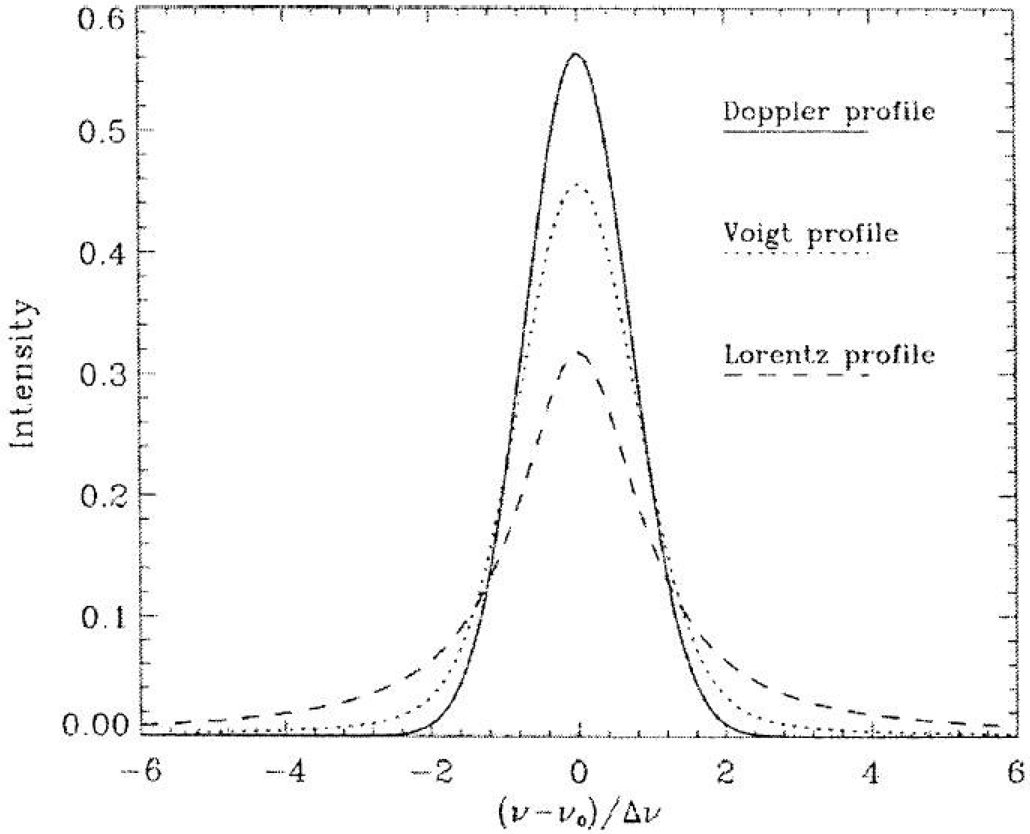

Figure 1.6: Line profiles for Doppler (solid line), Lorentz (large dashed line) and Voigt (dotted line) profiles. This is taken from Thomas and Stammes. [9]

Chapter 2: Experimental Motivation

2.1 Greenhouse Gases

Greenhouse gases (GHGs) have a direct impact on the climate and in the case of CO_2, has been linked to global temperature increases.[23] While many studies are underway, the magnitude of the problem is overwhelming and much more work is required. Inexpensive and sensitive instruments are needed that can be used to study greenhouse gases quickly and accurately.

The predominant GHG is CO_2, (outside of water) which has been vastly studied, but quantifying CO_2 and tracking changes in CO_2 accurately, inexpensively and quickly is still an issue that demands further attention. Ideally, a system that can examine different greenhouse contributors, such as GHGs as well as greenhouse aerosols would allow simpler and more available global site measurements. Many different GHGs as well as greenhouse aerosols have absorption characteristics, readily measured with several different techniques. In the case of this work, photoacoustic spectroscopy is employed on both gases and aerosols. The accuracy and precision of these measurements will be detailed in this dissertation.

2.2 Greenhouse Aerosols

Global climate models need refined forcing values for soot to properly estimate the change in the atmosphere due to anthropogenic emissions. Because of the variability in the values of the forcing of soot in the atmosphere, experimental measurements of the enhancement of the soot absorption cross-section (C_{abs}) are needed.[24] Values for the forcing impact of soot range anywhere from 0.27 Wm^{-2} to

0.54 Wm^{-2}.[25] With an average forcing of 0.41 ± 0.2 Wm^{-2}, there lies a huge uncertainty in its actual impact. One of the difficulties in obtaining quantitative optical properties of soot is the variability in morphology, composition, and conditioning of the soot. Since soot cannot be defined by a unique chemical formula (like e.g. silica) it is necessarily ill defined as a material, and varies from source to source.[26] Understanding the optical properties of soot becomes a daunting task when done in situ because of the myriad of variables in the atmosphere such as meteorology, sampling platform, history, age of air parcel and source.[27] Any quantitative assessment of the optical properties of soot and the impact of coatings requires a measure of laboratory control that enables one to eliminate or corral the number of variables inherent. Another factor that hinders many optical soot measurements is the traditional use of filter-based measurements such as particle soot absorption photometers and aethalometers.[28-30] While filter based measurements are robust, and involve a simple applications of Beer's law, there are many drawbacks to those methods. These include (1) an artificially high absorption reading if light is scattered off the particles on the filter and (2) light rescattering off suspended particles within the filter may result in multiple absorption events, again resulting in an artificially high absorption result.[31] Ideally one would like to make the optical characterization in a dilute aerosol state so that optical depth interferences and particle size effects be accounted for. Several groups have measured the absorption properties of soot.[32-36] A typical approach is an indirect determination through a difference in scattering and extinction. This indirect approach may provide reasonable values for the absorption properties, but a direct method can yield accurate results with a lower uncertainty than an indirect method.

Soot emissions are highly controlled in the United States and Europe, but in the developing world, primarily India and East Asia, understanding soot's impact is of utmost priority, as Fig. 2.1 demonstrates this is the major source.[10, 37] Due to meteorological transport, the emissions of soot and other aerosols are not confined to local boundaries and make them a large-scale problem. India's soot emissions, for example, not only impact India, but areas downwind as well.[37, 38] In general, air pollution does not follow borders; therefore, it is imperative that more work be done to understand soot's global impact. With these issues in mind, the motivation for studying the soot-aerosol system is clear.

2.3 Figures

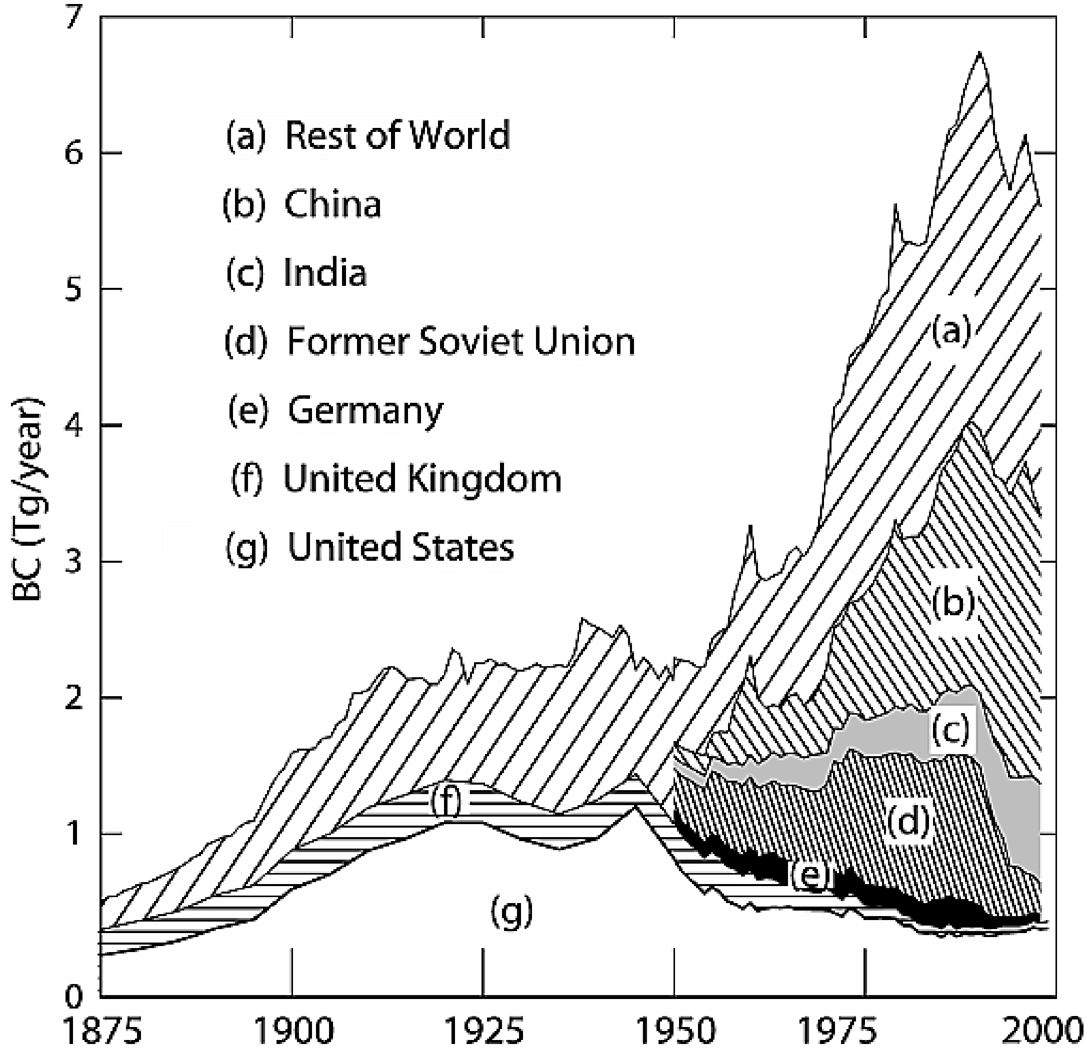

Figure 2.1: Estimated emissions of black carbon (soot) over the previous 125 years from Novakov et al.[10]

Chapter 3: Experimental Methods

Chapter 3 in this dissertation is intended to provide the reader with an understanding of all the major equipment and techniques used in this research. Each major piece of instrumentation is detailed in order to give both theoretical and practical information. In some cases where an instrument was minimally employed only a brief description was given. In all cases, the purpose and intent of the instrument is clearly stated.

3.1 Particle Generation

The experimental methods used in this work have several fundamental and key aspects that will be detailed in this section. In all the work presented, nanoparticles ranging from 20 to 1000 nm where generated (in the case of the soot) or prepared and aerosolized (in the case of the sucrose, PSL spheres and gold). Several methods were used in order to generate and prepare the nanoparticles but in all cases, the nanoparticles were transported in essentially the same manner. In this chapter, the details of the generation and preparation process, the transport process and the analysis process will be described in detail.

3.1.1 Diffusion Flame

Laminar diffusion flames have been studied for many years. The practicality of the diffusion flame lies in its simplicity as well as its controllability. The diffusion flame employed in this work comprised a central pathway for the fuel (ethylene in the case of this work) and an outer pathway for the oxidizer (particle free air). This coannular design allows for a steady and controlled laminar flame as shown in Fig. 3.1 and 3.2. The configuration enables the operation of a stable flame, and thus a consistent soot source over many hours of continuous operation. In the case of this work, the diffusion flame used is based on what is now known as a “Santoro Style” diffusion flame, named after Professor Robert J. Santoro of the Pennsylvania State University. Santoro’s work in the early 1980’s led to the development and establishment of this burner style for simple and safe soot production.[39]

Several factors have been identified in the formation of and growth of the soot produced by diffusion flames. Initially, a kinetically controlled chemical reaction within the flame leads to the formation of precursors for the soot particles. Secondly, a primary particle inception stage where the building blocks of the soot are initially formed, usually of similar size and shape. Thirdly, there is a period of time where particles grow via surface growth or coagulation and carbonization takes place while the hydrogen content is greatly reduced. Finally, a limiting step where the ultimate size of the soot particle leaving the flame is determined via agglomeration or even halted by oxidative attack. [39]

In the burner set-up, a glass sheath is used to surround the flame in order to maintain laminar flow. This sheath is split in two and the smaller portion is positioned under the sampling probe where the soot is captured and moved. The taller portion rests atop this sampling probe and lower sheath portion and is used to direct the wash of oxidizer up and away from the flame. The actual burner consists of a brass housing approximately 10 cm in diameter where a ceramic mesh screen is placed. The one cm diameter brass tube used to direct the fuel through the center of the burner is suspended within this ceramic mesh screen. The ceramic mesh screen is used in order to promote laminar flow for the oxidizer around the flame. Typical flow rates for both the fuel and oxidizer differ by several orders of magnitude. In this experiment, the fuel was typically run at 50 to 150 sccm while the air surrounding the flame was run at 30-50 lpm. Changing the fuel flow rate controls the flame height. The resulting flame was anywhere from one to 4 cm in height. This burner system was successfully used for several years in order to generate a steady stream of soot particles ranging in size from ≈ 30 nm to one micrometer.

3.1.2 Atomization

Nanoparticles can be put into the aerosol phase by several approaches. As described above, soot can be generated and captured into a stream of gas in order to transport it. The laminar diffusion flame burner generates and aerosolizes the soot all in one. However, when one wants to aerosolize existing particles, e.g., polystyrene latex spheres (PSL), sucrose or colloidal gold (Ted Pella, Inc.) a different method is required. In the work presented herein, a TSI Model 3076 Constant Output Atomizer (COA) was utilized. The COA, which is detailed in Fig. 3.3 has one keen advantage over other atomizers that as the solution is aerosolized in order to generate the nanoparticles, the concentration of the solution does not increase, subsequently increasing the particle size (most applicable to the sucrose solution). The COA was developed by Professor Benjamin Y. H. Liu and one of his graduate students, K. W. Lee on the University of Minnesota. The original COA used a syringe pump in order to provide a constant feed rate for the solution being aerosolized. In the work presented here, a syringe pump was not used, but the COA was run in non-recirculation mode so that the non-aerosolized solution does not return to the original solution which would concentrate the solution, thus, increasing the particle size. Typically, a one to ten percent solution of sucrose in de-ionized water was used in order to generate sucrose particles.

The COA was also employed in order to aerosolize PSL spheres for several purposes. The PSL are originally in highly concentrated solution, but this solution requires dilution in order to aerosolize it. Typically, several drops (5 to 10) of the PSL solution are diluted in 100 ml of de-ionized water and then placed in the COA. The COA produces a steady stream of PSL which was used in order of calibrate the DMAs as well as to test several theories in the PASm. [40]

3.1.3 Electrospray

Electrospray (ES) aerosol generation has wide applications and uses in many fields, but within the constraints of this work, was used in order to aerosolize both PSL and gold colloids. The history of electrospray process has its roots in mass spectrometry and can be followed back to the work of Fenn[41] and Dole.[42] Essentially, a solution with the analyte of desire is passed through a capillary with a pressure gradient and a potential. The solution passes through an electric field that generates a mist of highly charged particles. Upon exiting the capillary at atmospheric pressure, the analyte is nearly desolvated, thus generating a charged population of macro-ions, or charged analyte particles, which in this work are labeled, aerosolized nanoparticles. Figure 3.4 details the basic arrangement of the electrospray system. Upon exiting the electrospray, the charged particles are directed towards the appropriate instruments for analysis and characterization. While the electrospray process has a very long history, it is only described briefly within this text to explain its purpose in the experiments where it was used.

3.2 Particle Transport

The particles generated must be efficiently collected and transported to the analytical instruments.

3.2.1 Soot Transport

Placed directly above the flame tip is a sampling probe. The sampling probe consists of a stainless steel tube approximately one cm in diameter. A one mm hole was drilled into the wall of the tube and the tube is held orthogonally to the flame. A carrier gas (particle free air in this case) is directed through the sampling probe in order to carry the soot particles in the desired direction. Particle free air is delivered at 5 lpm orthogonally to the flame. An ejector pump downstream of the sampling probe creates a low-pressure region in the direction of the soot flow. In turn, this low-pressure region ($\Delta p \approx 10$ cm H_20) creates a pressure difference at the flame tip, which draws the flame into a one mm hole in the sampling probe at the flame-probe interface. The soot is carried to a 5 l accumulation chamber where the fresh soot is allowed to agglomerate for approximately one minute in order to increase the diameter at the peak of the size distribution as well as stabilize the concentration. From that point the soot flows through an ejector pump to the classification system for a total flow rate of 30 lpm after the ejector pump. After the ejector pump, the particles are driven out of the tubing into the laboratory exhaust hood. Prior to exiting into the hood, a “T” junction was built in order to siphon off the soot particles into the analysis system. The analysis system comprised of either one or two DMAs, the PASm and a CPC or electrometer was run in under-pressure mode. Essentially, a pump at the end of the flow train (housed in the CPC or the electrometer) pulled the particles through the analysis tools. Figure 3.5 is a schematic of a typical single DMA experimental set-up.

3.2.2 PSL, Gold and Sucrose Transport

Constant output atomizers and ES both produce positive pressure flows, so the method required to transport the particles to their desired destination are slightly different from that of the soot. The soot was generated in a neutral pressure mode and then carried into an over-pressure mode; however, the PSL, the gold and the sucrose particles exit their respective aersolization systems at a higher pressure than ambient (initially an over-pressure mode). Because the DMA-CPC system was run in under-pressure mode (as described earlier), a positive pressure flow train cannot be sent directly to the analysis system or a pressure build-up could occur. In order to capture the particles of interest, the particles were directed out of their respective aerosolization system into a HEPA (High Efficiency Particulate Absorption) filter at ambient pressure. Prior to the HEPA filter, a “T” junction was made in order to create a port to which the flow train could be connected for the analysis system. The particle flow out of the aerosolization system, in this case, was at higher pressure than the particle flow to the analysis system. By connecting the under-pressure system to the “T” junction, the nanoparticles can be siphoned away from the main particle train and directed to the analysis system.

3.2.3 Experimental Considerations

Several considerations are required when assembling the infrastructure of an experimental system such as the one used in this study. For example, materials that are electrically conductive are necessary in order to not have the charged particles stick to the walls. Stainless steel was the material of choice for the tubing, but in areas where more flexibility was needed, then Tygon or conductive silicone tubing (TSI Model #3001789) was used. Also, proper ventilation is critical when generating nanoparticles. The soot used in these experiments was generated inside the exhaust hood and any instrument that exhausted particles was directed to exhaust into the hood.

3.3 Particle Classification and Metering

In order to characterize the size and number of particles used in all the experiments reported, several instruments were employed. To characterize the size of the nanoparticles, a differential mobility analyzer (DMA) was employed. To count the particles a condensation particle counter (CPC) was used and the electrometer was employed when the charges on the particles needed to be counted. The details of each of these three instruments will be expanded upon in this section. Information regarding uncertainties and operating conditions will be specifically found in the results section with regard to the specific set of results that those conditions refer to.

3.3.1 Differential Mobility Analysis

Differential mobility analysis is an application of electrical classification methods. DMAs have been in use for several decades and its roots can be traced back to Knutson and Whitby.[43] A DMA separates particles based on the particle's electrical mobility. A balance between the drag forces on the particle is balanced with the electrical field the particle encounters allowing specific sized particles to pass through the DMA.

A DMA is comprised of central rod surrounded by a hollow, concentric cylinder. A voltage (zero to 1×10^4 V) is applied to the central rod thus creating an electrical field between the central rod and the wall of the cylinder. There is an inlet for the aerosols and an exit slit at the bottom of the cylinder. There is also an inlet and an exit for the sheath flow. Figures 3.6 and 3.7 depict the basic design of the DMA columns used. The sheath flow is the flow of carrier gas along the long axis of the DMA. This sheath flow is laminar and typically an order of magnitude larger than the aerosol flow. There is a fundamental equation that governs the mobility of the particles (Z_p) passing through a DMA.[43] To arrive at the Z_p, a basic derivation is in order.

Newton's laws of motion govern the behavior of both macroparticles and nanoparticles. In the case of nanoparticles, the following derivation demonstrates the origins of the electrical mobility equation that governs the behavior of a nanoparticle in a DMA.

Newton's second law states that the sum of the forces on a particle is equal to the change in the velocity of the particle with respect to time and the mass of the particle;

$$m\frac{dV}{dt} = \sum F_p \tag{3.1}$$

where m is the mass of the particle, $\frac{dV}{dt}$ is the change in velocity with respect to time and F_p is the net force acting on the particle. In the DMA, the particle feels two forces, F_D (the drag force) and F_E (electrical field force);

$$m\frac{dV}{dt} = F_D + F_E \tag{3.2}$$

The drag force on the particle can be described more accurately by the Stokes's drag;

$$F_D = 3\pi\eta d_p V \tag{3.3}$$

where the drag force (F_D) is proportional to the viscosity of the fluid (η) and the velocity of the particle (V). The force opposing the F_D in the DMA is the F_E, the electrical field force:

$$F_E = neE \tag{3.4}$$

where n, the number and elementary units of charges on the particle, e, the charge of an electron ($1.6\text{X}10^{-19}$ C) and E is the electric field. In a DMA, when $\frac{dV}{dt}$ is zero, Eq. 3.1 becomes;

$$3\pi\eta dV = neE \tag{3.5}$$

Solving for V, which can now be rewritten as V_E, the electrical velocity, the equation becomes;

$$V_E = \frac{neE}{3\pi\eta d} \tag{3.6}$$

It is convenient to express this equation in terms of the electrical mobility, Z_p, where the particle's electrical velocity in an E field of unit strength becomes;

$$Z_p = \frac{ne}{3\pi\eta d} \tag{3.7}$$

This Z_p applies to particles much larger than the mean free path and with a Reynolds number much less than one. However, when the particle in question is less than one micrometer, the effect of the gas on the particle at the surface-fluid interface cannot be ignored. In order to account for this fluid effect on particles that approach the mean free path (λ_a), the Cunningham Slip Correction factor (C_C) must be included. The C_C is proportional to the λ_a inversely proportional to the d:

$$C_C = 1 + \frac{2.52\,\lambda_a}{d} \tag{3.8}$$

The slip correction factor is now applied to the electrical mobility and the result is the final form of the electrical mobility of a particle in a DMA.

$$Z_p = \frac{neC_c}{3\pi\eta d} \tag{3.9}$$

The mathematical basis for the operation of the DMA relies on the probability that a particle entering the DMA will follow a streamline created by the sheath flow and exit the DMA with a specific Z_p. This probability is described by the transfer function (Ω):

$$\Omega = \left(\frac{1}{q}\right) * max\left[0, min\left((q_a, q_s)\left[\frac{1}{2}(q_a + q_s) - \left|2\pi Z_p \cdot \Delta\Phi + \frac{1}{2}(q_m + q_c)\right|\right]\right)\right] \tag{3.10}$$

where four flow rates; polydispersed aerosol flow rate in (q_a), monodispersed aerosol flow rate out (q_s), sheath flow rate in (q_m) and the sheath flow rate out (q_c) are input with regard to the electrical mobility (Z_p) and the electrical flux function (Φ). This equation is executable for a specific set of operating conditions that are controlled by the aerosol flow rates and of the sheath flow rates, three out of the four must be experimentally controlled in order satisfy the following relationship:

$$q_a + q_c = q_s + q_m \tag{3.11}$$

This linear relationship establishes that the sum of the in-flows needs to equal the sum of the out-flows. The result of Eq. (3.10) can be seen in Fig. 3.8. Further derivations for the Ω can be found in Knutson and Whitby.[43]

Understanding the relationship between the four flows in a DMA and how they relate to the probability that a particle will emerge with a given electrical mobility is necessary for an accurate size and size distribution measurement. . The DMA can be used to select monomobility particles by using a static voltage or can be used to measure a particle distribution by scanning the voltage. All of this reduces to a particle "window". Since the typical operating conditions used were with the aerosol flows in and out, equal, and the sheath in and out a equal, the resolution is defined as the ratio of the aerosol flow to the sheath flow$\left(\frac{q_s}{q_c}\right)$.

A practical understanding of the conditions governing a DMA has now been detailed as well as a conceptual understanding of what happens inside a DMA. For further detail with regard to the derivations of the principles described, please see Knutson and Whitby. [44, 45]

3.3.2 Mobility Diameters, What Do They Really Mean?

In theory, a sphere travelling through a DMA will behave as described in the previous section. The drag force will oppose the electrical force. In the free molecular regime where the particle diameter is much smaller than the mean free path

(66.5 nm for air at STP), the drag force is proportional to the square of the particle diameter or to the projected area. As noted in Eq. 3.3, the F_D is proportional to the diameter of the particle (d_p);

$$F_D \propto d_p \tag{3.12}$$

When the Cunningham slip correction (C_C) is taken into account, Eq. 3.12 becomes;

$$F_D \propto \frac{d_p}{C_C} \tag{3.13}$$

In the limit of where the particles are much smaller than the mean free path (λ_a), as they are in the free molecular regime, the C_C is proportional to the mean free path and inversely proportional to the diameter of the particle as seen in Eq. 3.8, therefore, Eq. 3.13 becomes;

$$F_D \propto \frac{d_p}{\lambda_a / d_p} \rightarrow F_D \propto {d_p}^2 / \lambda_a \tag{3.14}$$

where the F_D is now proportional to the d_p^2, or the projected area.

For non-spherical particles, the mobility diameter is often used to characterize the particle diameter. This is the diameter of a sphere that has the same mobility as the non-spherical particle. The mobility is computed from the balance between the electrical force and the drag force. However, because the particle is non-spherical, the other properties of the agglomerate will not be the same as for a sphere.

For agglomerates with primary particles much smaller than the λ_a, the majority of the primary particles that comprise the agglomerate are exposed to the gas molecules; therefore, the drag force is proportional to the number of primary particles when the fractal dimension is less than 2. In such a case the projected area of the agglomerate is proportional to the number of primary particles.

3.3.3 Condensation Particle Counter

Once particles exit the DMA they must be counted, ideally with a detector that is independent of particle size. There are several instruments capable of counting charged particles and two of those methods will be described in this section. A condensation particle counter (CPC TSI MODEL 3025A) and an electrometer (TSI MODEL 3068A) were used in this research.

The CPC has a long history dating back to 1888 with experiments conducted by John Aitken.[46] A CPC grows particles that are too small to be optically detected by heterogeneously condensing super saturated butanol on the particles. Once the particles have grown to several micrometers, they can be counted by single particle light scattering A schematic of the TSI 3025A can be found in Fig. 3.9.

The CPC in the experiments reported herein was the “end of the line” for all the particles. As mentioned earlier, the DMA system was run under-pressure. This under-pressure is a result of placing the CPC directly in line with the aerosol exit of the DMA column. The CPC draws particles with a built in vacuum pump, therefore, since the CPC is placed directly in line with the DMA, the pull of the vacuum in the CPC pulls through the DMA. Specifically, the CPC pulls the aerosol flow because the sheath flows (in and out) are controlled separately. The three flows that require control as established in Eq. 3.11 have now been identified. The aerosol out flow is controlled by the CPC, the sheath in flow is controlled by a flow meter and the sheath out flow is controlled by a vacuum pump. The fourth flow, the aerosol in flow, is automatically controlled in order to satisfy the linear relationship in Eq. 3.11.

3.3.4 Electrometer

A second method used for counting particles was an electrometer. An electrometer actually counts a stream of ions entering a Faraday cup. A Faraday cup is simply a cup designed to catch ions.[47] The ions are actually charged particles in the case of this work. Essentially, the total current (I) impinging on a filter within the Faraday cup is measured and can be converted into the number of charged particles (N) entering the electrometer with the following relationship;

$$I = Nn_p eq_e \tag{3.15}$$

where the elementary charge on an electron (e), the number of charges per particle (n_p) and the volumetric flow rate (q_e) are defined. The I is measured and the n_p is assumed to be equal to one. Therefore, N is the remaining variable that can easily be calculated. Figure 3.10 details the principal components of the TSI Model 3068 electrometer.

One drawback to the electrometer is encountered when multiply charged particles enter the flow stream. If the elementary charge on the particles is unknown, then the number of particles is also unknown. The electrometer has specific capabilities that were exploited in order to calibrate the DMAs used in these experiments by running known singly charged particles, as well as to determine the number of singly and doubly charged particles in some cases. A second drawback to the electrometer is a 1000 times less sensitivity, requiring much higher particle concentrations for accurate particle counting. The details of how the electrometer was used are found in Chapter 5.

3.4 Particle Analysis

Because most of the work was motivated from a global climate change perspective and the desire to understand how certain components of the atmosphere and associated particles interact with light, a method for determining the way the particles and gases interact with light in the atmosphere was needed. The initial impetus for the work outlined is the use of a photoacoustic spectrometer (PASm) to directly measure the absorption characteristics of the materials in question.

3.4.1 Photoacoustic Spectroscopy: History and Theory

Photoacoustic spectroscopy has a long history[48] and is a well-established analytical tool. [3, 11, 49, 50] Photoacoustic spectroscopy involves photon absorption by a gas or particle and subsequent energy transfer to thermal energy. The absorbed energy induces excitation in the vibrational, rotational and/or electronic states of the molecules which it interacts with. After excitation, these states relax back to the ground state via radiative and non-radiative pathways. Photos given off in radiative processes are not detected by photoacoustics. The non-radiative pathways, however, are facilitated by molecular collisions, which release energy from the excited state to the ground state via vibrational, rotational and electronic degrees of freedom to the translational degrees of freedom in the ground state, thereby increasing the system temperature. This temperature increase is transferred from the absorber to a surrounding medium (in this case air). The increase in the local gas temperature causes the gas to expand and the resultant density change is detected as a pressure (i.e. sound) wave, which is detected by a microphone. The power of the method resides in the fact that the amplitude of the sound wave is directly proportional to the amount of energy absorbed by the analyte, thus it depends on the absorption cross-section and incident intensity. As a result the method has been used as a very sensitive tool to measure the absorption cross-section (C_{abs}) of both gases and particles. For example photoacoustic spectroscopy has found applications for field measurement in atmospheric science. [4, 29, 35, 51] The well-tuned photoacoustic spectrometer (PASm) used in these experiments has a detection limit on the order of 3×10^{-9} cm^{-1} for gases (specifically, O_2)[52] and 15×10^{-9} cm^{-1} for soot.[52] In terms of gas and particle minimum detectible concentrations, these values would be approximately 3 ppm for O_2 and 1000 particles/cm^3 for 100 nm soot particles used in these experiments. However, the minimum detectible concentration is analyte specific while the absorption coefficient is proportional to analyte absorption cross-section and concentration. Using the absorption coefficient as the detection limit demonstrates the minimum energy loss in the cell that is detectible by the detector.

3.4.2 Photoacoustic Spectrometer Details

The PAS system used in all of the work reported herein was custom built at the National Institute of Standards and Technology (NIST) Gaithersburg, MD campus. The system was built by fellow collaborators; Gillis, Hodges and Havey. The system hardware comprised of an acoustic cell which is a 100 mm x 6 mm cylindrical duct (length x diameter) positioned between two 50 mm (l) x 30 mm (d) cylindrical chambers, machined from brass, an electret microphone (Knowles, MD6052USZ-1) with a sensitivity of 11.75 mV/Pa at 1640 Hz and 11.3 mV/Pa at 1275 Hz, a 405 nm continuous-wave laser (Power Technologies 405 nm 250 mW) intensity modulated at a modulation frequency (f_{mod}) ≈ 1.6 kHz with a function generator (Stanford Research Systems DS345) to match a resonance frequency in the acoustic cell and a calibrated power meter (Newport 918D-SL-OD3) to measure the transmitted beam power.[11] Figures 3.11- 3.13 show the resonator cell details and system configuration.

One of the most important advantages of the PASm over other absorption measuring techniques is that the measurement is conducted *in situ,* and because of the high sensitivity of the system, relatively low concentrations (on the order of 10^4 per cm^3) of particles are required limiting the chance that any aerosol-aerosol interactions can take place. The volumetric flow rate into the resonator is approximately $4x10^{-6}$ m^3/s; the particles pass along the analysis chamber with a sample volume of 3 cm^3, a residence time of approximately 0.7 s and then exit. As the particles pass through the analysis chamber they absorb energy from the laser. In the aerosol experiments, the laser current is directly modulated to match the resonator frequency while in the gas experiments the laser is externally modulated with an acousto-optic modulator. This photon energy is then converted to thermal energy through collisional energy transfer mechanisms and the resulting pressure wave created by the increased gas temperature is detected by the microphone. The microphone signal is then sent to a lock-in amplifier where both the in-phase, x, and out-of-phase, y, components are recorded. Output signals from the lock-in amplifier are regularly sampled by a data acquisition card (National Instruments PCI-6281, 16-bit, 500 Ksamples/s). An analyte free background signal is taken at the beginning and end of each experiment, which comprises all gases in the analyte flow as well as flow noise. The governing equation for this PAS system is as follows:

$$\alpha = \frac{R}{W_L K_N} \tag{3.16}$$

Here, α is the absorption coefficient in cm^{-1} measured in the cell, R is the measured PAS signal of analyte less background (i.e. gas of interest or soot particles less the measured noise due to flow and carrier gas in the case of the particles) in volts, W_L is the beam power of the 405 nm laser at the center of the PAS cell in watts and K_N is the photo-acoustic system constant previously determined in units of $\frac{V \cdot cm}{W}$. The photo-acoustic system constant is defined as follows:

$$K_N = \frac{C_N \beta_N \mathcal{R}_N}{\sqrt{8}} \tag{3.17}$$

where the cell constant is C_N and is geometry dependent, the microphone sensitivity β_N, and the relaxation response function, $\mathcal{R}_N$ (which lies between 0 and 1).

The relaxation response function demands further explanation for clarity. Non-radiative relaxation occurs through several channels where each channel is a multi-step cascade of events. In most cases, the time for the excited states to relax to the translational degrees of freedom is very short in comparison to the acoustic cycle. In some cases, however, a bottleneck in the cascading events increases the relaxation time. If the relaxation time is longer than the acoustic period, the efficiency of the acoustic wave generation is reduced. This relaxation respo0nse function is typically assumed to be unity for systems where there is a rapid relaxation process (as in the aerosols).

The time scales of the absorption and relaxation processes are also of interest. While the time scale of the absorption of a photon by the particle and the subsequent relaxation of the excited particle are not known exactly, but the absorption can be approximated by solving for the Einstein A coefficient in a stimulated emission calculation. While the exact time for an absorption event to take place cannot be calculated, the ratio of the time scale for absorption to the acoustic time scale can be approximated by employing the measured absorption cross-section (σ_{21}), the wavelength of the laser (λ), the index of refraction (n) (assumed to be 1 for this approximation) and an approximation for the spectral line shape function ($g(v)$) (which is the inverse of the laser bandwidth).

$$\sigma_{21}(v) = A_{21}\frac{\lambda^2}{8\pi n^2}g(v) \tag{3.18}$$

The acoustic cycle time scale is the inverse of the resonant frequency, which in the case of the soot study is on the order of $6\text{x}10^{-4}$ s. Based on the approximated absorption time scale and the acoustic cycle, the absorption of a photon is approximately 9 orders of magnitude faster than the acoustic cycle.

Subsequently, it is known that for particles in the 10's to few hundred nanometer range, the temperature increase in the particle is on the order of a few Kelvin and rises linearly with laser power. However, a noticeable temperature increase due to particle heating by the laser would require multi-Watt power levels as noted in Murphy (2009)[53] and in these experiments, sub-Watt laser powers were employed. This heating is essentially instantaneous and the particle temperature is uniform. The transfer of the heat in the particle to the surrounding gas is also essentially instantaneous. During an acoustic cycle, the length of the gas thermal penetration scale is orders of magnitude larger than the particle diameter (approximately 65 μm for the gas thermal penetration length compared to approximately 20 nm for a soot primary particle).

The photo-acoustic system constant is calibrated based on measurements of a gaseous species having known concentration and absorption coefficient. Agreement has recently been demonstrated for K_N between experimental measurements and modeled acoustic response ≈ 1 % for measurements of the O_2 *A*-band in air. [11] It was also shown that the relaxation response function $\mathcal{R}_N \approx 0.40$ must be incorporated into an accurate calibration involving the O_2 *A*-band. Other studies which aim to exploit the convenience of calibrating with the *A*-band at ambient conditions implicitly assumed a relaxation response function of 1 and were, therefore, subject to large, systematic errors (Tian *et al.*[54]). For the work presented within, it is assumed that the relaxation response function for any studied particles in air is unity and measurements of α rely on the product $C_N\beta_N = 18.7\frac{V\cdot cm}{W}$ [11] to model the instrumental response. Thus, measurements of the absorption coefficient for aerosols, α (cm^{-1}), flowing through the acoustic cell can be determined from the magnitude of the microphone signal (V) and the laser power (W). For a more detailed account of the calibration of the PASm, refer to Gillis *et al.* [11]

With respect to the soot measurements, the number of particles in the beam at any one time is approximately 3 % of the concentration of the particles in the cell at any time (approximately 1000 particles based on typical particle concentrations in the cell), which is the ratio of the beam volume to the sample cell volume. The typically low concentrations (10^3 to 10^4 particles/cm^3) of particles in the cell minimize the extinction of the laser through the path length, which in turn leaves the beam intensity nearly uniform along the path length, therefore, all the particles in the beam are exposed to the same intensity, making their orientation unimportant with respect to their ability to absorb energy and produce the PAS signal. Furthermore, the optical depth of the laser in the cell is related to the absorption coefficient measured by the cell which, in the case of the cell used in these experiments, the minimum detectible absorption coefficient is approximately 15 x10^{-9} cm^{-1}. The cross-section measured is related to the probability that a photon is absorbed by a particle. On average, there may be up to 10^8 photons absorbed per particle in the cell. This number of absorption events assures a high probability that absorption events occur and is proportional to the number of particles in the path length of the cell. The more particles in the path of the laser, the higher the probability an absorption event will occur. This is essentially Beer-Lambert's law, which is why the absorption coefficient is reported in cm^{-1}, because as Beer-Lambert states, the absorption coefficient is the measure of the light loss along a specific path length, thus the units are in inverse length units.. More on why the whole soot agglomerate contributes to the absorption signal is detailed in Chapter 5, but essentially, a particle with a fractal dimension of less than 2 (which these are) are basically transparent, or rather, all the primary particles are equally visible and no shielding takes place, regardless of orientation.

While scattering off the particles is present, it does not affect the PAS signal because the microphone does not pick up scattered light, only reradiated thermal energy. The placement of the microphone at the center of the cell is critical to efficient signal collection as the maximum acoustic pressure is in the center of the sample cell with a node at either end of the cell. Because the acoustic wave is a standing wave, the sum of the signal, which is representative of the particles in the cell is collected at the optimal location in the cell making particle location with respect to the microphone irrelevant, the particles merely need to be in the beam.

3.4.3 Photoacoustic Spectrometer Data Collection

Collecting an absorption signal with the PASm system involves many steps, but the most critical steps will be outlined here. The diode laser current is directly modulated with a function generator in order for the intensity modulation to match the frequency response of the acoustic resonator while not affecting the frequency of the single wavelength laser. The frequency, $f_{0,}$ is directly proportional to the speed of sound, C_{ideal}, in the resonator and in the limit of the ideal gas law can be described in the following manner:

$$C_{ideal} = \lim_{P\to 0} C_{T,P=} \sqrt{\frac{\gamma RT}{M}} \qquad (3.19)$$

The adiabatic index, γ, pressure P, T is temperature, R is the ideal gas constant and M is the molar mass. In this system, the lowest-order mode which efficiently couples to a modulated laser current has a resonant frequency in ambient air at 296 K of approximately 1640 Hz. [11] This frequency is dependent upon the composition of the gas and analyte in the acoustic resonator. Note how C_{ideal} depends on the square root of the inverse mass, when the mass changes, so does the C_{ideal}. Because of this dependence, for each analyte studied (the gas was always particle free air in each study), the peak resonant frequency was measured and then adjusted for that experiment. In order to measure this peak frequency, a large concentration of analyte was introduced into the resonator under normal operating procedures. The frequency of the laser modulation was then swept from approximately 1.5 to 1.7 kHz in 10 Hz increments, ensuring that the approximate frequency mentioned earlier would be captured. The PASm signal was recorded for each corresponding frequency and where the signal was strongest, that frequency was adopted. This was a simple solution for fine tuning the modulation frequency of the laser because in all cases with aerosols, the gas medium was the same and only slight adjustments were required. In the calibration of the PASm system discussed in Gillis *et al.*[11], it was not so easy because the gas itself was the calibration standard and the frequency was quite different for the O_2 and CO_2 calibration. The frequency was swept from 1 kHz to 6 kHz to find the resonant frequency for those two mentioned gasses. One very important feature that differentiates this PAS system from others is that in the course of the calibrations procedure, it was determined that calibration was not actually necessary. The model that governs the PAS system matches the calibrated results to within 1% for the O2 and within 3% for the CO2 that further calibration is unnecessary. If a system component change was required, a revised constant would be computed using the modified parameters. Details of that calibration can be found in Gillis *et al.* [11]

Upon locating the peak frequency corresponding to the analyte in question, the 405 nm laser current was modulated with a function generator to match the resonant frequency in the resonator. This modulator was synchronized with a lock-in amplifier used in order to collect the appropriate signal from the microphone. The time scale of the measurement can be calculated from the laser modulation frequency of 1.6 kHz. The lock-in amplifier has a time constant, which in the case of the soot measurements was 300 ms, which is averaged over several acoustic cycles. The lock-in amplifier output is averaged over a range of 10 kHz - 100 kHz (10 to 100 μs), which oversamples the data. The 10 kHz - 100 kHz data is then averaged for 60 s ,which comprises one measurement. Multiple 60 s signals are taken for any one experiment, which is eventually averaged to produce the final PAS signal for that specific analyte. An example of the raw signal can be seen in Fig. (3.14). Figure 3.14 shows the raw PAS data (the red markers and fit line) as well as the PAS signal that has been fit to a complex function that describes the acoustic resonance in the cell (blue markers and fit line). The measurements are made at the peak of the blue line.

Data collection processes involve sampling both the in-phase (x) and out-of-phase (y) components of a two channel lock-in amplifier (Stanford Research Systems SR830) synchronized to f_0. Background signals, x_0 and y_0, are collected in the absence of the absorbing analyte but with all other background gasses present. In the case of the soot study, the DMAs in line with the PASm were turned off to stop the passage of the soot particles but the diffusion flame was kept on in order to generate any accompanying gasses that might absorb at 405 nm, such as NO_2. The amplitude of the PAS signal (R) for an absorbing species on resonance is obtained from;

$$R = \sqrt{[(x - x_0)^2 + (y - y_0)^2]} \tag{3.20}$$

where x_0 and y_0 are the measured background signals and x and y are the measured signal with analyte. They are summed in quadrature and the root of the square of the sum is R. This now returns us to Eq. 3.16 and R is substituted with Eq. 3.20. Ultimately providing an α, which when coupled with the particle counts from the CPC, an absorption cross-section per particle (C_{abs}) is determined, which in the case of all the work regarding the soot was the ultimate goal.

3.5 Figures

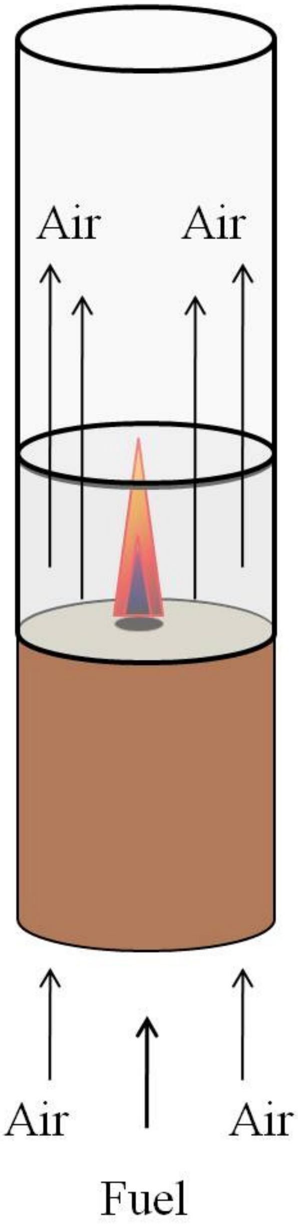

Figure 3.1 Schematic of a "Santoro Style" laminar diffusion flame burner used in all soot experiments.

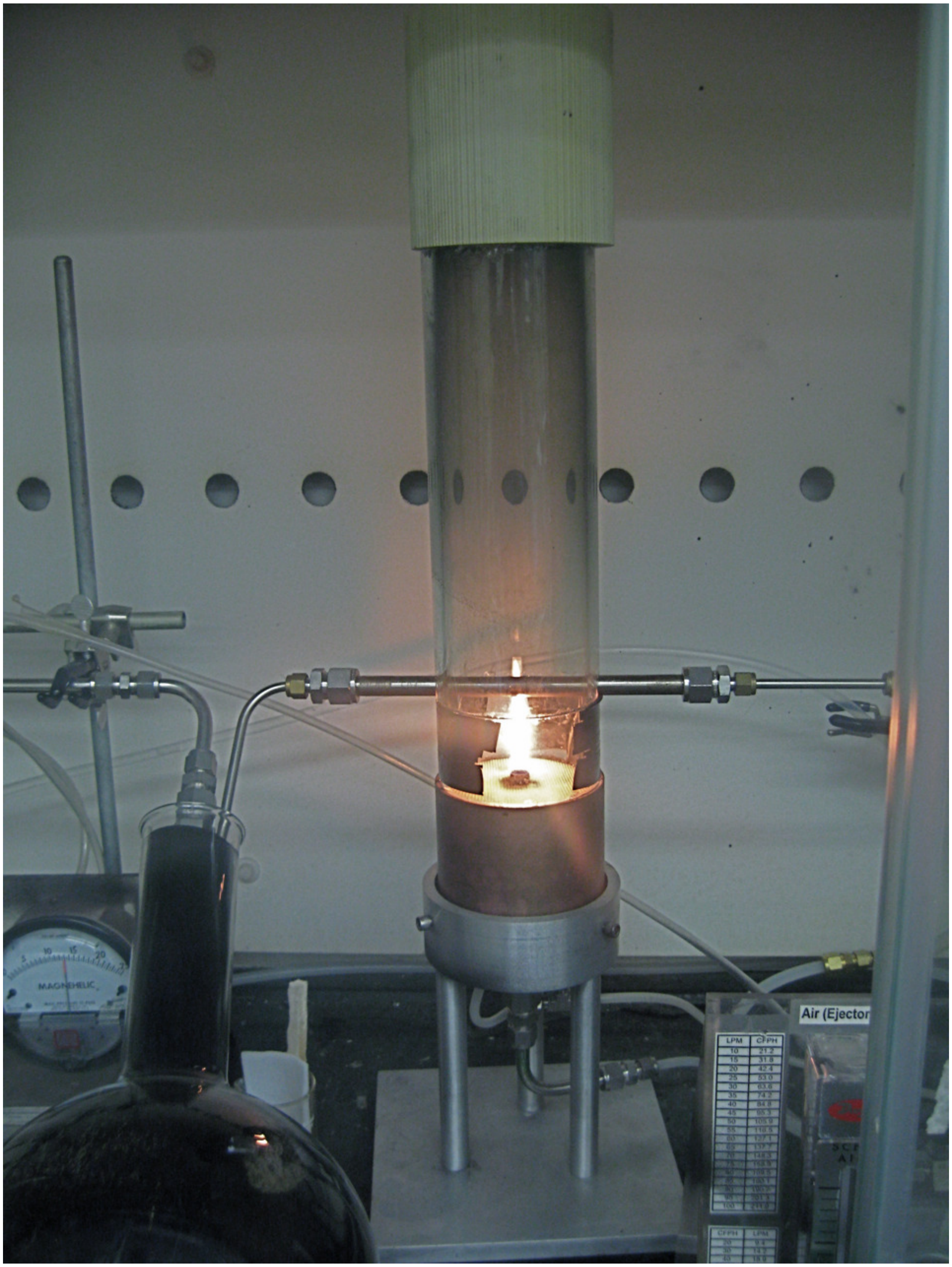

Figure 3.2: Photograph of laminar diffusion flame burner.

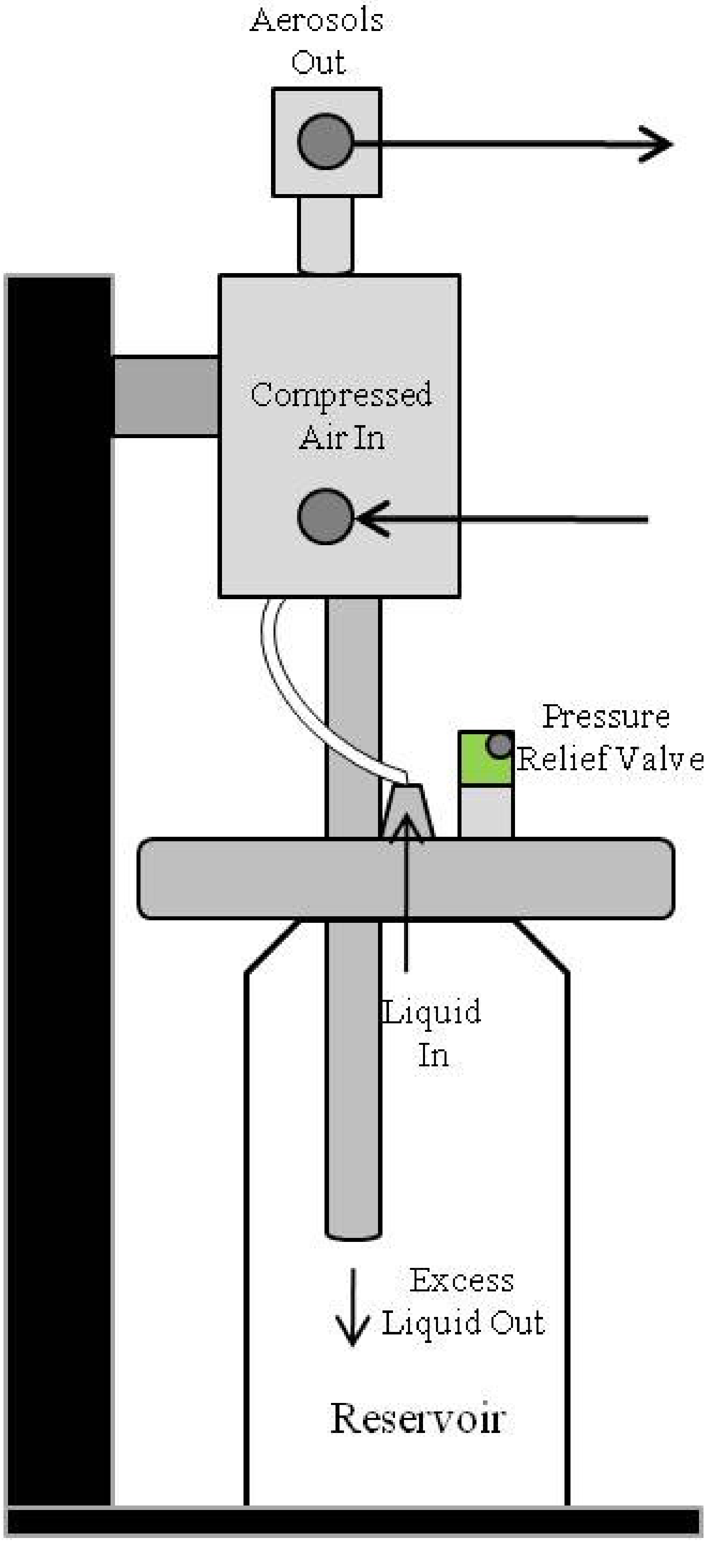

Figure 3.3: Schematic of a TSI Model 3076 constant output atomizer.

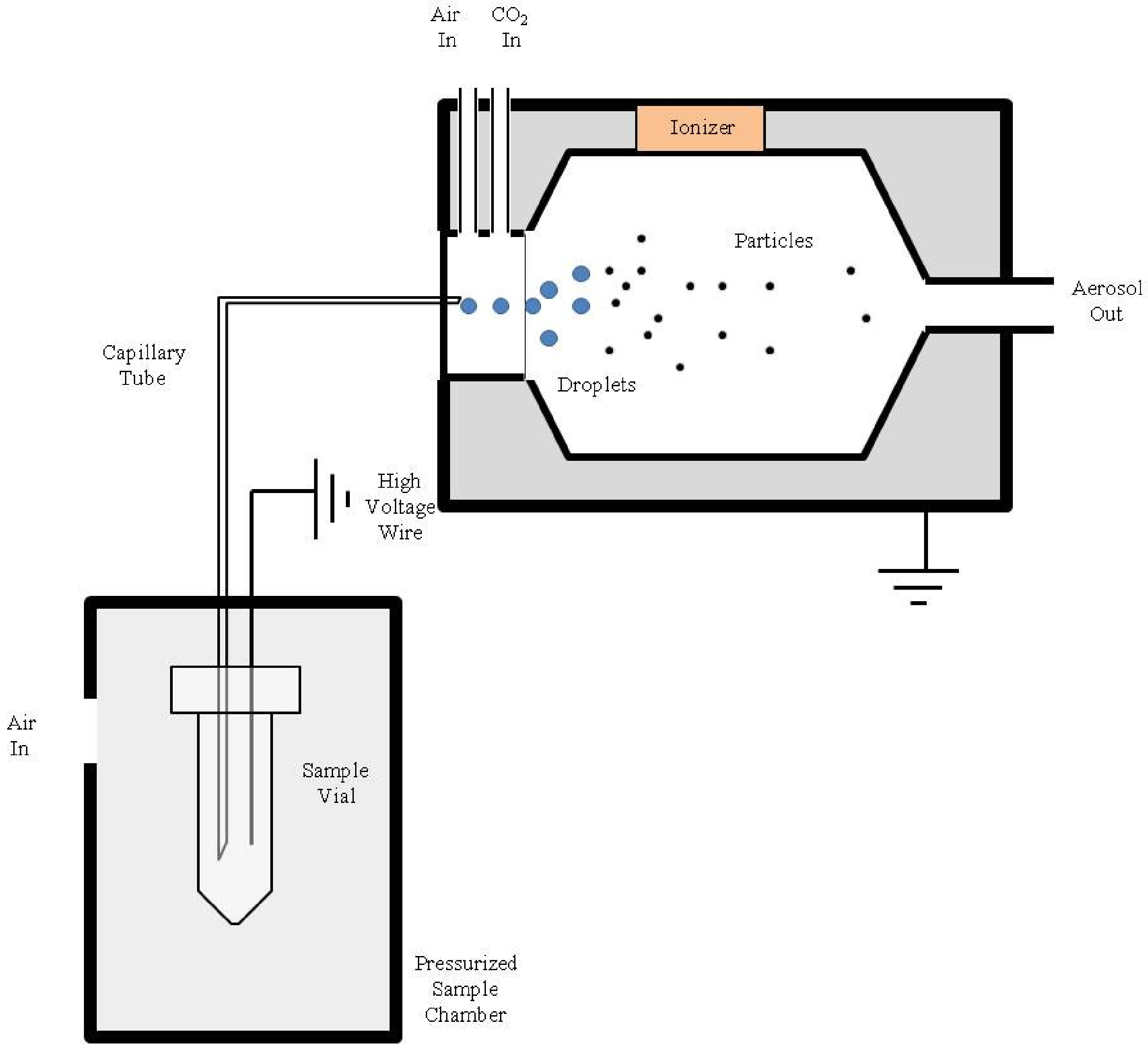

Figure 3.4: Schematic of a TSI Model 3480 electrospray.

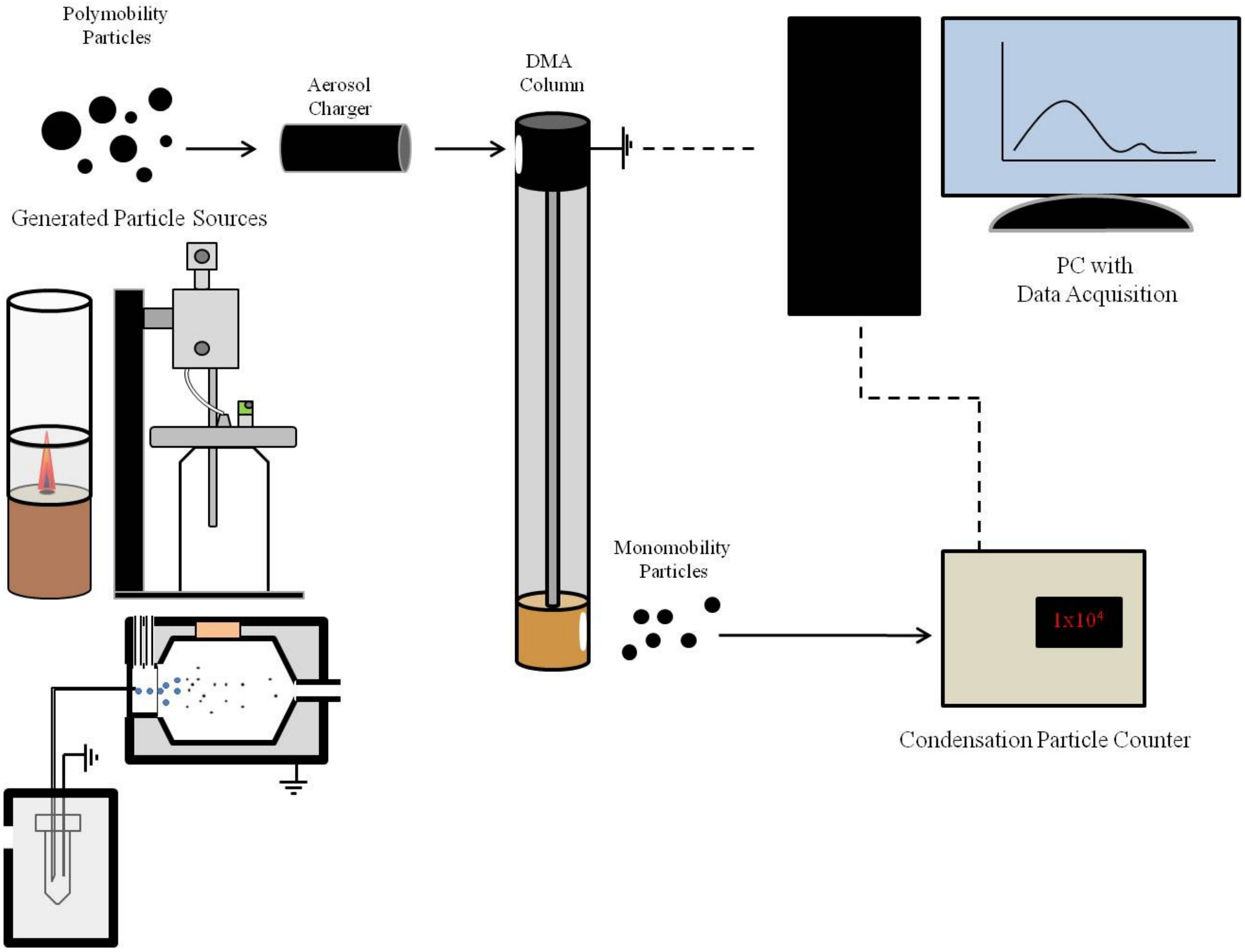

Figure 3.5: Basic experimental set-up including particle generation systems, single DMA column, an aerosol charger, condensation particle counter and a data acquisition system.

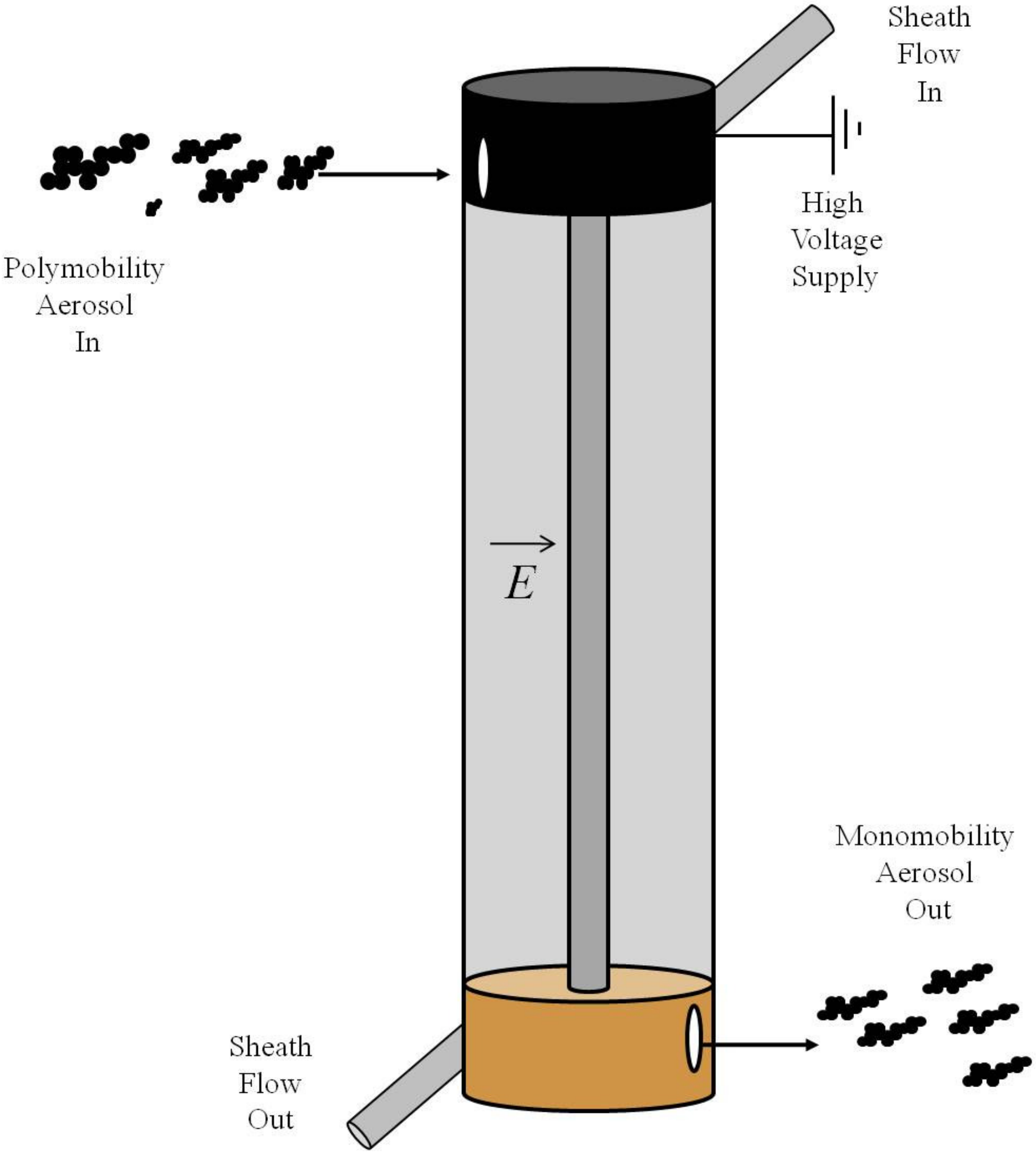

Figure 3.6: Schematic of a TSI Model 3081 DMA column.

Figure 3.7: Photograph of custom built differential mobility analyzer using a TSI Model 3081 long column.

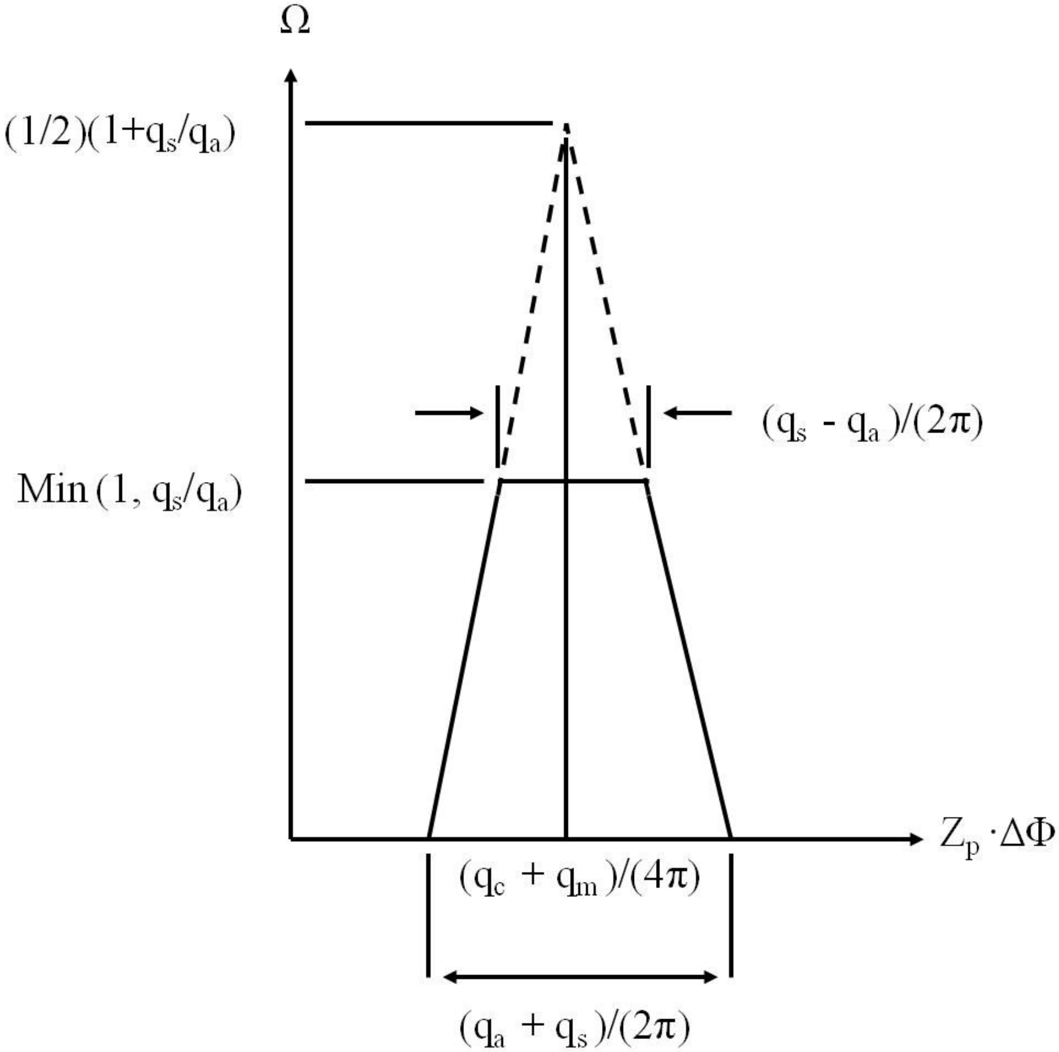

Figure 3.8: A graphical representation of the transfer function for a DMA. The probability that a particle has a specific Z_p is along the y-axis and the Z_p in question is along the x-axis.

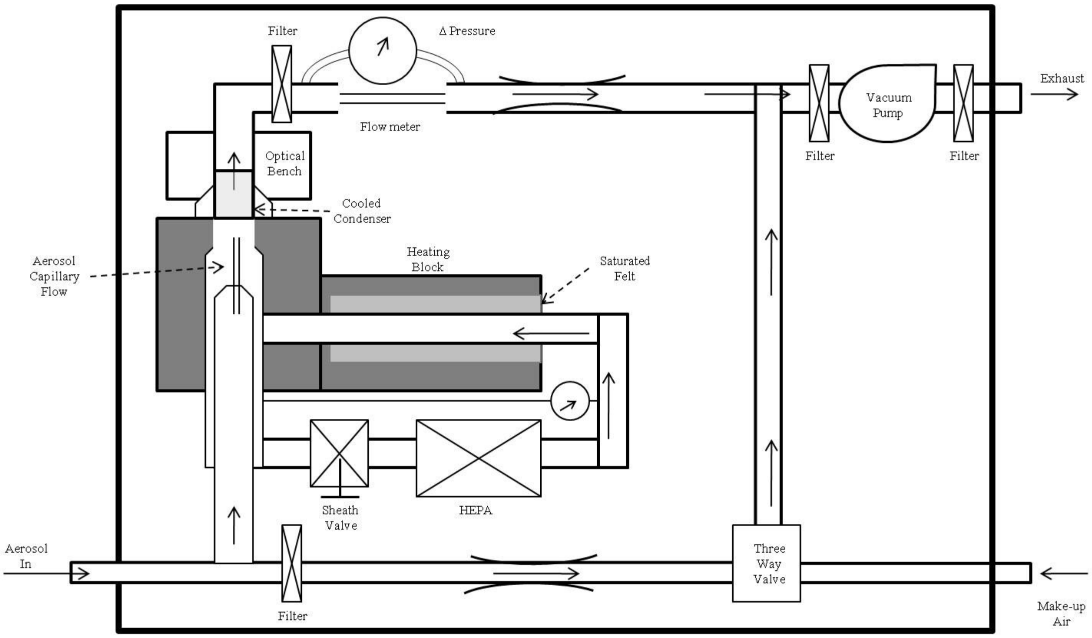

Figure 3.9: Schematic of TSI Model 3025A condensation particle counter.

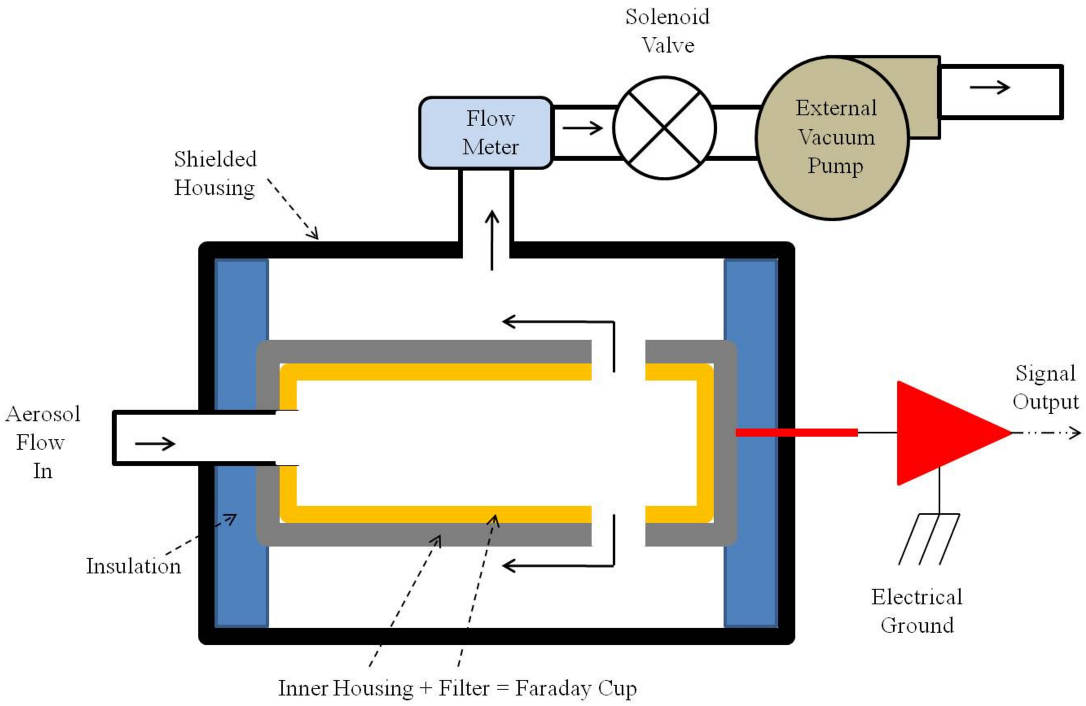

Figure 3.10: Schematic of a TSI Model 3068 electrometer.

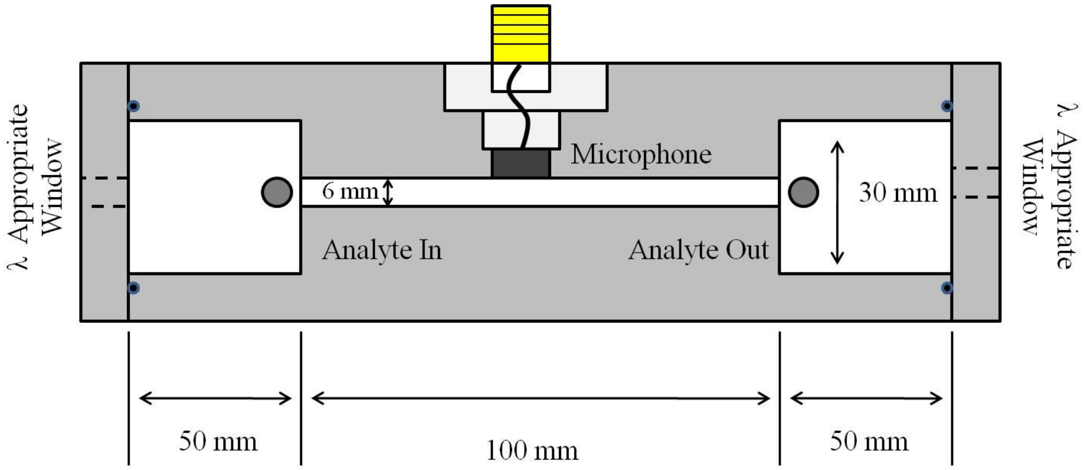

Figure 3.11: Schematic of photoacoustic resonator with dimensions included.

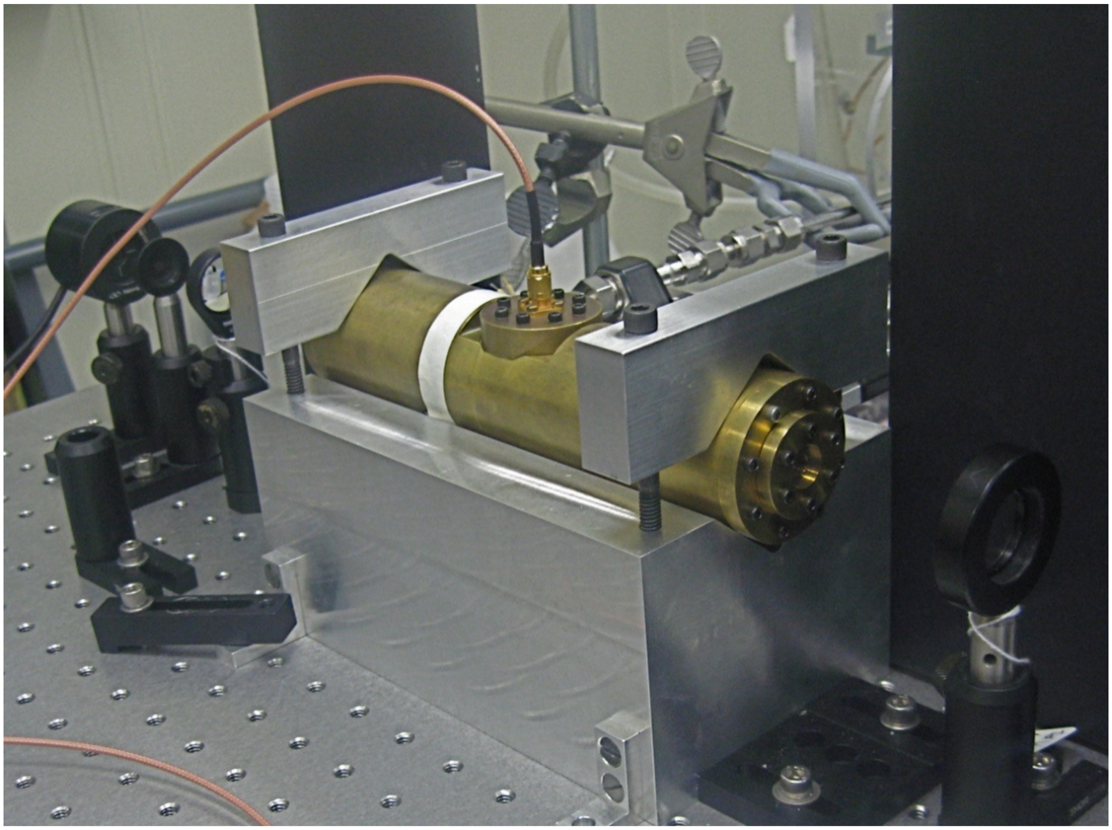

Figure 3.12: Photograph of the photoacoustic cell used in these experiments.

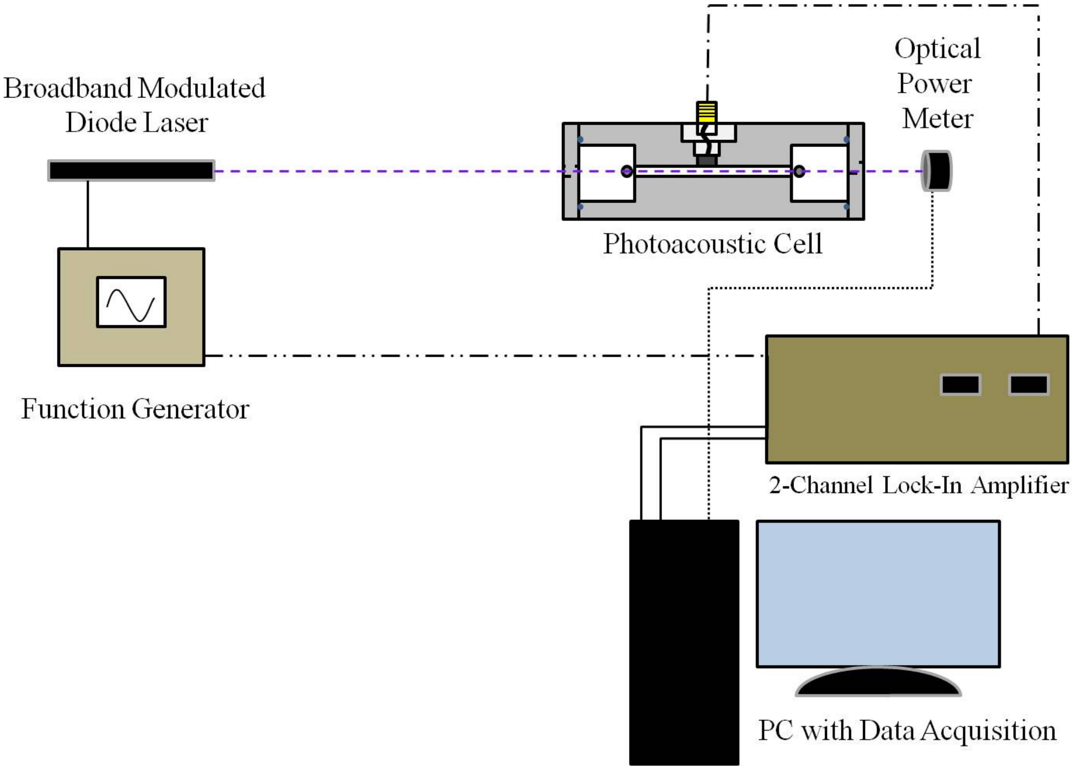

Figure 3.13: Photoacoustic spectrometer system with accompanying components.

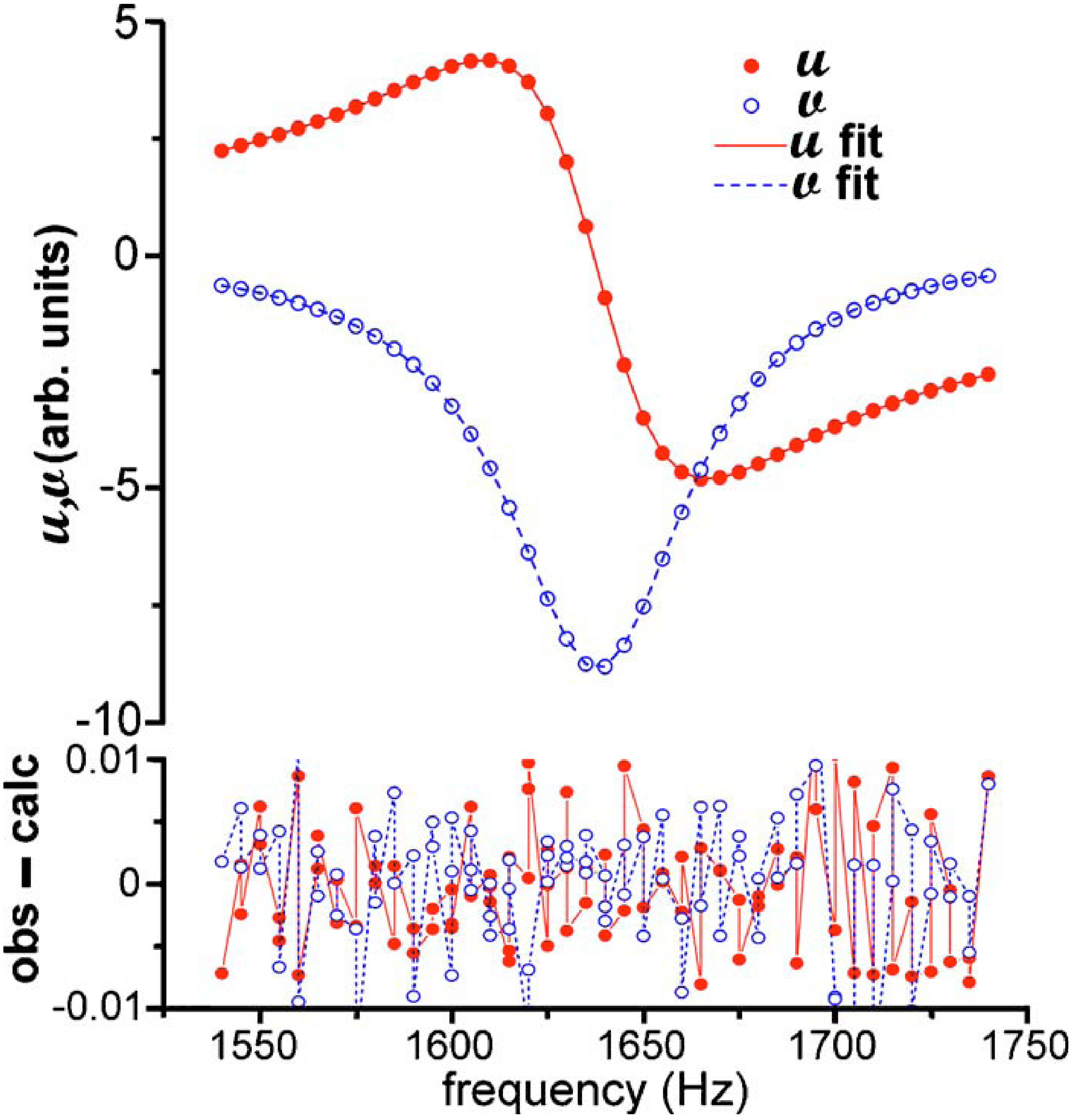

Figure 3.14: Measured acoustic resonance (red line and markers) and fit (blue lines and markers) to complex resonance function corresponding to laboratory air at *T* = 300 K, *p* = 98.5 kPa. Fitted values include *f*0 = 1638.22 Hz and *g* = 29.2 Hz. Upper panel: u and v measurements (symbols) and fits (lines). Bottom panel: fit residuals for u and v components.[11]

.

Chapter 4: Standard Photoacoustic Spectrometer: Measurements of Greenhouse Gases and Aerosols

4.1 Introduction

There exist numerous analytical techniques for studying absorption of atmospheric species. Detection of greenhouse gases in the field typically involves using spectroscopy, and examples include non-dispersive infrared (NDIR)[55] and tunable diode laser absorption spectroscopy (TDLAS).[56] The current state-of-the-art incorporates advanced spectroscopic methods such as continuous-wave cavity ring-down spectroscopy (CW-CRDS)[57] or other cavity-enhanced methods[58] which can perform with relative combined standard uncertainties of < 1%. However, a major obstacle for utilizing state-of-the-art greenhouse gas detectors is resource investment. Commercial CW-CRDS instruments can approach $60,000 for a single sensor, which prohibits deployment on a large scale. Thus, there is a need for new robust, yet simple and less expensive, high-performance analytical instruments to measure greenhouse gases in both laboratory and field environments.

Measuring the absorption of aerosols is complicated by the interplay between absorption and scattering. One measurement approach has been to quantify extinction (absorption + scattering) using cavity ring-down spectroscopy, and scattering via nephelometry, with absorption obtained from the difference. Unfortunately with this approach, the combined uncertainty in the deduced absorption can be substantial and the measurement can be subject to additional bias. Photoacoustic spectroscopy (PAS) is seeing increased use as an absorption probe for investigating problems related to atmospheric and climate chemistry to help mitigate these complexities. Numerous recent studies have established PAS as a standard aerosol absorption measurement technique to compete with typical filter-based methods.[28, 35, 59] Laboratory and field studies have been done using PAS[60] on aerosols which have investigated topics ranging from the effects of particle coatings,[61, 62] instrument cross-comparison,[63] and a relative humidity dependence on mineral dust.[30] These studies all exploit the attribute that PAS is sensitive only to absorption but not extinction or scattering.

However, while PAS does selectively measure absorption, it does so indirectly. Photon excitation deposits energy into a system. That energy then undergoes several processes: (1) conversion to internal degrees of freedom in the absorbing molecule, (2) transfer to thermal energy via molecular collisions with surrounding gases, (3) detection as a pressure wave by an acoustic sensor. Because of the complex processes involved, the response function is photoacoustic spectrometer specific and requires calibration and/or modeling. Relative uncertainty requirements for PAS calibrations specifically for atmospheric measurements typically range from 2% to 10% depending on the application. Most calibration techniques are focused on determining the detected amplitude of the pressure wave for a given sample absorption coefficient, solely considering (3) in the above description. Traditionally, PAS calibrations have been done utilizing gas phase absorbing species, NO_2 for example.[3, 64] In 2006, Lack *et al.*[60] outlined a calibration method using both ozone gas and nigrosin (India ink), a potential standard aerosol, to achieve a relative combined uncertainty at the 1-2% level for a gas sample and > 95% stated accuracy when validated for aerosols. To achieve these uncertainty levels Lack *et al.*[60] paired the PAS technique with additional instrumentation, specifically CRDS. While successful, the overall approach requires an increased level of technical expertise as well as substantial resource investment. Also, while the aforementioned calibration procedures are now well-established, their accuracies are ultimately limited by uncertainties in calibrant optical properties.[65]

Only recently, has molecular spectroscopy reference data for typical atmospheric molecules achieved the < 0.5% uncertainty levels required for improvement.[13, 66, 67] Realizing this, Tian *et al.*[54] recently presented a convenient and potentially high-accuracy calibration procedure based on measurements of absorption within the $b^1\Sigma_g^+ \leftarrow X^3\Sigma_g^-(0,0)$ band of O_2. These transitions commonly referred to as the O_2 *A*-band, arise from rotationally resolved magnetic dipole transitions near 765 nm. Unfortunately, a complication not considered by Tian *et al.*[54] is that for the O_2 *A*-band transition energy transfer processes involved in quenching the upper $b^1\Sigma_g^+$ state (see (2) and (3) above) can substantially reduce the efficiency with which the absorbed photon energy is converted to thermal energy on characteristic acoustic time scales.[11] Recently, using a photoacoustic spectrometer developed at the National Institute of Standards and Technology (NIST) we demonstrated that for the O_2 *A*-band, energy transfer processes can suppress the acoustic signal by as much as a factor of 2.5 because of the multi-step relaxation process. Moreover this effect depends strongly on quencher availability (e.g. relative humidity).[11] Other groups have explored and quantified the effects of energy transfer processes on PAS signals for small polyatomic molecules including HCN, CH_4, and CO_2 for many years.[68] However, by incorporating energy transfer processes into our resonator model we have reported a calibration procedure having a relative combined uncertainty of 1%

for selected transitions within the O_2 *A*-band.[11] This calibration was done conveniently on a sample of ambient laboratory air having a known relative humidity. Further, the calibration was consistent with and validated our resonator model. Specifically, the model independently predicted the measured response (which included an absolute calibration of the microphone sensitivity and optical power meter) within the combined measurement uncertainty. This means that the instrument response, containing the setup constant, can be discerned from first principles[11] and does not necessarily require traditional calibrations against reference samples with known optical properties. [11, 50, 69]

This work presents evidence that a custom–built PAS system based on a first principles model can be used in order to make quantitative measurements of both atmospheric gases and particles. The PAS system is used in order to measure CO_2 in ambient air and show that the PAS system can be used to detect subtle changes in a trace gas in amongst a very large background of other gases. It is also shown that PAS is well suited in quantitatively measuring atmospherically relevant aerosols that require in situ, fast response time and long-term stability measurements. Specific details regarding the PAS system construction and theory are found in Chapter 2 and are only briefly outlined in this chapter.

4.2 Experimental Apparatus

Instrument and data collection is outlined in Chapter 3, but specific details regarding the experiments in this chapter will be described herein and can be seen in Fig. 4.1. To collect data one must first intensity modulate the continuous-wave laser, using an acousto-optic modulator (AOM) for example, to match the frequency response of the acoustic resonator. This frequency, f_0, is complex to predict[11] but is directly proportional to the speed of sound in the system to be measured. This frequency can change dramatically depending on the gas composition in the acoustic resonator. For example, as shown in Fig. 4.2, in pure CO_2 at 296 K and 101.3 kPa the modulation frequency shifts to approximately 1275 Hz, easily predicted from Eq. 3.16. Shifts in $f_{0,}$ in turn, affect the amplitude of the photoacoustic signal. Approaches for dealing with this are fourfold:

(1) Maintain constant temperature such that amplitude fluctuations are a small contribution to the combined uncertainty of the measurement[50, 60]
(2) Measure the acoustic resonance prior to making any PAS measurement[11]
(3) Actively model the PAS resonator line shape and shift in resonance frequency based on inputs from precision temperature measurements to correct the signal amplitude in real time
(4) Adjust the modulation frequency during the course of a measurement to remain at the peak of the acoustic resonance either by using the modeled frequency shift or incorporating another type of servo

While approaches (1) and (2) are preferred there are cases where incorporating them to satisfy combined uncertainty requirements is challenging. We have currently made no attempt to regulate the temperature of the PAS instrument. Instead, by applying approaches (3) and (4) using Eq. 3.16 to calculate temperature-dependent shifts in f_0 we have observed improvements in measurement precision as high as 40% for temperature fluctuations on the order of $\Delta T \sim 1\text{-}2$ K.

After locating the acoustic resonance, the laser wavelength must be matched to a spectral region of optical absorption to probe an analyte of interest. For aerosol particles this is generally simple since absorption is, for the most part, spectrally broad. For measurements of greenhouse gases, the laser must be single-mode and tunable and its frequency should be scanned over a given optical transition. After locating this transition, measurements can then be collected by either measuring the spectral dependence of the PAS signal or by collecting data at fixed wavelength and modeling the local absorption coefficient. Our data collection process involves sampling both the in-phase (x) and out-of-phase (y) components of a two channel lock-in amplifier synchronized to f_0 *as* described in Chapter 3. The microphone sensitivity was obtained by referencing the signal measured from a constant amplitude sound source to the response of a standard reference microphone and was characterized as a function of frequency, signal intensity, and relative humidity.

4.3 Experiments

Experiments were performed on a few select systems to evaluate instrument performance. Initial measurements were made on O_2 in laboratory air, 20.95% by volume[8], at 300.0 K and 100.8 kPa. Subsequent measurements were made on samples of humidified CO_2 at 298.9 K and 99.88 kPa as well as trace CO_2 in laboratory air. A tunable single-mode external cavity diode lasers centered at $\lambda = 765$ nm for O_2 and $\lambda = 1590$ nm for CO_2 was used for these experiments. Line intensities, self- and air-broadening parameters, and Dicke narrowing parameters of Robichaud *et al.*[66] and Havey *et al.*[67] for the O_2 *A*-band as well as line intensities and broadening parameters of Toth *et al.* for CO_2[13] were exploited due to their well-established history and character. Galatry profiles[70] were used to fit the measured PAS O_2 *A*-band spectra. Contributions to the measured absorption coefficients from higher-order line shape effects, such as line mixing, are assumed to be small relative to the 1% combined uncertainty in our instrument response[11] and are not incorporated into this data analysis.

Measurements were also made on soot aerosols having mobility diameters (d_m) of 100, 150 and 200 nm. Details on the experimental apparatus used to generate and classify the soot are described in Chapter 2. An ethylene fueled laminar diffusion flame was used to generate soot particles.[39] Soot was then transported to a DMA for size characterization and classification. Prior to passing through the DMA, the soot particles passed through an aerosol neutralizer containing ^{210}Po in order to place a Boltzman distribution of net +1 charges on the particles.[71] A DMA separates particles by balancing the drag force and the electrical force on the particles as described in Chapter 2. The voltage on the DMA was set to correspond to constant 100, 150 or 200 nm mobility sized particles. After passing through the DMA, particles were analyzed with the PASm using a 405 nm multimode diode laser and then sent to a CPC to measure particle concentration. The DMA was calibrated with

NIST SRM® 1964 (60 nm polystyrene latex spheres) which has a relative combined standard uncertainty in mobility diameter of ± 0.5%.[72]

4.4 Results

This study aims to evaluate the performance of the custom built, first principles NIST PASm for measurements of greenhouse gases and atmospherically relevant aerosol. Performance criteria consist of instrument accuracy, precision, response time, and detection limit. Success is also pinned to the ability to predict the resonator response over a range of sample compositions, temperature, and pressure conditions.[11]

The ultimate level to which optical absorption coefficients can be measured is shown by the Allan deviations in Fig. 4.3.[12] Gas measurements were conducted by measuring the absorption signal at line center of the ${}^{P}P(9)$ transition at 13,091.710 cm^{-1} in the O_2 *A*-band with ~ 3 mW peak-to-peak power. Aerosol measurements were made on a flowing stream of 100 nm ± 1 nm mobility diameter soot particles with ~ 200 mW peak-to-peak power. Both datasets were generated by measuring sample absorption for two hours at uniform intervals of 0.1 s. For a 60 s averaging time, our detection limits, given by the product of power and absorption coefficient $\alpha_{\min}W_{PP}$, were measured to be $4\mathrm{x}10^{-10}$ $\mathrm{W{\cdot}cm^{-1}}$ for the O_2 *A*-band and $2\mathrm{x}10^{-9}$ $\mathrm{W{\cdot}cm^{-1}}$ for soot particles. The minimum in the Allan deviation, corresponding to the optimal short-term averaging time, occurs between 50 s and 100 s for measurements of the O_2 *A*-band and between 100 s and 300 s for soot particles. The differences in the Allan deviation plots are most likely caused by two factors: (1) increased random noise generated by a fluctuating aerosol source (see Fig. 4.3 inset) and (2) the relatively narrow O_2 absorption lines compared to the spectrally broad aerosol absorption signatures. For soot, the latter effect reduces sensitivity to laser frequency drift and allows for longer averaging times. These datasets suggest impressive single-pass detection limits when combined with lasers having continuous-wave powers greater than 1 W.

A comparison of detection limits for a selection of literature PAS instruments is shown in Table 4.1.

Table 4.1. Some literature PAS detection limits of comparable magnitude are tabulated. The sensitivity of PAS instruments for measuring aerosol particles is sample limited not instrument limited. Further, gas sample performance metrics should not be used for predicting aerosol sample capabilities and vice versa. [a]Authors understate their capabilities; see Kosterev et al.[1] [b]Detection limit calculation assumes a peak-to-peak power of 8 W with square-wave modulation and is converted to a 1σ value for comparison against the present work and published values by Arnott et al.[2-4]

PAS Reference	**Year**	**Gas Detection Limit ($W\text{-}cm^{-1}\text{-}Hz^{-1/2}$)**	**Aerosol Detection Limit ($W\text{-}cm^{-1}\text{-}Hz^{-1/2}$)**
Pushkarsky *et al.*[a,73]	(2003)	2.2×10^{-9}	-
Miklos *et al.*[74]	(2006)	3.3×10^{-9}	-
Kosterev *et al.*[1]	(2005)	5.4×10^{-9}	-
Present Study	(2010)	3.1×10^{-9}	1.5×10^{-8}
Arnott *et al.*[4]	(2006)	-	2.0×10^{-8}
Lack *et al.*[b,60]	(2006)	-	3.1×10^{-8}
Arnott *et al.*[3]	(1999)	-	6.8×10^{-8}

The sensitivity of this standard spectrometer compares favorably with respect to numerous other research groups utilizing PASm for many different applications.[1, 3, 4, 60, 73, 74] It is notable that PAS measurements targeted to gas phase applications typically have lower detection limits than those made on aerosols, validating the complexity and variability of aerosol systems. In essence, what works for gases does not necessarily work for aerosols and vice versa. Independent operating considerations are required when transitioning from the gas phase to the aerosol phase. A critical point, not obvious in the instrument precision analysis, is that the accuracy of this PASm is directly linked to the first principles model developed by Gillis, Hodges and Havey with a relative combined uncertainty of 1%.[11] Apart from characterization of the laser power and the microphone, no instrumental calibration is required to characterize the PASm system response.

Measurement precision is influenced by a combination of signal-to-noise ratio, data acquisition rate, and data analysis. With these considerations in mind, the manner in which high-precision data is generated is very different for gases and particles. Additionally, the performance criteria-per-analyte system is only relevant within the context of that analyte. Two gases (O_2 and CO_2) were used as calibrants. Initially, measurements of humidified CO_2 (20-30% RH) at 298.9 K and 99.88 kPa were conducted in order to show that high-precision measurements can be made with the NIST PASm on other systems than the previously mentioned O_2 calibrant. Measurements were made at line center of two transitions, R22e at 6363.726 cm^{-1} and R20e at 6362.504 cm^{-1}, within the $(30^01)\leftarrow(00^01)$ global combination band. The signal-to-noise level, defined as the peak absorption divided by the standard deviation of the spectrally detuned baseline, was ≈ 1800:1. Absorption coefficients for two transitions were measured over 1 hour. The spectra modeled with Voigt profiles using the line parameters of Toth *et al.*[13] and the data was temperature corrected to a reference temperature of 296 K to account for the temperature dependence of the line intensity. Results are shown in Fig. 4.4. For any given observation, measurement precision was approximately 0.13% while the relative combined standard uncertainty in the absolute absorption coefficient was 1.1%.

Additional measurements were made on trace CO_2 in ambient laboratory air. The goal of these experiments was to see if the instrument could potentially act as a point-source greenhouse gas sensor. The 1% relative combined uncertainty of our calibrated and modeled resonator response[11] potentially enables a PAS-based sensor to compete directly with existing state-of-the-art spectroscopic greenhouse gas detectors. The local absorption coefficient for the peak of the $(30^01)\leftarrow(00^01)$ R22e transition at ambient conditions is approximately $6.6\text{x}10^{-7}$ cm^{-1}, assuming a nominal CO_2 mole fraction of 385 ppm.[13] Using the measured gas detection limit of $\alpha_{\min}W_{PP}$ = $4\text{x}10^{-10}$ $\text{W}\cdot\text{cm}^{-1}$ and diode laser peak-to-peak power of 2 mW a minimum detectable absorption coefficient of $5\text{x}10^{-7}$ cm^{-1} can be predicted. In regards to these limits, this particular application pushes the limits of this NIST PASm. A series of measurements were made at line center, 6363.504 cm^{-1} and detuned from resonance. The measured CO_2 mole fraction was 466 ppm ± 32 ppm for 3 sets of 10 measurements with 60 s averaging windows taken over a one week time period. To validate these results this same transition using frequency-stabilized cavity ring-down spectroscopy[75] to measure the mole fraction of CO_2 in air was probed, again averaged over a one week time period, to be 463 ppm ± 15 ppm. Stated uncertainties are relative combined standard values for both measurements. The PAS and CRDS measurements are consistent. Therefore, with higher laser powers or reduced levels of microphone noise, one should be able to utilize this standard PASm to produce an affordable point-source CO_2 greenhouse gas sensor operating under atmospheric conditions.

The radiative properties of soot are atmospherically relevant but cannot be readily predicted from first principles. Likewise the required optical measurements on soot are challenging. Both models and measurements must account for the fact that soot can vary in size, morphology, mixing state, and chemical composition, which all depend on generation and flow conditions. These aspects directly affect optical properties and consequently measurements are required over a wide range of conditions. To address these measurement requirements, instruments for quantifying aerosol radiative properties need to have certain attributes: (1) rapid response time, (2) sensitivity to distinguish changes in size, shape, and chemical composition, (3) durability, and (4) capability to operate under convenient conditions (e.g. ambient). Several experiments were performed to evaluate how the NIST standard PASm behaves in this context for measurements of absorbing aerosols. A flowing sample of 100 nm ± 1 nm soot particles, as described previously, was directed into the PASm and monitored for a period of 5 h. During this time, the modulated power of a multimode the 405 nm diode laser used for the aerosol measurements, particle concentration, and PAS microphone signal were continuously logged in 60 s integration windows. Four sets of data were collected to generate multiple long-term datasets. Figure 4.5 shows the results for two of the datasets. Within a given 5 h dataset the 1σ measurement precision for the normalized PAS signal was approximately 1.5%. Of the four datasets, the day-to-day reproducibility of the mean normalized PAS signal was on the order of 10%, which, for aerosol based experiments, is consistent with the 10% component uncertainty from the CPC used (bottom right of Figure 4.5).

Finally, measurements were made on both 150 and 200 nm soot particles coated with dibutyl phthalate (DBP). Soot was sent through a heated coating chamber containing a material saturated with the DBP. Details of the coating procedure can be found in Chapter 3. DBP has a low vapor pressure and does not absorb at 405 nm making it a useful surrogate for atmospheric species such as $H_2SO_{4(aq)}$, which can coat atmospheric aerosol particles. Several groups have now quantified increased absorption of soot particles from the presence of a non-absorbing coating.[33, 76, 77] In regards to these experiments, soot was coated with the smallest amount of DBP that the coating apparatus can currently provide and measure the change in the normalized PAS signal introduced by the non-absorbing coating. Figure (4.6) contains these results. The short-term precision, as described previously, is more than adequate for resolving enhanced absorption for coating shell thicknesses,

$$\frac{(d_{m,coated} - d_{m,uncoated})}{2} \tag{4.1}$$

less than 10 nm which is defined by Eq. 4.1 where $d_{m,coated}$ is the mobility diameter of the coated soot and $d_{m,uncoated}$ is the mobility diameter of the uncoated soot. Mie theory calculations for coated spheres[15] were performed in order to determine the minimal detectability of the coatings on the soot. Calculations assumed $m_1 = 1.55 + 0.8i$ and $m_2 = 1.5 + 0i$ for the soot core and DBP coating, respectively, where m is the complex refractive index of the material. The change in particle absorption cross section, $\Delta\sigma(t_c)$ of a coated particle relative to that of an uncoated 100 nm soot particle was calculated for shell thickness values, t_c, ranging from 1 nm to 50 nm. In order to determine the minimum detectable change in absorption cross section, the $\Delta\sigma(t_c) = \alpha_{\min}/N$ was calculated, where N is the soot particle number density. Figure 4.7 shows a series of results (expressed as minimum coating thickness) assuming $\alpha_{\min} W_{PP} = 2\mathrm{x}10^{-9}$ W·cm^{-1} for $N = 10^5$, 10^3, and 10^1 particles cm^{-3}. Assuming that the effective thickness of a monolayer of DPB is between 0.1 nm and 1 nm, the PASm can resolve sub-monolayer coverage on a sample of 10^5 particles/cm^3 for modulated laser powers higher than 0.01 W to 0.1 W. In other words, for laser powers approaching 10 W this analysis suggests the ability to resolve absorption enhancement for a 500 nm thick coating on a single particle in the spectrometer. Interestingly, these power levels are achievable given what others[60, 78] have demonstrated utilizing multi-pass PAS configurations. Utilizing these approaches in tandem may open up new ways of probing particle interfaces to better understand problems relating to atmospheric and climate chemistry.

4.5 Conclusions

A newly developed NIST standard PASm has been characterized within the context of some important atmospheric components. For measurements of CO_2, the ability to perform precise and accurate spectroscopic measurements by comparison with known CO_2 line parameters[13] has been demonstrated. A proof-of-concept experiment was conducted which confirmed the potential of PAS to act as a point-source greenhouse gas sensor. Light absorbing soot was measured in the laboratory with PAS yielding 1σ precision of $< 1\%$ and 1.5% for short- (1 h) and long-term (5

h) averaging, respectively. Detection limits for 60 s averaging times were measured to be 4×10^{-10} W/cm for a gas and 2×10^{-9} W/cm for an aerosol, the latter quantity being limited primarily by generation, classification, and measurement of the aerosol number density. This sensitivity was exploited for measurements of coated soot. Absorption based enhancements from < 10 nm thick non-absorbing coatings on 150 nm and 200 nm soot particles were measured. Mie theory calculations suggest a minimum detectable coating thickness at the angstrom level for 100 nm particles, aerosol concentrations of order 10^5 particles/cm^3, and modulated power levels of 0.01 W to 0.1 W. Results show that a standard spectrometer with characteristics as described in Chapter 2 is well suited for measuring atmospherically relevant gases and aerosols.

4.6 Figures

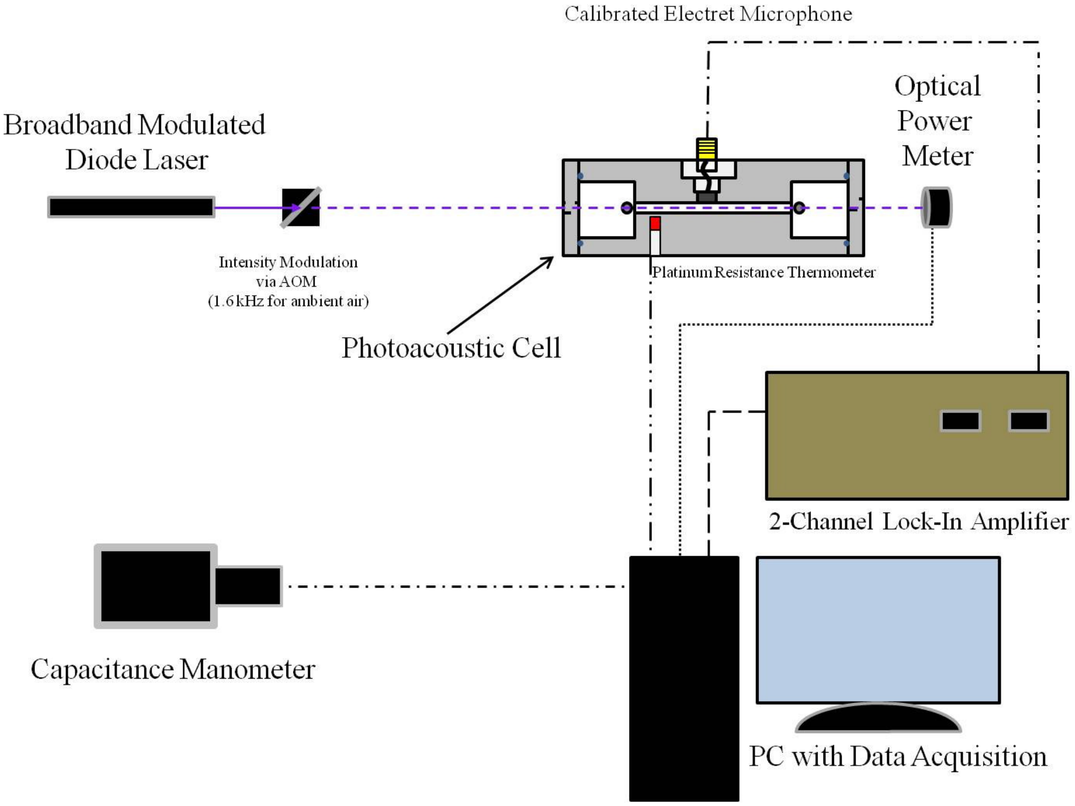

Figure 4.1. A schematic of a simple PAS experiment using the NIST spectrometer is shown

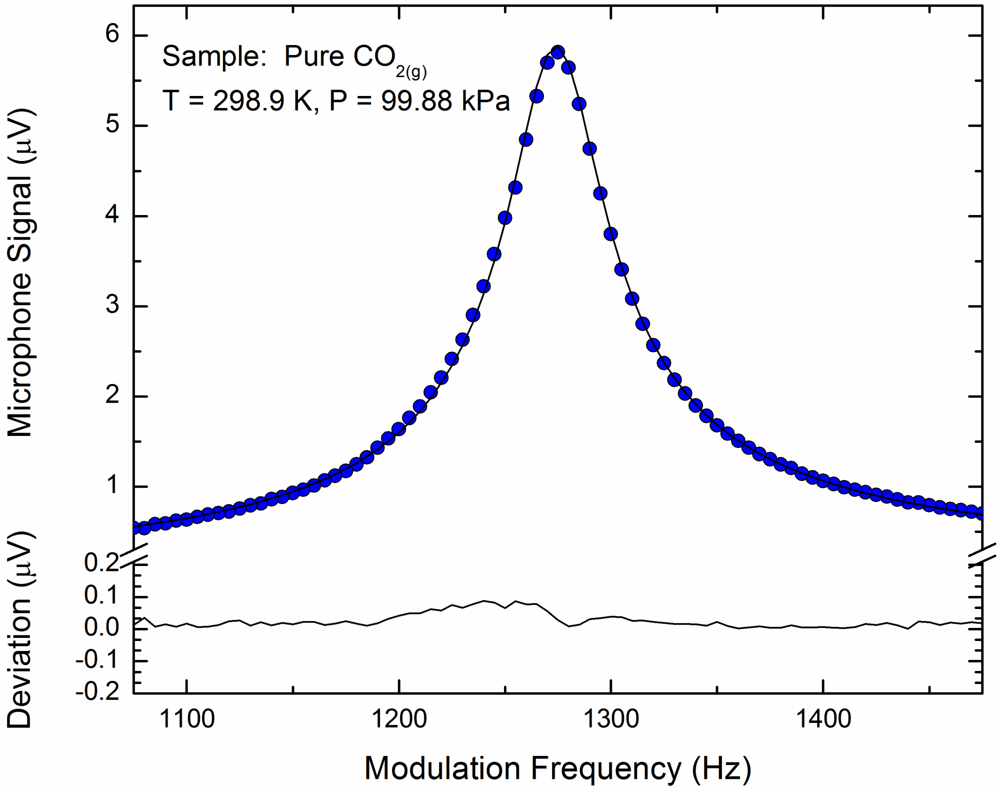

Figure 4.2. An acoustic resonance fit for CO_2 yielding f_0 = 1273.6 Hz and Q = 28.8 is presented. The complex resonance function $x + iy = \frac{-Af}{f^2 - (f_r + ig_r\sqrt{\tilde{f}/f})^2} + B + C(f - \tilde{f})$ was fit to the data as described in Gillis *et al.*[11]

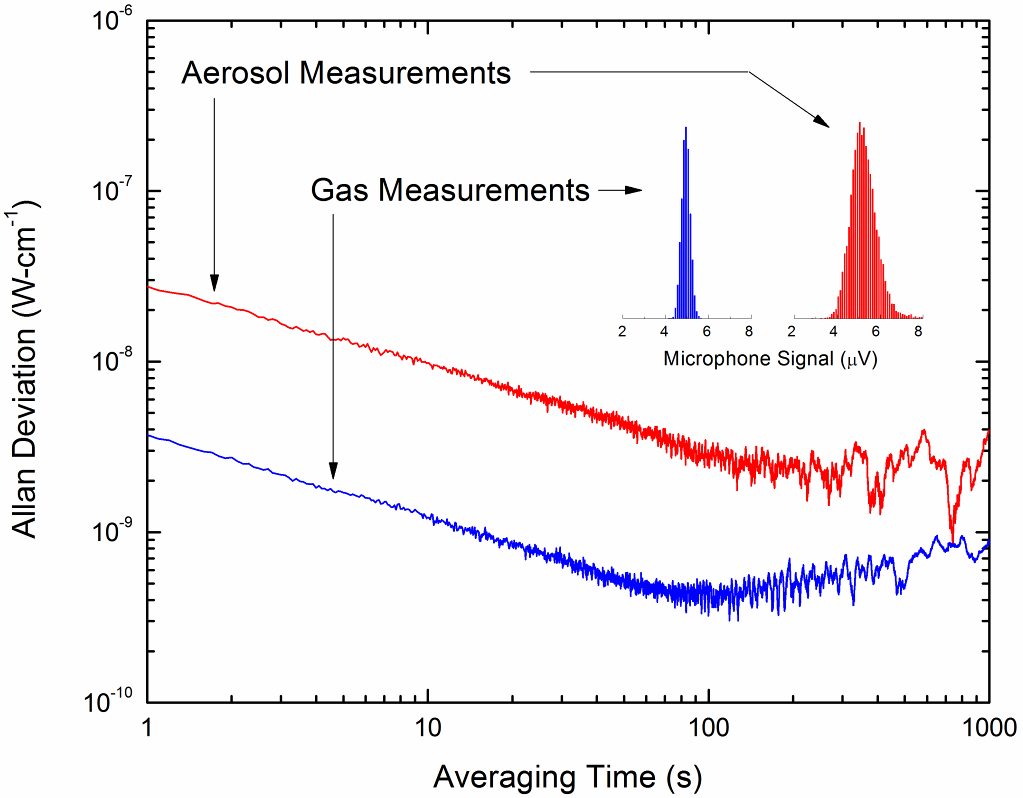

Figure 4.3. Power normalized Allan deviations (square root of the Allan variance[12]) are shown for absorption measurements at line center of the ${}^{P}P(9)$ transition at 13,091.710 cm^{-1} in the O_2 *A*-band at 300.0 K and 100.8 kPa (blue) and for 100 nm ± 1 nm soot particles at 100.3 kPa and 295.9 K (red). Measurements of the O_2 *A*-band utilized a 765 nm single-mode external cavity diode laser with peak-to-peak modulated power of ~ 3 mW; soot aerosol measurements utilized a 405 nm multimode diode laser with ~ 200 mW of peak-to-peak power. Instrumental detection limits for 60 s averaging times are 4×10^{-10} W·cm^{-1} for gases and 2×10^{-9} W·cm^{-1} for aerosols.

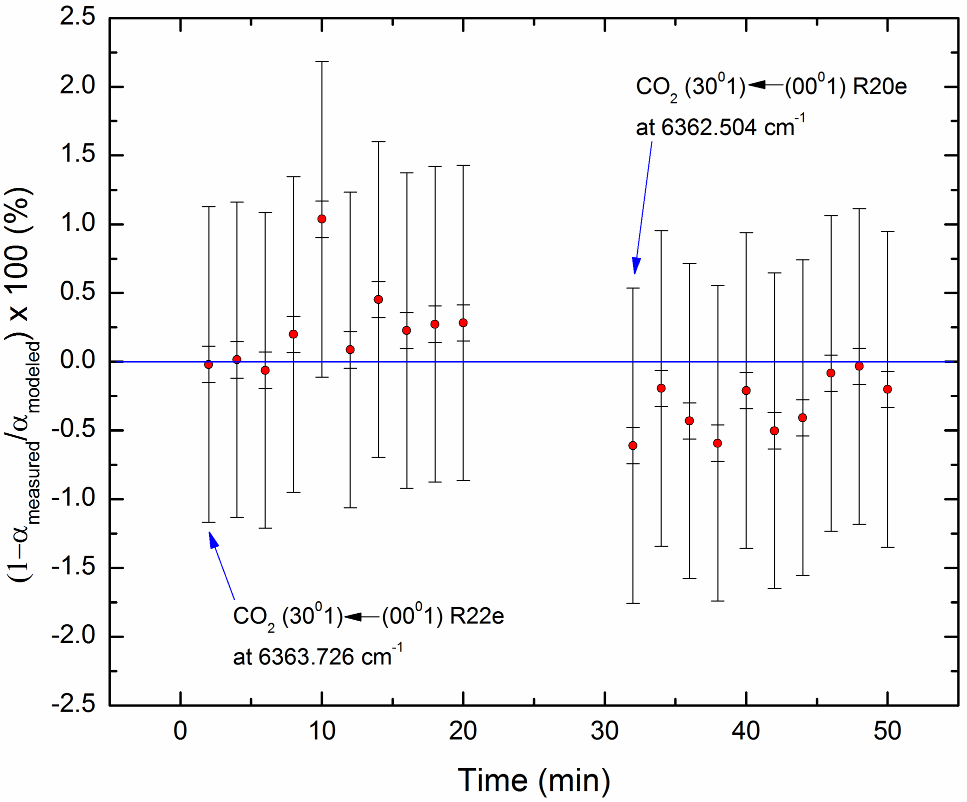

Figure 4.4. Differences between measured and modeled absorption coefficients for measurements of two CO_2 transitions within the $(30^01)\leftarrow(00^01)$ combination band are presented. Modeled absorption coefficients utilized Voigt profiles with the line parameters of Toth *et al.*[13] PAS measurements were made on humidified CO_2 at 298.9 K and 99.88 kPa with signal-to-noise ratios of ~1800:1 for 2 mW of peak-to-peak modulated laser power. Presented error bars correspond to relative combined standard uncertainties (outer bars) containing contributions from random components (inner bars) and systematic uncertainties in system constant,[11] temperature, pressure, and power.

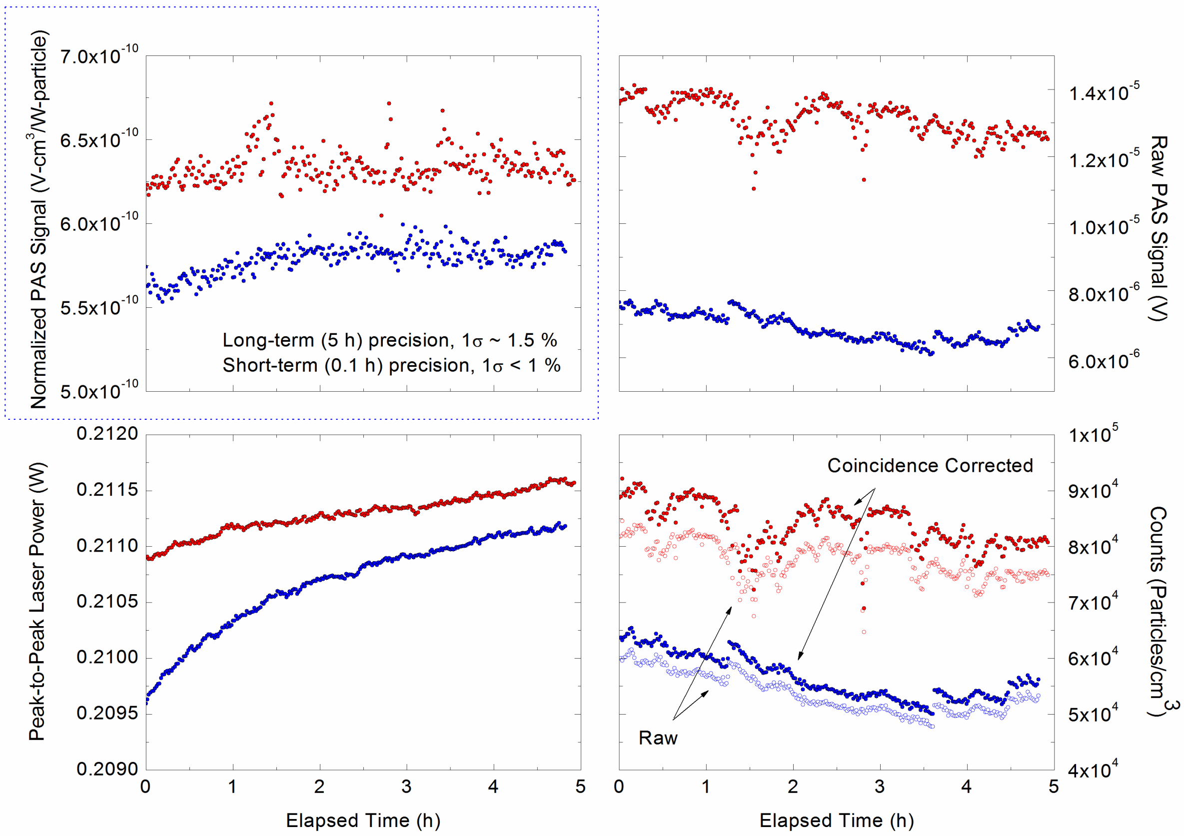

Figure 4.5. Measured PAS signals normalized for power and counts are shown for flowing samples of 100 nm ± 1 nm soot particles. A coincidence correction to measured particle concentrations was performed to account for particle shielding effects in a condensation particle counter by iteratively solving the equation $\frac{N_T}{N_M} = e^{(-N_T q t_c)}$ until results converged to better than 0.5%[14]; here N_T is the true particle concentration, N_M is the measured particle concentration, q is the volumetric flow rate, and t_c is the measurement time for a condensation particle counter. Our measured long-term (5 h) 1σ measurement precision is 1.5% despite dynamic soot particle number densities

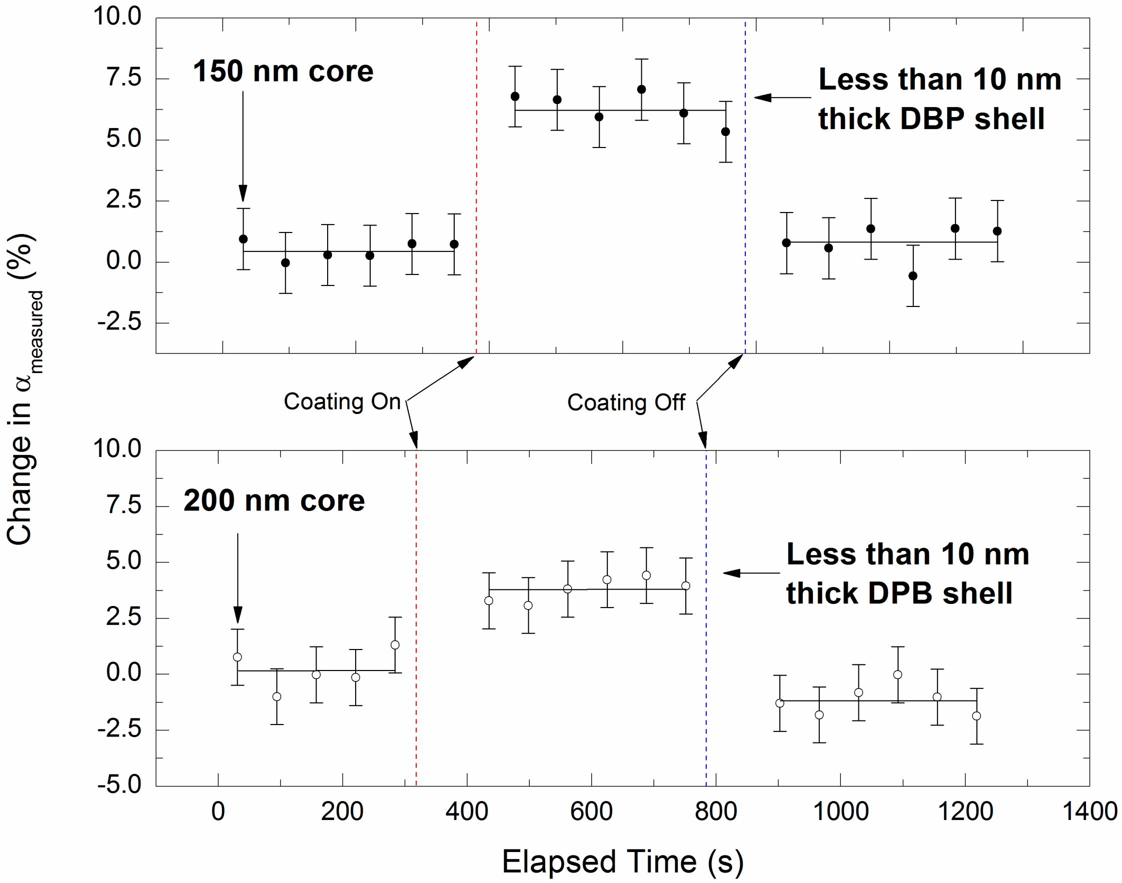

Figure 4.6. Measured relative changes in absorption coefficient are presented for measurements of 150 nm and 200 nm soot particles coated with < 10 nm thick shells of dibutyl phthalate (DBP); this is the smallest amount we can currently apply. Presented uncertainties correspond to $\sigma\alpha_{measured}/\sqrt{n}$ where $\sigma\alpha_{measured}$ is the standard deviation of the measured absorption coefficient and *n* is the number of observations.

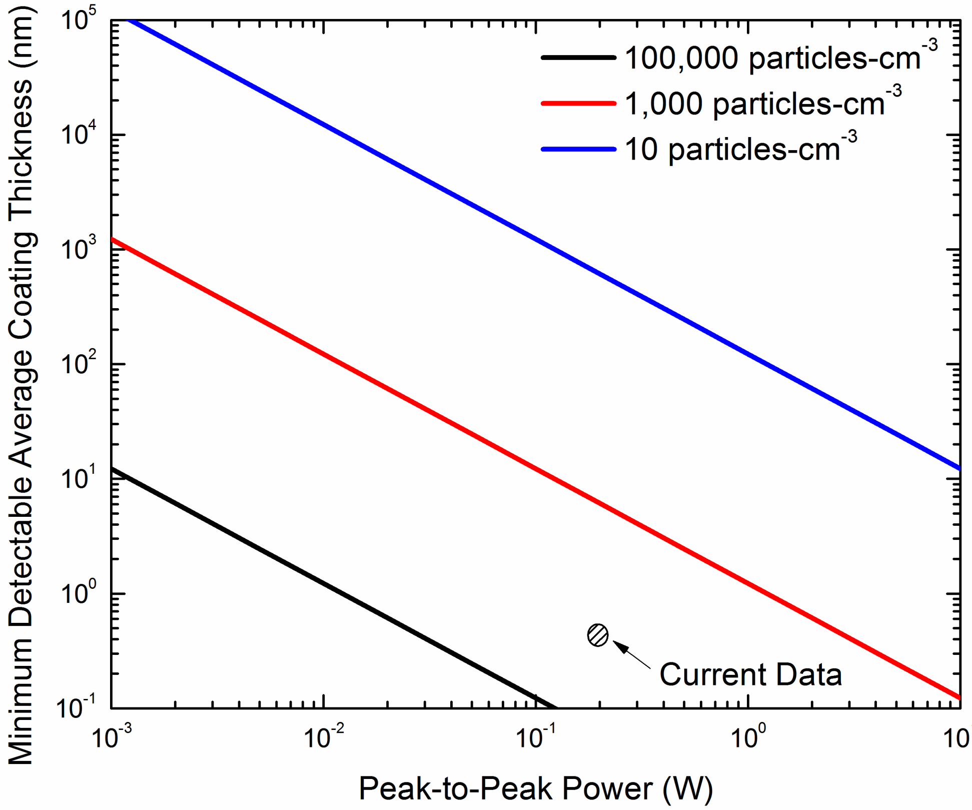

Figure 4.7. Minimum detectable average DBP coating thickness on 100 nm soot particles as a function of peak-to-peak laser power is shown. "Current Data" point represents the typical operating conditions, ~60,000 particles-cm^3 and 0.2 W peak-to-peak power, utilized in the present work. Lorenz-Mie theory calculations for coated spheres were performed using the code of Bohren and Huffman.[15] We assumed $m_1 = 1.55 + 0.8i$ and $m_2=1.5 + 0i$ for the complex index of refraction for soot and DBP, respectively. Predicted absorption enhancements over a range of shell thicknesses were calculated for samples of 10^5, 10^3, and 10^1 particles·cm^{-3} and compared against our measured detection limit of $\alpha_{min}W_{PP} = 2x10^{-9}$ W·cm^{-1} for a 60 s averaging time.

Chapter 5: Direct Measurement of the Absorption Cross-Section of Uncoated and Coated Soot by Photoacoustic Spectroscopy

5.1 Introduction

Soot is the principal light absorbing atmospheric aerosol.[79] Sometimes referred to as black carbon, soot is composed of graphitic carbon, as well as other organic compounds. Soot is not a uniquely defined material chemically or in terms of size distribution so that it is difficult to accurately assess its chemical and global warming impact. While the exact impact of soot on the atmosphere is still under investigation, it is well established that soot acts as a warming component to the atmosphere. [80] The exact contribution that soot imparts to the overall energy balance to the atmosphere is as yet an unresolved question. The latest IPCC charts still show a large uncertainty in the contribution soot and other light absorbing particles have on the atmosphere. [80] In fact, the contribution by particles that warm the atmosphere is masked by the contribution of other particles (Fig. 5.1). Most atmospheric aerosols reflect (or scatter) incoming radiation, which has a cooling effect (negative radiative forcing). The warming effect (positive radiative forcing) is effectively unique to soot, which has lead to its prominence as a greenhouse component. With a positive forcing on the order of 0.5 Wm^{-2}, only carbon dioxide warms the atmosphere more. [81]

It is understood that soot ages when released into the atmosphere. [38, 82] This process usually involves the oxidation of the particles and eventual coating by chemicals found in the atmosphere. One of the most common coatings found on soot is sulfuric acid,[83] which while weakly-absorbing in the visible, may influence the effective absorption efficiency of soot. [17, 25, 79] The aging of the soot leads to several possible mixing states, including core-shell states, externally mixed states and internally mixed states. The core-shell state that appears to be the most prevalent for aged soot [25] and the experimental model used in this study. It has been shown that the coating of soot with sulfuric acid and subsequent hygroscopic growth due to interactions in the atmosphere lead to definite enhancement of the optical properties of the particles. Inclusive of this enhancement, it has been shown that the absorption can nearly double due to the coating process. [36]

Soot, with its fractal structure[84],as seen in Fig. 5.2, is good at agglomerating other substances onto its surface. [85]. This is the end result observed as emissions from incomplete fossil fuel combustion and biomass burning. Typically, soot is an arrangement of smaller sub-units linked into a larger particle.

The majority of the soot particle is elemental carbon, appearing in a graphitic form, which allows for gaps and exposed unpaired electrons that can attract other compounds; such as oxygen, nitrogen, and hydrogen. These imperfections in the structure allow for other substances to agglomerate and ultimately to form an organic layer around the particle. This agglomeration enables the normally insoluble particle to dissolve in water. [86] Within this morphology, the carbon portion of soot can exist in several basic forms. The different forms have been modeled to show different atmospheric impacts. The three proposed models of atmospheric aerosols by Jacobson are seen in the Fig. 5.3. One species is well mixed with the surrounding compounds (which is referred to as internally mixed), another is co-existing, but not well mixed with the surrounding environment (which is known as externally mixed) and the third as a core for a particle with a variably mixed shell.[87] The latter mixing state gives the absorptive properties of soot their particular radiative effects which will be investigated in this experiment. The effects of these different forms were modeled and it was found that the radiative forcing effects lie between +0.27 Wm^{-2} and +0.54 Wm^{-2}.[87]

Several other groups have done similar work regarding the amplification of absorbing cores with non-absorbing coatings. Their findings are summarized in Table 5.1.

Table 5.1: Summary of other authors' findings regarding absorption amplification of absorbing cores with non-absorbing coatings.

Author	**λ**	**Core Material**	**Coating Material**	**Method of Attaining Absorption**	**Amplification**
Schnaiter[34]	200-1000	BC internally mixed (diesel soot)	SOA	Long path extinction cell/Nephelometer	1.8-2.1
Slowik[35]	870/670	Premixed ethylene flame	Oleic acid/ Anthracene	PAS/MAAP	1.65
Gangl[32]	530/650	Spark discharge soot	Carnauba wax	MPASS/Nephelometer	≈1.8
Zhang	532	Diffusion flame propane	H_2SO_4 and H_2O	CRDS/Nephelometer	2
Khalizov	532	Diffusion flame acetylene	H_2SO_4 and H_2O	CRDS/Nephelometer	1.4
Lack	532	BPSL	Oleic acid	PAS/CRDS	1.4
Xue	532	Propane diffusion flame	Dicarboxylic acid	CRDS/Nephelometer	< 1.2
Shiraiwa	532	Graphite	Oleic acid and Glycerol	PAS	2

These findings span a large range of amplifications from less than 1.2 times to more than twice the uncoated absorption. The methods involved are primarily indirect in that they involve both an extinction and scattering method requiring the difference of those two methods in order to determine the absorption.

The work presented within this chapter demonstrates that the direct measurement of the absorption cross-section of both uncoated and coated soot with a PASm was accomplished and fits within the findings shown in Table 5.1.

5.2 Experimental

5.2.1 Experimental Outline

This experiment was two-fold in execution. Initially, evidence of amplification of the C_{abs} for soot by a non-absorbing coating was needed in order to justify a further refined experiment. To do this, soot of several mobility diameters (100, 150 and 200 nm) were generated with a diffusion flame burner and size selected with a differential mobility analyzer (DMA). These selected soot particles were then sent to a photo-acoustic spectrometer (PASm) for analysis. Once this measurement was complete, the same mobility size soot was generated, size selected and then coated with a non-absorbing coating. These coated particles were again sent to the PASm for analysis, and the results were compared to the uncoated soot. These soots were coated under the same conditions, and the only variable was the coating thickness, dictated by the coating apparatus temperature. The results showed amplification in the $C_{abs.}$ The second portion of this experiment was done to further refine the single DMA (SDMA) data by in addition to size selecting the core with the first DMA; a second DMA was used to select the coated particle size. A tandem DMA (TDMA) mode was set up in order filter both the uncoated and coated particle populations in order to realize a refined C_{abs} for all the uncoated and coated particle sets. Surprisingly, the accuracy of the simpler, SDMA measurements was found to be higher than those of the TDMA measurements. The details of these experiments and their results are presented below.

5.2.2 Soot Generation

The experiment is comprised of a soot generation/classification system, a soot-coating chamber, and a photo-acoustic spectrometer as seen in Fig. 5.4. The soot is generated in a Santoro style diffusion burner[39] and sampled via a sampling probe method described by Kim et al.[88] Particle free air is delivered at 5 LPM orthogonally to the flame. An ejector pump downstream of the sampling probe creates a low-pressure region in the direction of the soot flow. In turn, this low-pressure region creates a pressure difference at the flame tip, which draws the flame into a 1 mm hole in the sampling probe at the flame-probe interface. The soot is carried to a 5 L accumulation chamber where the fresh soot is allowed to agglomerate in order to increase the diameter at the peak of the size distribution. From that point the soot flows through an ejector pump to the classification system for a total flow rate of 30 LPM after the ejector pump. Particles are sampled from this flow to the DMA for characterization and PASm for analysis.

5.2.3 Size Classification

Differential mobility analysis is used for separating particles based on electrical mobility and for this purpose is used as both a characterization and preparation tool [43]. The basic concept behind particle preparation is to use DMA_1 to size select bare soot, while DMA_2 is used in the TDMA experiment to further refine the uncoated cores and to size select the coated soot. The soot particles initially pass through an aerosol neutralizer (^{210}Po) and then are mobility selected with DMA_1 (TSI Model 3081), to generate the core size of interest. These size selected core particles are a narrow band of particles isolated from the full particle distribution shown in the inset of Fig. 5.5. These particles can be either sent to the PASm for analysis in the SDMA experiment, or to DMA_2 for further refinement or to the coating system. To further refine the particle population, the TDMA system is used with a second particle neutralizer in front of DMA_2.[88] Normally, a single particle neutralizer is placed in front of the inlet to the first DMA, which places a Boltzmann charge distribution on the polydispersed particle population. However, there are a percentage of doubly and even triply charged particles that are hidden within the major peak of singly charged particles that are initially size selected with DMA_1. These will have an impact on the measured absorption since they have more mass. In order to separate these multiply charged particles a second aerosol neutralizer is used to further distribute the charges on the particles prior to DMA_2. Figures 5.6 A, B and C show the resulting multimodal distributions of uncoated soot after a dual aerosol neutralizer is used for 100, 150 and 200 nm mobility diameter particles (respectively). In Fig. 5.6A, there are four clearly visible particle peaks where each peak represents a particular mobility size and above the peak, the original charge on the particle is shown, and what the charge becomes after re-neutralization. For example, the peak labeled 2 → 1 in Fig. 5.6A was a doubly charged particle that once re-neutralized, becomes a singly charged particle and consequently, after passing through DMA_2, appears at a larger mobility diameter.

The size selected distribution is comprised of a significant number of 150 nm and 200 nm doubly and triply charged particles in addition to the singly charged 100 nm particles. This deconvolution, however, can be repeated indefinitely, because some portion of the multiply charged particles will always exist in the monomobility distribution. One of two methods can be employed to better represent the size distribution of particles that are analyzed by the PASm. One approach is to correct the PASm signal to account for the size distribution. Another approach, and the one employed in this analysis, is to correct the particle diameter to account for the size distribution actually seen by the PASm. For this, the diameter of average mass (d_{mass}) was calculated for both the SDMA and the TDMA data from the fractional component of singly and doubly charged particles per core size because absorption is mass dependent. The d_{mass} is defined as the equivalent sphere diameter representative of the average mass of particles in any particle distribution. How the d_{mass} is calculated is described below. These charge fractions were obtained by using a condensation particle counter (CPC) and an electrometer to count particles and charges exiting the DMA. A relative calibration of the electrometer to the CPC was carried out by generating 99.8% singly charged, 15 nm sucrose aerosol using electrospray. Particles with more than two charges were not included in the analysis due to the generally minimal number of those particles; however, the impact on the results for the smallest core size is treated in the uncertainty section. The difference between the charge counts from the CPC and the charge counts from the electrometer gives a direct determination of the number of doubly charged particles. Table 5.2 presents the measured fractions for all core sizes used.

Table 5.1: Fraction of singly and doubly charged particles for both the SDMA and TDMA experiments.

Experimental Mode	**Charged Fraction**	**d_m (nm)**		
		100	**150**	**200**
SDMA	Singly Charged	0.40	0.52	0.73
	Doubly Charged	0.60	0.48	0.27
TDMA	Singly Charged	0.96	0.94	1.0
	Doubly Charged	0.040	0.060	0.0

5.2.4 Translating Mobility to Mass

Because optical measurements are mass based, a relationship between mass and mobility is needed. This is straightforward if the particles are spheres but more complicated for aggregates.

In order to translate mobility diameters to mass and then d_{mass}, several calculations are required. The translation is based on the work of Park *et al.*, [89] where the scaling exponent and the particle density were explored. The mobility mass ($Mass_{dm}$) is a product of the aggregate volume (V_a), calculated from the mobility diameter (d_m), scaling law exponent (D_{fm}), a pre-factor constant (C) and the density of the particle (ρ_p). Park *et al.* used 2.35 for the power law exponents and $7.35\text{x}10^{-21}$ as the mass pre-factor based on their specific diesel soot. While this would provide a reasonable estimate for the soot in this project, a method is available in order to calculate the power law exponent and the pre-factor that is derived directly from the photoacoustic signal and the mobility diameters measured in this experiment.

The TEM micrographs indicate that the soot is classically agglomerated and that the primary particles, which are nearly spherical, are nominally 20 nm in diameter. An estimate of the volume of these agglomerates in terms of d_m is required for the analysis of their optical absorption. In the Park *et al.* study [89] of diesel soot that incorporated both mass and differential mobility analyzers, showed that the particle mass and mobility diameter, d_m, can be correlated using a power scaling law. Similarly, we use the following relation between the aggregate volume, V_a, (which can be converted to the $Mass_{dm}$ with the particle density, ρ_p) and mobility diameter:

$$\frac{Mass_{d_m}}{\rho_p} = V_a = \frac{\pi {d_{se}}^3}{6} = C\left(\frac{d_m}{d_0}\right)^n \tag{5.1}$$

where n is the power-law exponent, d_{se} is the sphere-equivalent diameter, and C is the volume corresponding to $d_\mathrm{m} = d_0 = 1$ nm. Assuming the DMA system selects a bimodal distribution of singly charged and doubly charged aggregates of mobility diameters, $d_{\mathrm{m},1}$ and $d_{\mathrm{m},2}$, respectively, gives

$$d_{se} = \left\{C\left[f_1\left(\frac{d_m}{d_0}\right)^n + (1-f_1)\left(\frac{d_{m,2}}{d_0}\right)^n\right]\frac{6}{\pi}\right\}^{1/3} \tag{5.2}$$

in which the relative abundance of singly charged particles is specified by f_1. The preceding expression provides a simple relationship between the observed d_m and the d_{se} of the soot provided that the parameters C and η are known. Equation 5.3 describes the relationship between the calculated $Mass_{dm}$ and the mass equivalent diameter, d_{mass}:

$$d_{mass} = \left(\frac{6Mass_{d_m}}{\pi\rho}\right)^{(1/3)} \tag{5.3}$$

Below, it is shown how these two quantities can be determined by fitting this expression to measurements of soot mobility diameter and particle absorption cross-section.

For soot agglomerates comprised of primary particles whose characteristic dimensions are small compared to the wavelength of light, the total absorption by the particle cluster can be estimated by summing over the set of monomer absorption cross sections. In this approximation known as the Rayleigh-Debye-Gans (RDG) model, interactions between soot primary particles are not considered and their light absorption is treated as being independent of agglomerate morphology. By comparison with more general calculations of absorbing and scattering from soot clusters, Farias *et al.* [90] showed that the accuracy of the RDG approximation depends on the primary particle size parameter, $x_{pp} = \pi d_{pp}/\lambda$, complex refractive index, $m = m_r + i\, m_i$ and number of primary particles in the agglomerate, where d_{pp} is the primary particle diameter and λ is the optical wavelength. Under the assumption that $x_{pp} << 1$ (Rayleigh limit) the absorption cross section of a spherical monomer is given by

$$\sigma_{abs,pp} = \frac{4\pi x_{pp}^3}{k^2} Im\left(\frac{m^2-1}{m^2+2}\right) \tag{5.4}$$

where $= 2\pi/\lambda$. Summing over all primary particles gives the absorption cross-section of the agglomerate to be $\sigma_{abs} = N_{pp}\sigma_{abs,pp}$. After dividing Eq. 5.4 by the primary particle volume, it follows that the absorption cross-section per-unit-volume of agglomerate depends only on m and λ and is given by

$$\frac{\sigma_{abs}}{V_a} = 3k\ Im\left(\frac{m^2-1}{m^2+2}\right) \tag{5.5}$$

Note that the particle absorption coefficient is also given in terms of the experimentally PAS-measured absorption coefficient, denoted by α, divided by the measured particle number density, n, so that

$$\sigma_{abs} = \frac{\alpha}{n} \tag{5.6}$$

From Eqs. (5.1-5.6) we obtain,

$$\frac{\alpha}{n} = 3k\, Im\left(\frac{m^2-1}{m^2+2}\right) C\left[f_1\left(\frac{d_m}{d_0}\right)^n + (1-f_1)\left(\frac{d_{m,2}}{d_0}\right)^n\right] \tag{5.7}$$

Where the C and η coefficients were determined as well as a set of d_{se} soot core values by fitting the absorption model embodied in the right-hand-side of Eq. 5.7 to the measured values of α/n, d_{m1}, d_{m2} and f_1 obtained for uncoated soot. These data correspond to a total of six measurements: three for the SDMA and TDMA experiments, respectively. C, η were the only floated parameters used in the fitting procedure. In order to evaluate the foregoing expressions, a value of m consistent with previous ethylene soot measurements by Zhu *et al.* [91] were assumed. The assumed value of absorption coefficient was corrected to λ=405 nm to yield a mass-specific value of 10.88 $m^2\ g^{-1}$, which corresponds to $\sigma_{abs}/V_a = 0.0196\ nm^{-1}$ assuming a soot density of 1.8 $g\ cm^{-3}$. Given that m is complex, there is a family of m values of paired real and imaginary components that when substituted into Eq. 5.5 yield this wavelength-corrected value of σ_{abs}/V_a. Of these m values, the fit shown in Fig. 5.7 was based on $m = 1.51 + 0.9\ i$, which yielded $C = 2.528\ nm^3$ and $\eta = 2.285$. Importantly, the fitted exponent η is completely insensitive to the choice of m as is the flatness of the fitted σ_{abs}/V_a. These data strongly support the RDG assumption that leads to being independent of effective particle volume. However, changing m alters the fit-derived V_a and d_{se} for the various data points as well as the magnitude of the fitted σ_{abs}/V_a value. Setting the recommended value for m the value 1.55 + 0.8i, gives a result about 10% low of the value corresponding to the mass-specific absorption coefficients reported by Zhu *et al.* [91] Figure (5.7) also illustrates the expected σ_{abs}/V_a based on a Mie theory calculation of the absorption cross-section based upon the treating the agglomerate as a spherical particle. These data show that this approximation tends to overestimate the value of σ_{abs}/V_a for particles of effective diameter greater than about 40 nm.

Table 5.2 shows the results for d_{mass} for both experiments based on a density of 1.8 g/cm^3 [92, 93] and the V_a calculated previously. It should be noted the TDMA data show smaller average d_{mass} for all core sizes. This demonstrates that the second aerosol neutralizer reduces the fraction of doubly charged particles processed by DMA$_2$. These values will be used below in comparing Mie theory predictions with our results.

Table 5.2: Combined average mass diameter for the singly and doubly charged particles for both SDMA and TDMA experiment.

Mobility Diameter (nm)	**SDMA d_{mass} (nm)**	**TDMA d_{mass} (nm)**
98.2	70.2	56.9
151.2	94.2	79.8
201.7	107.7	96.3

While there are ultimately still some multiply charged particles passing through DMA_2, the amount is drastically reduced, therefore, the particle peak of interest is a more monomobility population than when using only a single aerosol charger. With this system, any changes made to the size selected soot can be observed by a change in the PASm signal in the SDMA experiment or by scanning the soot with DMA_2 in the TDMA experiment. Particle counts are made with a condensation particle counter (CPC) TSI model 3025A.

5.2.5 Coating System

The coating apparatus is located after DMA_1 for both experimental modes. The coater consists of a one meter long, 2.54 cm diameter stainless steel tube with a 0.32 cm thick polyester felt fabric inner wall liner saturated with the coating material. Due to the caustic nature of H_2SO_4, dibutyl phthalate (DBP) was used as the coating material. The DBP is non-absorbing at the wavelength of interest and has a low volatility, making it a good surrogate for the H_2SO_4 as well as other partially oxidized particle coatings in the atmosphere. The stainless steel tube is wrapped in heating tape, which is then wrapped in insulation to reduce temperature fluctuations. Temperature stability of the coating system was $\pm$ 0.1 K. The heating is controlled via proportional-integral-derivative controllers, and the temperature was measured at the wall of the tube as well as inside the tube in the particle flow. A bypass tube parallel to the coating tube allows the passage of soot along the same path as the coated soot without encountering any coating material. With an approximate 1.5 LPM of soot flow through the coating tube, the 11 s residence time allows the exiting gas to have a vapor pressure of at least 90% of the saturation vapor pressure of DBP at the set temperature. The length of tubing required to ensure adequate coating was based on diffusion plug flow calculations from Carslaw [94] and Hinds. [45] Immediately following the heated coating section, a chilled 0.3 m section of the same tube promotes heterogeneous condensation of the coating material onto the soot agglomerates. From this point, the coated particles are sent to the PASm for the SDMA experiment or sent to DMA_2 for scanning and characterization in the TDMA experiment.

The coating apparatus also acts as a charge separator because the temporal behavior of the coating process follows a heterogeneous growth law.[95] This phenomenon is exploited for the TDMA experiment. As the particles grow, the influence of the original core size becomes less pronounced, and the singly and doubly charged coated particles essentially grow toward the same size. This approximation is most valid for larger core particles, and larger coating thicknesses. The multiply charged, larger core coated particles exit the DMA at a smaller mobility diameter than the singly charged coated core particles, thus effectively isolating the singly charged coated core soot particles of interest. Figure 5.5 shows the size distribution measured by DMA_2 for uncoated 100 nm soot cores (the solid line) as well as coated particle distributions obtained at different coating conditions (dashed lines). The apparent bimodal distributions of the coated particles are an artifact of multiple charging rather than two distinct size modes. In order to provide credibility to the assumption that the bimodal distribution is due to multiply charged, single diameter particles, an adjusted mobility diameter for the larger peak was calculated assuming a doubly charged particle and the results show that the doubly charged peak appears where the experimentally smaller peak appears. While there is still some overlap in the coated particle distributions, especially for the smaller coatings, an estimation of the contribution by larger core particles can be made to properly assess the absorption properties of the particles of interest. This allows for a clean photo-acoustic measurement of the coated particles of interest. At this point, once the particles of interest are selected with the second DMA, the particles flow through the PAS system and then to the CPC for counting.

5.2.6 Photoacoustic Spectrometer

The PASm system used in this experiment is described in Chapter 3. The details on how the system operates and how the data are interpreted can be found there as well.

5.3 Results

5.3.1 Uncoated Soot

Differential mobility sized soot cores of 100, 150 and 200 nm were analyzed in the experiment. All core sizes were coated with different thicknesses of DBP ranging in size from 20 nm to over 150 nm. The coating thickness is defined as the difference between the coated particle mobility diameter and the initial uncoated average d_{mass} soot particle.

The uncoated soot mass absorption cross-section in m^2/g (MACs) for 100, 150 and 200 nm particles was computed. The MACs is the cross-sectional area per gram of soot that absorbs light and is the absorption cross section per particle divided by the mass of the particle. This quantity is calculated from the measured absorption cross-section and the $Mass_{dm}$, given by Eq. 5.1. The average MACs for both the SDMA and TDMA experiments of 10.8 m^2/g found in this experiment are within the bounds of previously reported MACs of 1.5 to 25.4 m^2/g for the products of incomplete combustion[96]and on par with the MACs reported specifically for several diffusion flame soot of 10.1 ± 0.5 m^2/g adjusted for wavelength,[93] 13.3 m^2/g adjusted for wavelength [97]and 11.4 m^2/g adjusted for wavelength [36]as reflected in Fig. 5.8.

In Fig. 5.8 both the SDMA and TDMA MACs are plotted for the three core average d_{mass}'s. Both the SDMA and the TDMA values essentially lie on the same horizontal line. This implies that the mobility to mass conversion is consistent for the two sets of data. Any significant deviation would imply that the conversion of the mobility of the aggregate to mass was problematic. Also plotted is the Mie theory calculation for the d_{mass} with an index of refraction of 1.51 + 0.9i. The Mie code used was based on Bohren and Huffman.[22] Shown in Fig. 5.8 are two ranges of reported MACs from Bond and Bergstrom[96] and Choi *et al.*[98] The Mie cross-section is significantly higher and may reflect an uncertainty in either the refractive index, limitations of Mie theory to accommodate agglomerates and/or errors in the mobility to mass conversion. The decrease in the Mie theory cross-section as a function of size reflects the effects of optical thickness in a sphere. This effect is not seen for our aggregates since to first order the total absorption in the experiment is the sum of individual absorption of the primary particles comprising the aggregate, which are individually in the thin absorption limit. To better determine the MACs, an independent measurement of particle mass would be required. However the purpose of this work is to evaluate the amplification effect and not a definitive determination of absorption cross-section for soot.

5.3.2 Coated Soot

Initially, a SDMA experiment was performed where a core size of soot was first size selected and then sent on to the PASm for analysis. Subsequently, the same particle population was sent from DMA_1 into the coating apparatus and then the PASm for analysis. This experiment was run at several different temperatures producing several coating thicknesses. Again, Fig. 5.5 shows an example of the coating thicknesses applied to the uncoated 100 nm soot. Fig. 5.9 shows the absolute values for the C_{abs} for both the SDMA and TDMA modes as a function of relative coating thickness defined as:

$$D_r(D_{coat}) = \frac{(d_m(coat) - d_{mass})}{d_{mass}} \tag{5.8}$$

It is clear that for all three SDMA core sizes (70, 94 and 108 nm), there is a monotonic increase in absorption cross-section with increasing coating thickness indicating that amplification is taking place. All coated particles exhibit amplification ranging from a few percent to nearly 90% as shown in Fig. 5.9. The key figure and major impact of this experiment is the low uncertainty/high accuracy of the amplification for the SDMA measurements. The uncertainty in the amplification is within the size of the plotted symbols. The slight variability in the amplification is thought to be from a slight change in the soot particles from day-to-day generation. There could also be a slight change in the width of the droplet distribution for a fixed peak size of the droplets.

The TDMA system employed a second aerosol neutralizer. The results are qualitatively consistent with the SDMA results and amplification of the C_{abs} is seen in all the cases with values ranging from several percent to nearly 70% amplification. Surprisingly and as indicated by the larger error bars, the measurement repeatability is not as good for the TDMA measurements. In all three SDMA core sizes, the absorption amplification increases with the reduced coating thickness, while for the TDMA decreases and then increases with increasing coating thickness. The cause of this apparently anomalous result is likely a combination of the effects described below. The accuracy of the absorption measurements is better for the SDMA because of the approximate order of magnitude higher concentration. Secondly, there is a difference in the charge fraction for the uncoated and coated particles. This will have the largest effect for small coating thicknesses. The third reason relates to the measurement of the absorption cross-section of the uncoated particle. For the SDMA, this measurement is made within minutes of the measurement for the coated particle. For the TDMA, there is a longer delay because the TDMA must be reconfigured for the coating measurement. In fact, typically the value for the uncoated soot for the TDMA is the average of measurements made on several days. This leads to a larger uncertainty in the amplification because of the 12% standard deviation in the repeatability measurements of the absorption cross-section with the TDMA method.

Figure 5.10 demonstrates consistency between theory and measurements for SDMA. The Mie code [22] used requires a core size input (the d_{mass}) and a total coated particle diameter (d_r) as well as an index of refraction for both the core and the coating (1.51 + 0.9i and 1.495, respectively). The solid and dashed lines in Figure

5.10 are the theoretical amplifications at several reasonably possible indices of refraction ranging from 2.0 + 1.0i to 1.3 + 0.3i [96] with the assumed index of refraction of 1.51 + 0.9i for this specific soot. All the lines modeled in Fig. 5.10 increase upon the onset of amplification; therefore, amplification occurs in all cases, regardless of the index of refraction modeled or the coating thickness. Again this result is consistent with the SDMA and TDMA measurements.

5.3.3 TEM Characterization

Coated and uncoated soot were collected on TEM grids with a nano-aerosol sampler (TSI Model 3089) to observe the effect of coating on the soot particles. Figure 5.11 is a set of TEM images of uncoated (upper quadrants) and coated 150 nm (lower quadrants) mobility selected soot particles. The TEM images were taken with a cold stage mode on a JEOL Jem 2100 Microscope. The temperature was maintained at -167 °C for both the uncoated and coated particles. Figure 5.11 clearly shows soot aggregates. Figure 5.11 shows 150 nm mobility selected soot, which was coated with DBP to a total particle size of 320 nm. The aggregates in Fig. 5.11 (lower quadrants) are collapsed and show a more spherical morphology than the uncoated particles in the upper quadrants. While visual evidence of the coating material is not obvious, the aggregate collapse and the fact that the particles were collected while DMA2 was set to only allow 320 nm particles is clear indication that the particles were indeed coated.

5.3.4 Uncertainty

Several sources of uncertainty exist in any experiment, and they will be delineated in this section. Traditionally, it is assumed that a more refined, sophisticated experiment reveals better results. It will be shown, that in the case of this study, the simpler, less sophisticated SDMA experiment produced more reliable and repeatable results than the more complex TDMA experiment. Exactly the reasons for this apparent paradox are not known, but certainly a much smaller working sample for the TDMA experiment would be a logical reason. The compliment to this deficit in particle counts is the sensitivity of the PASm. As further proof, the more sophisticated approach taken by Shiraiwa *et al.*[77] reveals uncertainties in the 25% range while the uncertainties in the SDMA presented within are in the few percent range. As with any measurement, more sample availability and more sensitive equipment will almost always improve any given results. This study shows that sometimes less is more.

The first source of uncertainty derives from a fundamental issue in this experiment; a mobility measurement ***does not*** equal a mass measurement. Because absorption is directly related to mass, it is imperative to convert the DMA measured mobility diameters to a mass based measurement. As detailed earlier, the power law exponent and the volume pre-factor were derived empirically in order to determine a mass based diameter and are in good agreement with the values from Park *et al.*[99] Moreover, the mere assumption that the density of the soot generated is accurately known is also only that, an assumption. However, the uncertainty is reduced through the empirical derivation of the power law exponent and the volume pre-factor using the RDG theory. The aerosol measurements in this study consist of the absorption cross-section, the mobility diameter, the number concentration, and the electrical current of the aerosol. Estimates of the uncertainty in each of these quantities are given below. There is a 1.0% uncertainty in the absorption coefficient (u_c) arising from the difference between the calculated and measured cell constant for the O_2 *A*-band calibration measurement. [11] The random component of the uncertainty (u_r) is 0.7% for an absorption coefficient of $2.7 \times 10^{-6} cm^{-1}$.

The DMAs used in both studies were calibrated using NIST SRM 1964 (60 nm Polystyrene Latex Spheres), which has an uncertainty of 0.5%. [72] The observed peak particle size for the 60 nm spheres in suspension aerosolized with an electrospray was within 1.0% of the certified diameter. No correction was made for this small deviation. An additional 2.0% uncertainty is included to account for day-to-day variability in the sheath flow meter together with the varying atmospheric pressure. The combined mobility diameter uncertainty ($u_{comb}\, d_m$) is computed as the root-sum-of-squares (RSS) of the three components listed above and has a value of 2.3%.

The reported uncertainty for the CPC is 10% up to and including 10^5 particles per cm^3. For the TSI 3068A electrometer, the uncertainty in the current is not specified by the manufacture. The electrometer was calibrated relative to the CPC by generating singly charged, 15 nm sucrose particles by electrospraying a 0.16% by volume sucrose solution. The sucrose passed through a neutralizer and DMA before being directed to the CPC and electrometer. Because of the small particle size, the doubly charged fraction was negligible with an estimated fraction 600 times smaller than for the singly charged particles. Comparison measurements for the two instruments were made at concentrations of approximately 7x10^4, 2.5x10^4, and 8x10^3 particles per cm^3. In each case the CPC measurement was coincidence corrected. After converting the electrometer reading to a particle concentration, the average ratio of the electrometer number concentration reading to the CPC number concentration was 1.07± 3% uncertainty.

The quantities of greatest interest in regard to light absorption are the absorption amplification, the absorption cross-section, and the average d_{mass}. The uncertainties in these quantities were determined by propagating the uncertainties in the measured quantities described above. The C_{abs} (cm^2/particle) is expressed as:

$$C_{abs} = \frac{K_{abs}}{N_{CPC}} \tag{5.9}$$

where K_{abs} is the absorption coefficient (cm^{-1}) and the N_{cpc} (particles/cm^3) is the number concentration from the CPC. The K_{abs} and N_{cpc} are obtained every second and then the ratio of the one minute averages is computed to determine the C_{abs}. It was found from multiple experiments extending for several hours that the N_{cpc} and K_{abs} may drift by as much as 20%; however, the variation in the C_{abs} is much less with a nominal standard deviation of 3%. Measurements on five separate days over a one-month time span for the 100 nm mobility size had a larger variability with a day to day standard deviation of 9 %. The cause of this larger variation is not known. One possibility is a slight variation in the size distribution/morphology in the soot being produced. The estimated random component of the uncertainty in the C_{abs} was computed as the RSS of the within-day standard deviation and the day-to-day standard deviation and has a value of 6% and is used as our measure of the random component of the uncertainty in the absorption cross-section. This value is used for the error bars in Fig. 5.9 for C_{abs} for both the coated and uncoated spheres. Additionally, the uncertainty component of the CPC is 10%. Computing the RSS of the random component and the number concentration uncertainty reveals a combined uncertainty in the C_{abs} equal to 11.7%.

The absorption amplification is the ratio of the C_{abs} for the coated versus uncoated particle:

$$absorption\ amplification = \left. \frac{K_{abs}(coated)}{N(coated)} \middle/ \frac{K_{abs}(uncoated)}{N(uncoated)} \right. \tag{5.10}$$

The SDMA experiment was designed to switch from measuring the coated to uncoated particles in a few seconds by switching two valves. It was found that the number concentration varied from 1% to 4% for the coated versus uncoated particles. Therefore, the uncertainty in the absorption amplification is primarily due to the uncertainty in the ratio of the K_{abs} values. For these measurements the absorption coefficient is 2.7×10^{-6} cm^{-1} or greater corresponding to a random uncertainty of 0.7%. The cell constant uncertainty does not contribute to the total uncertainty because the ratio of the absorption coefficients was computed. The total uncertainty for the absorption amplification is computed as the RSS of the random uncertainties in the absorption coefficient of the coated and uncoated particles (both 0.7 %) and the result is a value of 1% for any single measurement. Variability from measurement to measurement with respect to the expected trends is likely due to sample differences in each measurement, rather than uncertainty in the measurement itself. The low level of uncertainty shown is further proof of the quality of the absorption amplification measurement in this study.

Another source of uncertainty is in revealing the fraction of singly and multiply charged particles. An empirical approach was taken in order to deconvolve the particle distributions into the singly and doubly charged particles. The procedure is outlined earlier in the paper, but the impact will be detailed in this section. It is well known that in DMA measurements particles of different sizes will appear as one size if the charges are different on said particles. For example, a 100 nm mobility diameter particle that is singly charged has doubly charged, 150 nm and triply charged, 200 nm particles appearing as the same mobility diameter. While the percentage of these larger particles is small with respect to the total particle count, their impact is felt when making an absorption measurement. The mass of the larger mobility particles can be 3 to 6 times (for the 150 and 200 nm particles respectively) larger than that of the 100 nm particles. These more massive particles can contribute significantly to the absorption coefficient measured by the PASm. If the particles contributing to the absorption are assumed to be all the same, the signal will be grossly misinterpreted and over predicted. A first order method for assessing the percentage of larger particles in each core size distribution is detailed earlier, but the important point to note is that experimentally, only the single and doubly charged particles can be determined. The triply charged are assumed to be somewhat negligible but not nonexistent and rolled into the uncertainty of the measurements. The assignment of singly and doubly charged particles to each core size ultimately determines what average mass based diameter is assumed to be in the PASm during any absorption measurement. Adjusting the representative particle size appears to be the simpler and reasonable approach rather than adjusting the absorption measurement to fit a predetermined mobility diameter. Once again, the major impact of this assumption is felt in the accuracy of the MACs reported; however, there is some impact in the amplification as well. While the impact is more obvious in the calculation of the MACs, in terms of the amplification, the difference between the coated particle and the core particle is affected.

The fractions of singly and doubly charged particles were needed for computing the uncertainty in the mass of the soot agglomerates and the average d_{mass}. The fraction of singly and doubly charged particles given in Table 1 is computed using the following expressions;

$$\left[{}^{N_{AE}}/_{C_1}\right] - N_{CPC} = N_2 \tag{5.11}$$

$$N_1 = N_{CPC} - N_2 \tag{5.12}$$

where N_1 and N_2 are the concentrations of singly and doubly charged particles and C_1=1.07 is the calibration factor measured with the CPC as discussed above. The effect of the uncertainty $u(C_1)$, which is equal to 3%, on N_1 and N_2 are computed by propagating the uncertainty in C_1 with the resulting expression:

$$u(N_1) = u(N_2) = \frac{(N_2+N_{CPC})}{C_1}u(C_1) \tag{5.13}$$

A 3% increase in C_1 is results in an increase of about 0.04 for the fraction of singly charged particles and a decrease of about 0.04 for the fraction of doubly charged particles for all three particle sizes.

Another source of uncertainty is the possibility of triply charged particles. Because of the rapid decrease in the size distribution above 200 nm, the 100 nm mobility diameter particles are the most likely to be impacted by triply charged particles. To estimate their impact, we assume that 10% of the particles are triply charged and adjust the fractions accordingly. Below, the effect of the triply charged particles on the average d_{mass} was estimated.

The sources of uncertainty for the $Mass_{dm}$ derived from Eq. 5.1, the particle density and the charging fraction are described above. These uncertainties are propagated to the total uncertainty in the mass. For the two larger core sizes, the mass uncertainty is about ± 7%. For the nominal 100 nm particle size the uncertainty is about +20% as a result of the large contribution from the presence of triply charged particles. The triply charge fraction only affects the plus uncertainty bound. The minus bounds are the same as the other two particle sizes. The uncertainty limits for MACs in Fig. 5.8 is estimated as the RSS of 6% for the day-to-day standard deviation for the cross-sectional measurement together with the 7% uncertainty in the mass and is equal to 9.2%.

The d_{mass} is computed from the average mass per particle using Eq. 5.1. As expected from the 1/3 exponent in Eq. 5.3, the uncertainty in average d_{mass} given in Table 5.2 is about 1/3 the uncertainty in the mass and ranges from 6% for the smallest particle size and 2% for the two largest.

In order to relate coating thickness to amplification, the size of the particles is required. As explained before, the core particle size has been converted to an average mass diameter, but the coated particles are not converted into a mass based measurement. The impetus for not converting the coated particles into mass based diameter is that the coated particles are assumed to be spherical. A spherical particle has the same diameter when measured by a DMA as with any other method. In other words, the ultimate goal of the mass based conversion of the core particles is to convert an aggregate into an equivalent mass sphere. Once the core particle is converted to a spherically equivalent diameter, it can then be compared to the spherically assumed coated particles. The basis for the assumption that coated particles are spherical is the Friedlander[100] work previously described in this paper. This assumption has its major impact on the determination of the coating thickness assumed in each measurement. The uncertainty in the reduced droplet size, $D_r(D_{coat})$ is defined by Eq. 5.8. The major source of uncertainty is in the value of average d_{mass} of the core particle. It is found from propagating the uncertainties in average d_{mass} and d_m for the droplet, that for absorption amplifications greater than 0.5, the uncertainty in D_r(drop) is about 5%.

While the experimental uncertainty is shown in all the plots where applicable, the total experimental uncertainty is not necessarily reflected in the error bars. The total experimental uncertainty is described in Table 5.3 below. Included in this total uncertainty are the uncertainties that could be considered systematic and not necessarily reflected in the day-to-day repeatability. An example of this systematic uncertainty would be an offset in the CPC. While this offset would be constant, therefore, not seen from day to day, it would ultimately affect the relationship between the experimentally determined values to the true values.

Table 5.3: Total experimental uncertainty percentages

Quantity	C_{abs} Amplification	C_{abs} (cm^2/particle)	$Mass_{dm}$ (g)	d_{mass} (nm)	MACs (m^2/g)	D_r *(coat)* (nm)
Random		± 6.0			±6.0	
Total	± 1.0	± 11.7	(+20.0-6.0)[a] ±6	(+6.0-2.0)[a] ±2.0	(+22.0-9.2)[a] ±9.2	(-22.0-4.0)[a] −4.0

[a] Effect of triple charges on smallest core particle size for SDMA. The 2nd set of uncertainties are for the larger two core sizes.

While most researchers tend to not detail the sources of uncertainty in their work, it was felt that due to the importance of this work, detailing the points where improvements can be made is critical. All of the issues presented in this section can be dealt with experimentally. And future work in this area will explore reducing these uncertainties. This experiment was designed to assess the impact of a non-absorbing coating on an absorbing core and that portion of the experiment is robust and rigorous and the uncertainties have been minimized to ± 1%.

5.4 Conclusions

In this study soot from a flame were generated in a well-controlled manner, and size selected particles were coated with DBP in order to study the effect of a non-absorbing coating on an absorbing particle. The data reveal that for soot, coating with a non-absorbing material does lead to an overall increase in the effective C_{abs}. Absorption amplifications at 405 nm, ranging from few percent to nearly 90% were observed with relative coating thicknesses of a few percent to over 300% for soot core sizes of 100, 150 and 200 nm mobility sizes. The range of the amplification of the C_{abs} due to the non-absorbing coating correlates with the theoretically predicted amplification as the core particle size increases, implying that as the larger aggregates are coated, they behave more like spheres. While there are several other studies that have tackled this problem[32, 33, 35, 36, 61, 77] those studies either use indirect measurements of the absorption or use surrogates for soot and atmospherically relevant coatings or still a different range of particle coating thicknesses. With respect to those studies, this study demonstrates similar levels of observed absorption amplifications with directly measured absorptions, and high levels of precision using soot. By using a custom-designed, first principle PASm together with sequential measurements of coated and uncoated particles, accurate absorption amplification measurements were made with an uncertainty of %. , which for similar experiments found in the literature are on the other of 25%.[77] In the case of the Shiraiwa *et al.*, the larger uncertainty is a result of the uncertainty in the measurement of the absorption cross-section of the coated and uncoated particle.

The results are consistent with a core-shell Mie theory calculation of the absorption enhancement with a uniformly increasing enhancement with increasing relative coating thickness. For all three SDMA core particle sizes (70 nm, 94 nm, and 108 nm), the maximum observed amplification was 1.7 to 1.8. For coating thicknesses in the range of 1 nm to 20 nm, enhancements in the range of 1.02 to 1.28 were observed

Under microscopic examination, we observe definite particle restructuring due to the coating material. As to whether restructuring occurs due to coating or its removal we were unable to ascertain. Finally, a MACs for each soot core size was calculated. The MACs for the SDMA and TDMA experiments is 10.8 ± 0.4 m^2/g. These results are slightly less than the calculated theoretical MACs of 12.4 ± 0.3m^2/g, but they are well within the bounds of the MACs found in various studies. [96, 98] The results from this experiment further confirm that a non-absorbing coating on an absorbing soot core does indeed effectively increase the absorption cross-section.

5.5 Figures

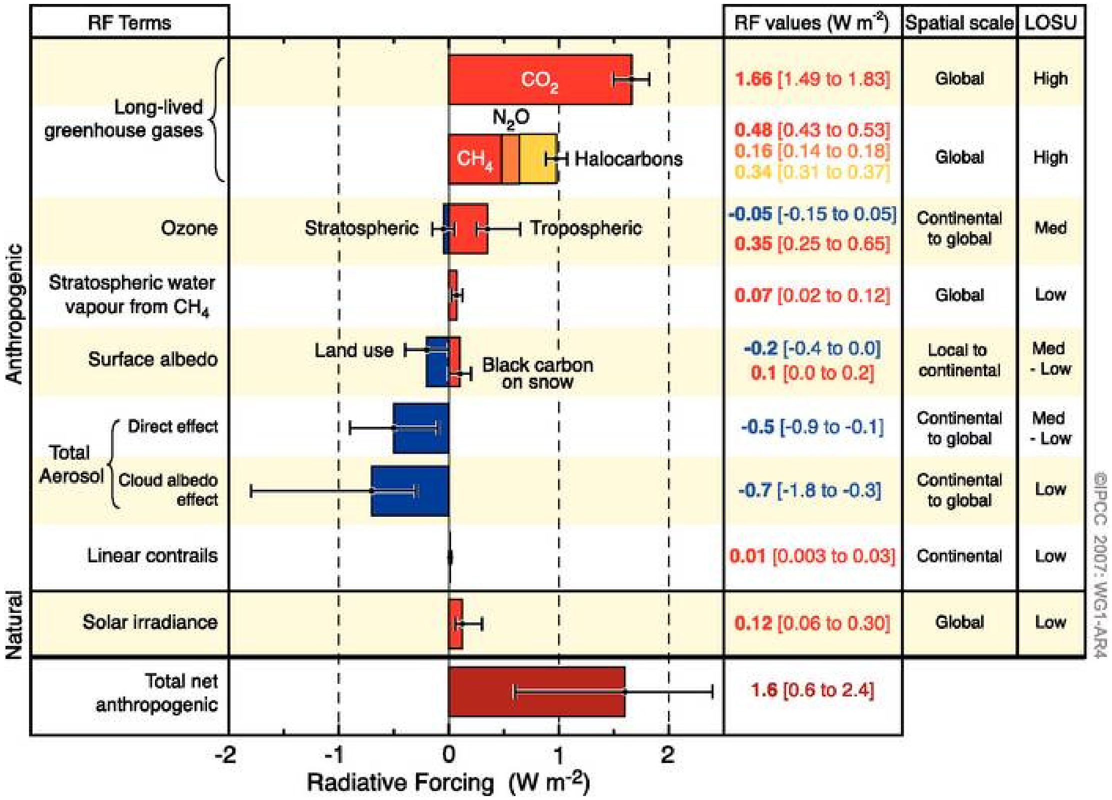

Figure 5.1: Comparison of climate forcing from IPCC for several greenhouse components. Note that absorbing aerosols are lost within the total aerosol and the nearly 100 % uncertainty on the aerosol bar.

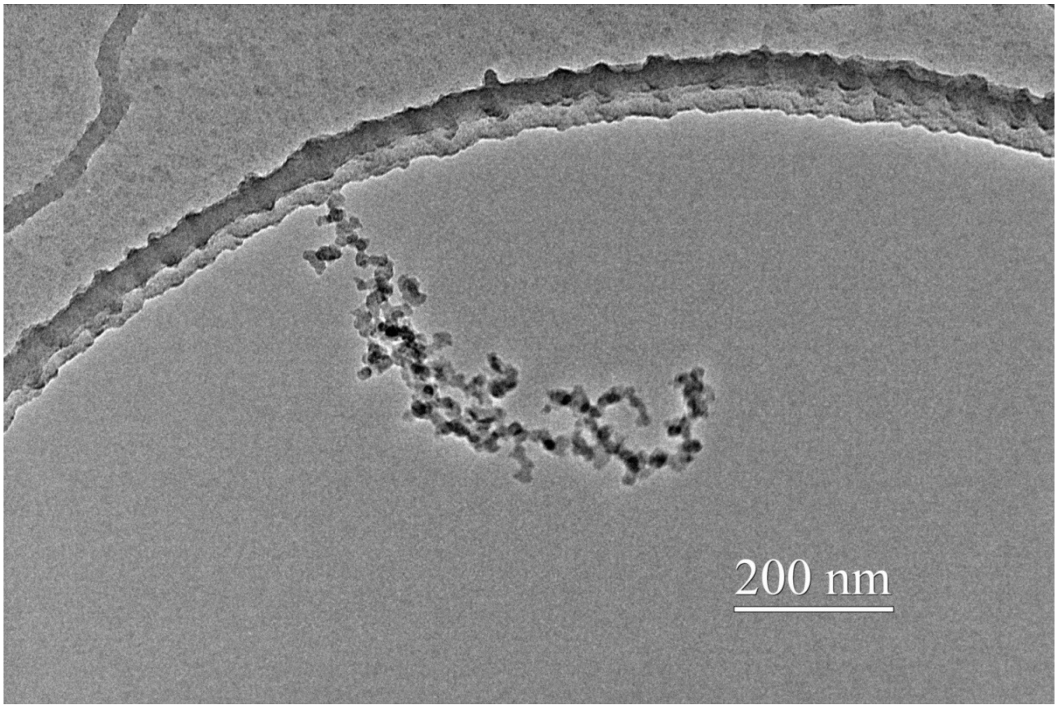

Figure 5.2: Transmission electron micrograph of a soot agglomerate denoting fractal structure of soot.

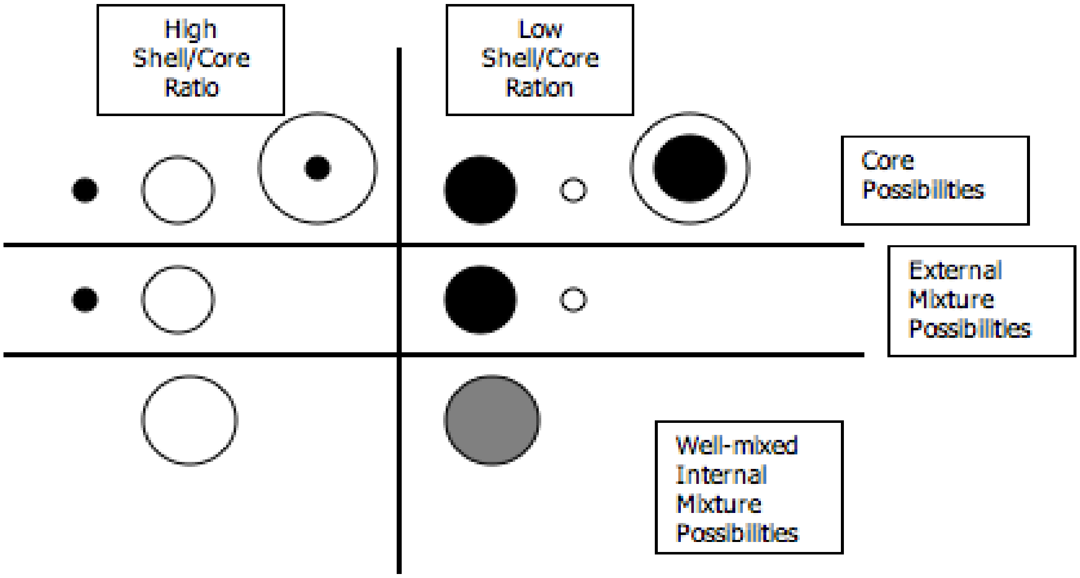

Figure 5.3: Possible mixing states of absorbing aerosols in the atmosphere as proposed by Jacobson[79].

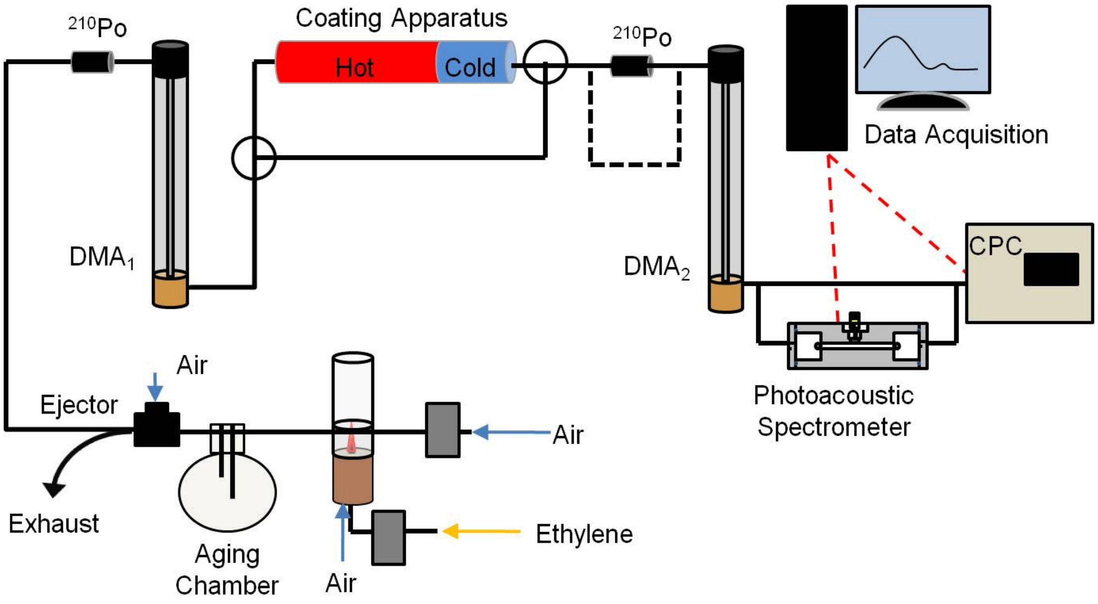

Figure 5.4: The SDAM and TDMA experimental set up as used in this study. Soot can follow two different paths after size selection with DMA$_1$. Soot can pass through a second aerosol neutralizer for uncoated measurements or can pass through the coating apparatus and then DMA$_2$ for PAS analysis. Both paths ultimately arrive at a CPC for counting. The SDMA experimental set up is the same with the exception of the second neutralizer and second DMA.

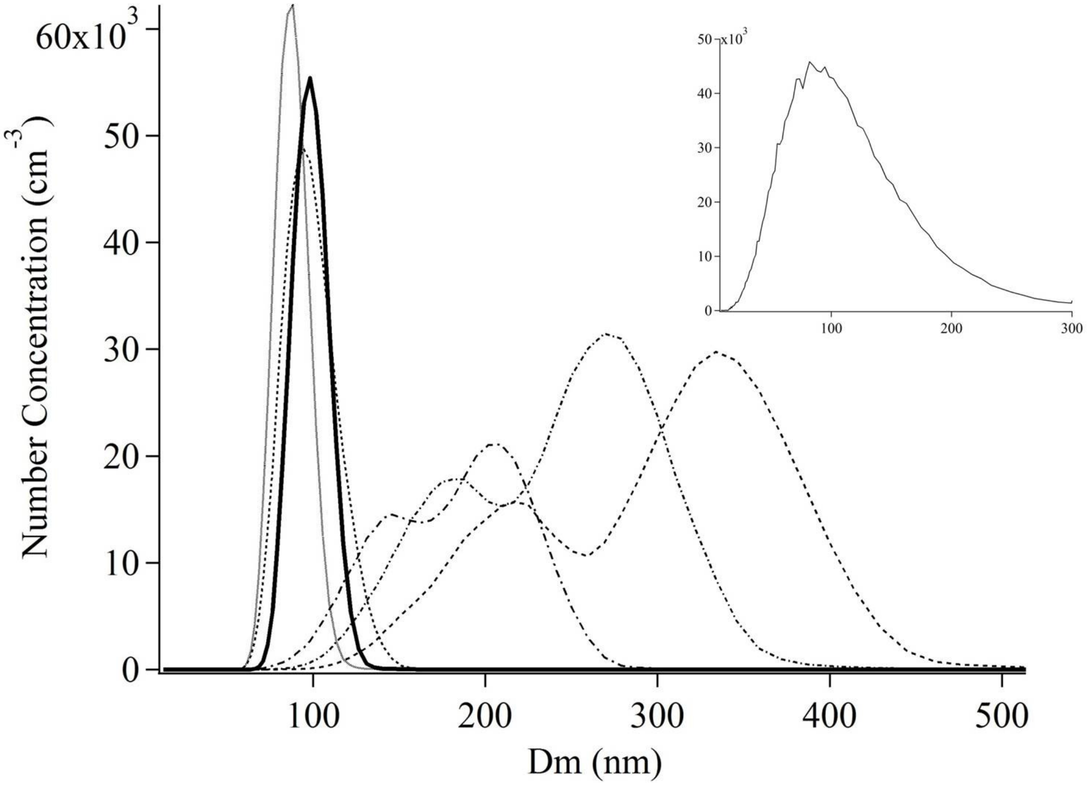

Figure 5.5: Particle distributions for 100 nm uncoated soot (solid thick line) and multiple representative coated soot distributions (dashed lines) during the SDMA mode. Each set of dashed lines is a different coating thickness for the same core size. Inset shows the full flame distribution measured using a single DMA.

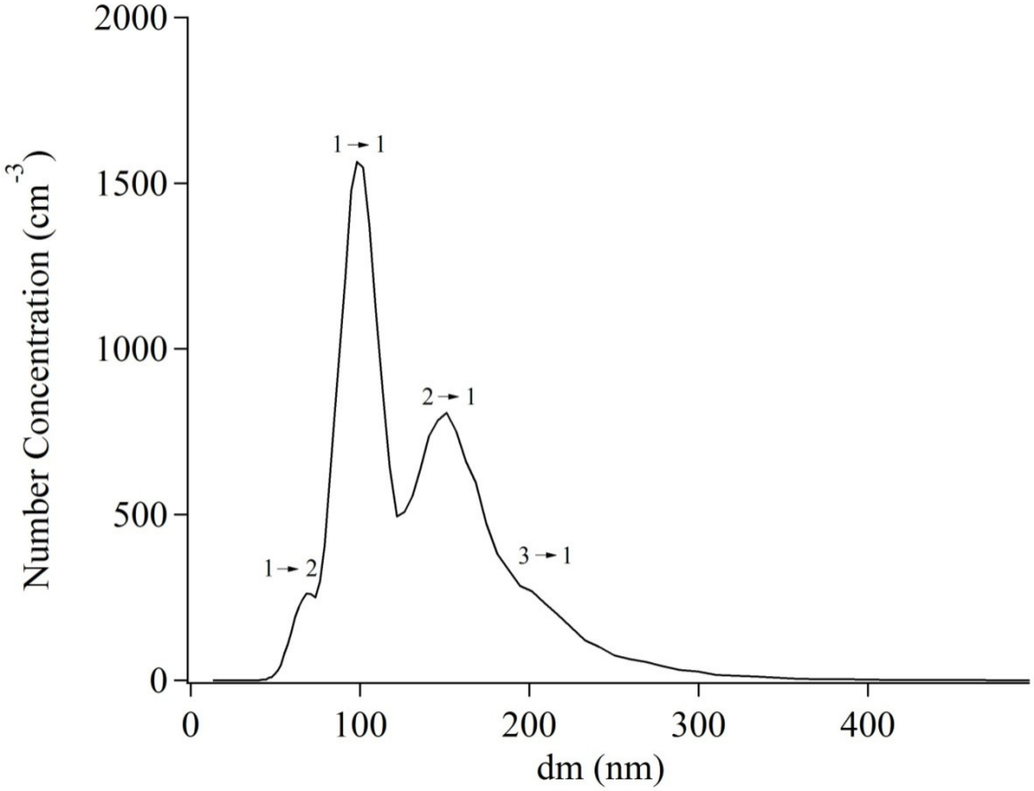

Figure 5.6A: 100 nm size selected soot that was run through a TDMA system with two neutralizers. The notation 2 → 1 indicates an initially doubly charged particle (2) is now a singly charged particle (1).

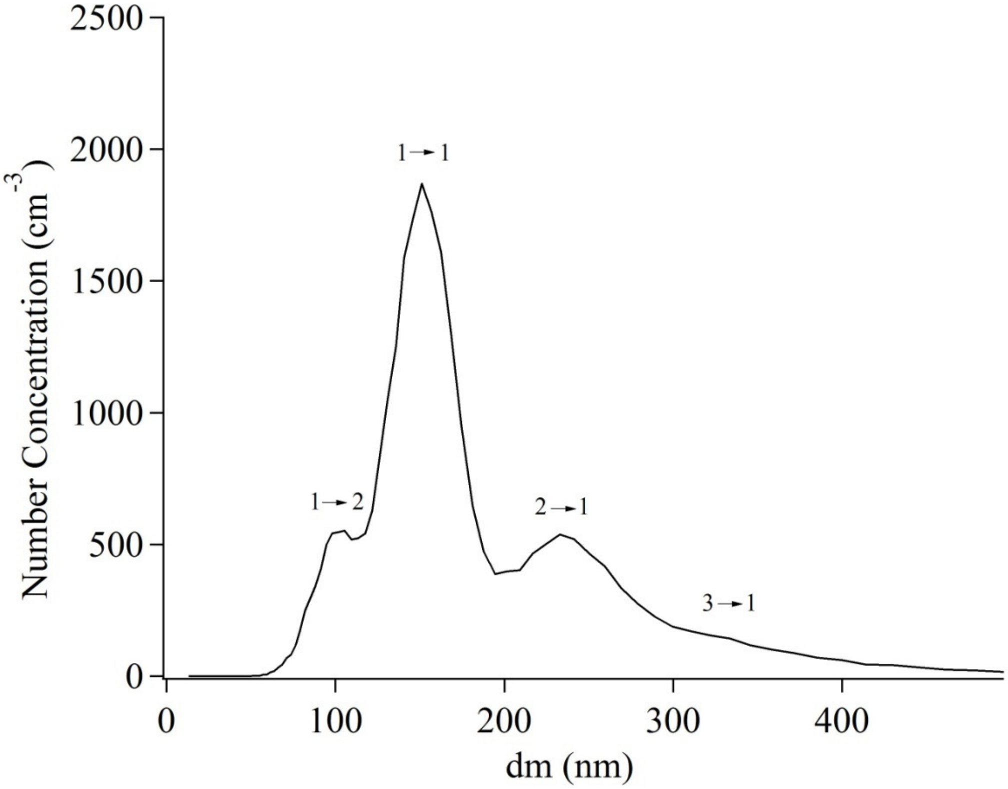

Figure 5.6B: 150 nm size selected soot that was run through a TDMA system with two aerosol chargers in place.

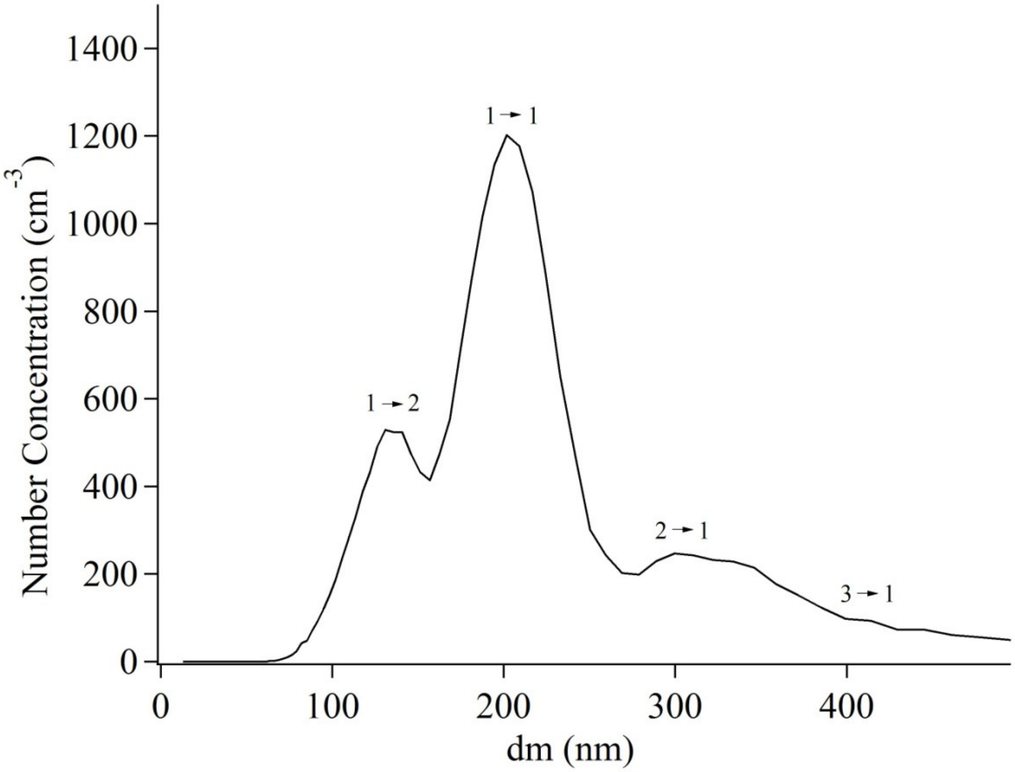

Figure 5.6C: 200 nm size selected soot that was run through a TDMA system with two aerosol chargers in place.

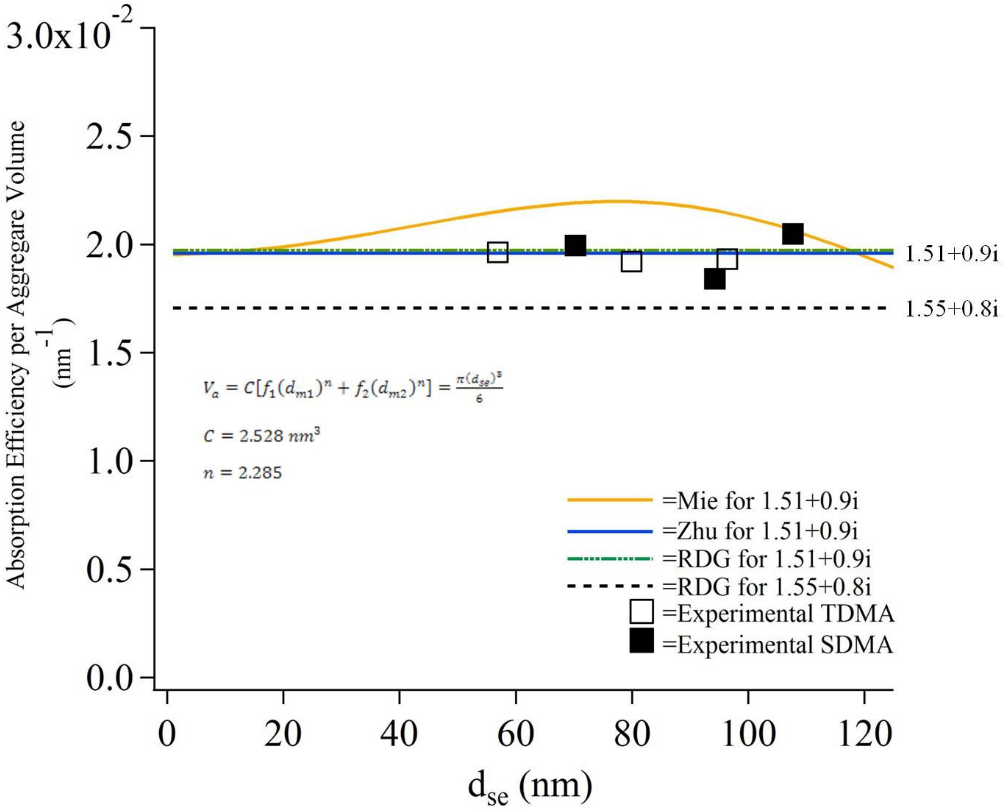

Figure 5.7: Fit for Mie and RDG theory at 1.51 + 0.9i (and also 1.55 + 0.8i for RDG) as well as the experimental SDMA and TDMA measurements for the absorption efficiency per aggregate volume with respect to the sphere equivalent diameters. The fit at 1.51 + 0.9i agrees with the experimental data measured.

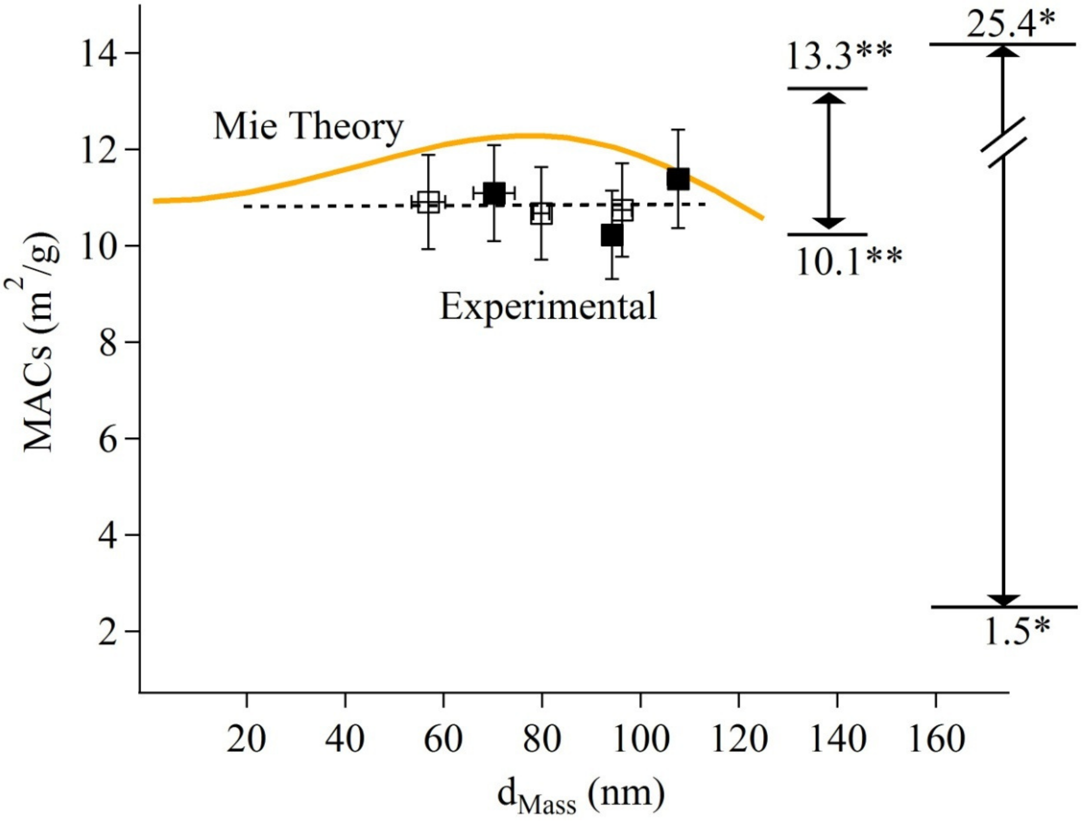

Figure 5.8: MACs for the experimentally measured data in contrast to the theoretical MACs (orange line) versus the average d_{mass}. Solid squares are SDMA and open squares are TDMA experimental data. The values denoted with the single* refer to the values in Bond and Bergstrom (2006) of 1.5 to 25.4 m^2/g and the value denoted with the double ** refer to the values in Choi et al. (1995) of 10.1 m^2/g, Slowik et al. (2007) of 13.3 m^2/g, Zhang et al. (2008) of 11.4 m^2/g and are specifically those of diffusion flame soot and have been adjusted to match the wavelength used in this experiment (405 nm).

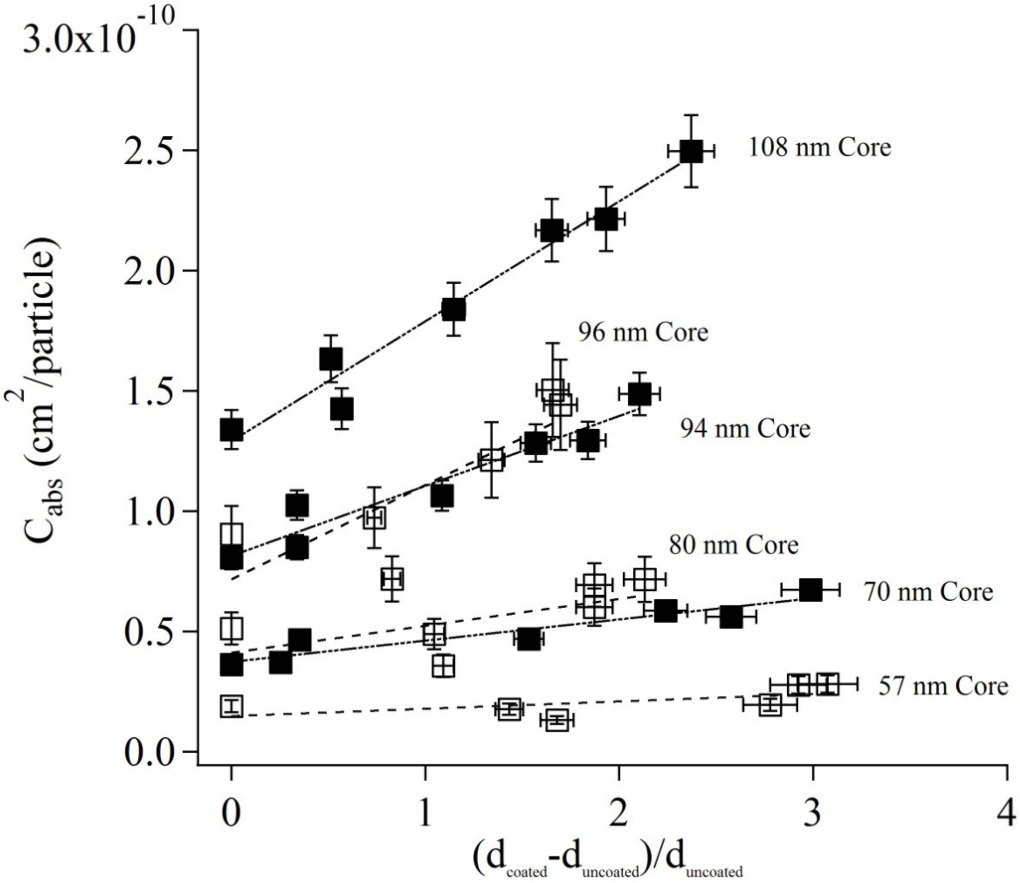

Figure 5.9: *C_{abs}* with respect to the coating thickness amplification for both the SDMA (solid squares) and the TDMA (open squares).

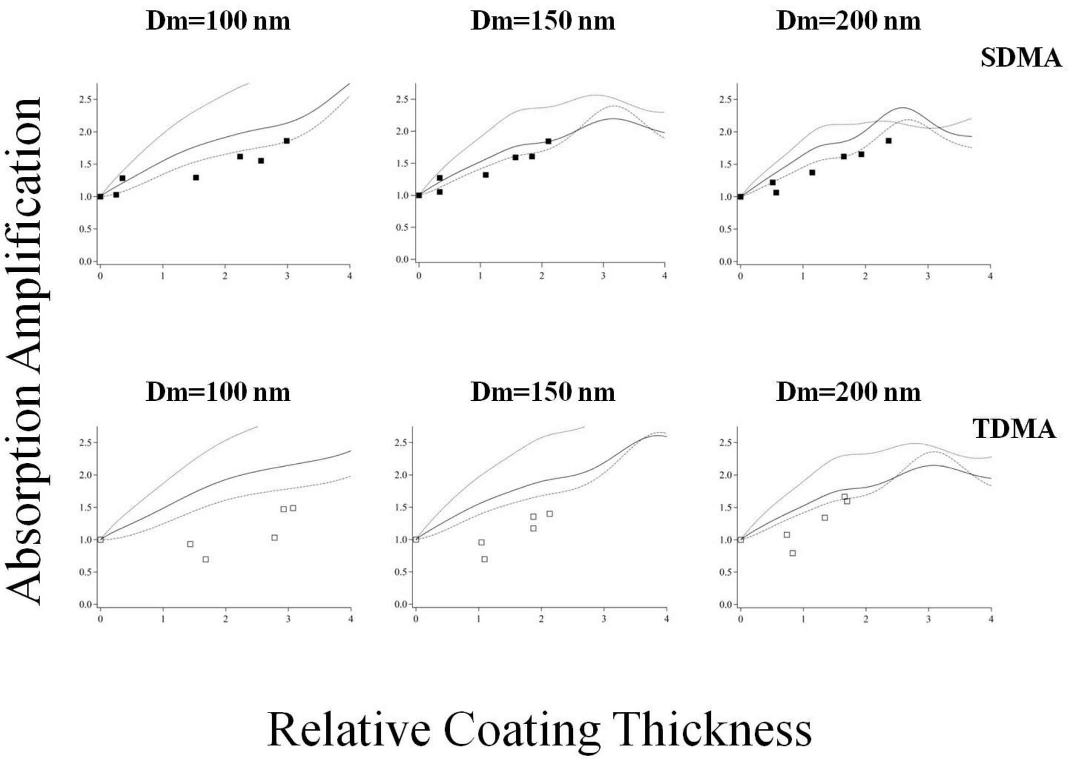

Figure 5.10: Modeled and experimental amplification of C_{abs} due to a non-absorbing coating with respect to the coating thickness amplification. The dashed lines are extremes in the indices of refraction (2.0+1.0i and 1.3+0.3i) and the solid line is the index of refraction assumed for this soot (1.51+0.9i). The solid squares are the SDMA data and the open squares are the TDMA data.

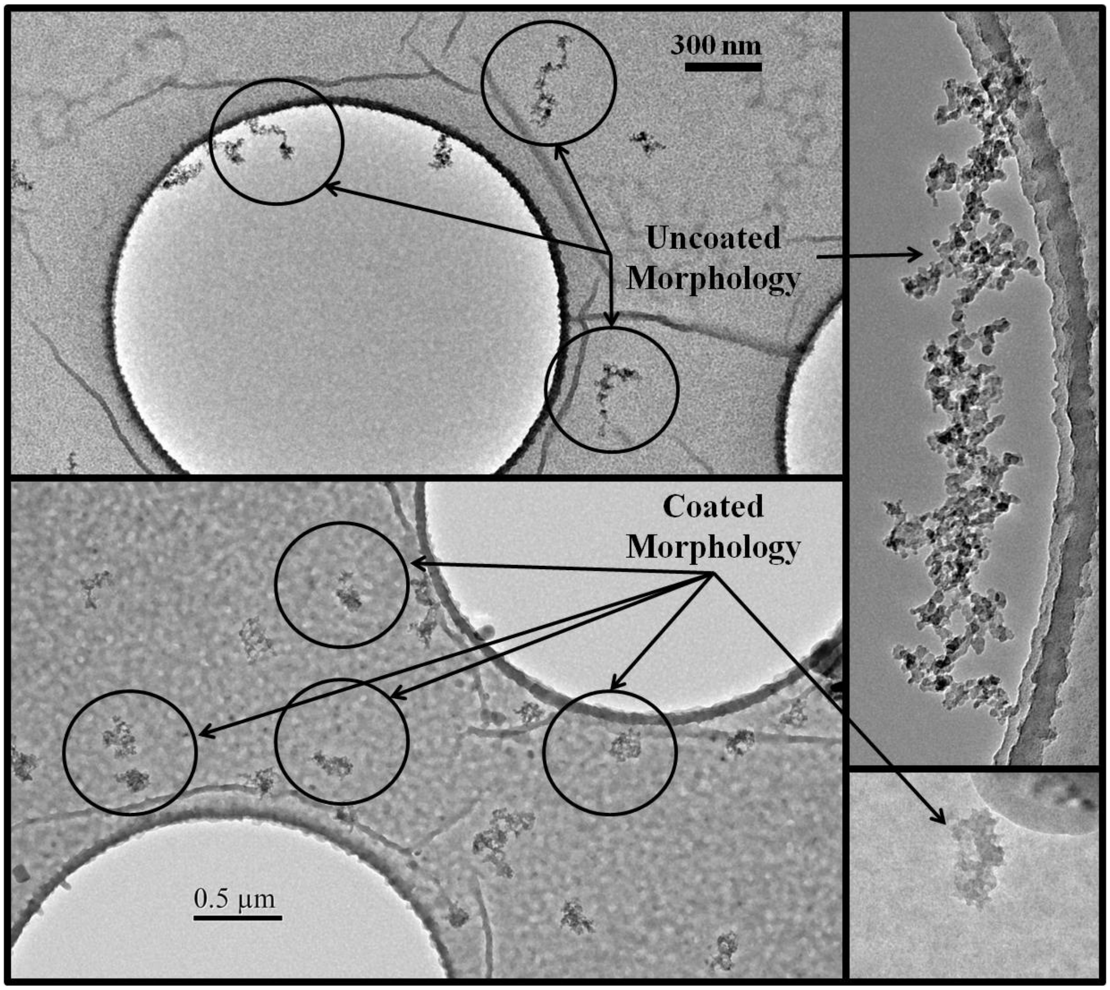

Figure 5.11: TEM micrographs of 150 nm mobility size uncoated soot (upper quadrants) and 150 nm mobility size soot coated with approximately 100 nm thick DBP shell (lower quadrants).

Chapter 6: Conclusions

6.1 Summary

The impetus for this work was a desire to contribute to the overall global climate change problem and lend experimental results to one segment of the climate change community. The issue of absorbing aerosols is one that has only recently been brought to the attention of the research community and much of the work started with field studies. While field studies are critical, experimental studies that control the majority of variables help pinpoint the source of the phenomena explored. This research provides one of many answers to a large and complex question.

The first major undertaking was to answer the initial question asked, will a non-absorbing coating on an absorbing particle effectively increase the absorption cross-section of said particle. The answer, yes, a transparent coating on a soot particle can double the absorption. Not only does a non-absorbing coating on an absorbing core effectively increase the absorption cross-section, but the results are on par with other similar studies. Within the bounds of the work, a doubling of the absorption cross-section was found and the soot agglomerate was found to be optically thin. The total mass of the soot contributes to the absorption properties of the particle. This is critical to the climate change community because Mie theory predicts that the total mass *will not* contribute to the absorption. Models can now incorporate a total mass absorption component in order to properly assess the impact soot has in the atmosphere. Not only was this result realized, but the uncertainty in the measurement was extremely small, on the order of 1%.

Subsequently, the custom built, first principles PASm was put to the test as a greenhouse gas sensor. The absorption cross-section of CO_2 was measured and found to be within 3% of the predicted line profile. Photoacoustic spectroscopy is a fast, inexpensive and precise measurement tool. This was shown with the CO_2 and the subsequently shown to be extremely sensitive when it was shown to be able to measure sub-monolayer coating thickness on soot aerosol.

In conclusion, the road has been long and hard, but the pay off has been well worth it. *Veni, vidi vici fumus*.

<u>*6.2 Future Work*</u>

Several suggestions for future work will be presented herein. Most obvious is the need for a mass measurement for the particle generated. Absorption is a property of mass, ergo, a mass measurement would seem appropriate. This would be possible by employing a DMA-aerosol particle mass analyzer system. While this was not possible for the work presented, it would be a relatively simple implementation into the existing system in the near future.

Further expansion of the photoacoustic spectrometer with multiple wavelengths would expand the breadth of the measurements. The measurements presented herein were limited by single wavelength measurements (with the exception of the CO_2 which was performed with an appropriate λ laser). A multiple wavelength PASm would benefit the climate change community as many commercial instruments that are widely employed typically measure at short, medium and longer visible wavelengths. Our system was tuned to provide a unique window not commonly explored in the climate change community for soot.

Appendix

Included in this appendix is the raw soot data which was used in both sets of soot experiments (Chapters 4 and 5).

	d_m Core (nm)	**C_{abs} (cm^2/particle)**	**C_{abs} (cm^2/particle)**	**C_{abs} (cm^2/particle)**	**C_{abs} (cm^2/particle)**	**C_{abs} (cm^2/particle)**	**C_{abs} (cm^2/particle)**	**C_{abs} (cm^2/particle)**
TDMA Data Core	98.2	2.04768E-11	2.19087E-11	1.55263E-11	1.51266E-11	2.13933E-11	2.0174E-11	1.78727E-11
	151.2	5.00396E-11	5.86713E-11	4.04863E-11	n/a	5.43344E-11	5.29406E-11	5.07113E-11
	201.7	8.97171E-11	1.06309E-10	7.34698E-11	7.18141E-11	1.00834E-10	9.73565E-11	9.31937E-11

	d_m Core (nm)	**C_{abs} (cm^2/particle)**	**C_{abs} (cm^2/particle)**	**C_{abs} (cm^2/particle)**	**C_{abs} (cm^2/particle)**	**C_{abs} (cm^2/particle)**
SDMA Data Core	98.2	3.70E-11	4.10791E-11	3.48965E-11	3.53275E-11	3.27312E-11
	151.2	8.32E-11	8.58602E-11	7.91707E-11	8.00369E-11	7.4818E-11
	201.7	1.38E-10	1.31879E-10	1.36478E-10	1.36206E-10	1.26454E-10

	TDMA Coating Temp (C°)	**100 nm Core d_{RDG} Core + Coating (nm)**	**100 nm Core Coated Cross-Section (cm^2/particle)**	**150 nm Core d_{RDG} Core + Coating (nm)**	**150 nm Core Coated Cross-Section (cm^2/particle)**	**200 nm Core d_{RDG} Core + Coating (nm)**	**200 nm Core Coated Cross-Section (cm^2/particle)**
TDMA Experimental Data Coating Measurements Uses d_{RDG} as core size	RT	56.9	1.89255E-11	79.8	5.11972E-11	96.3	9.03849E-11
	32	157.5	1.76216E-11	163.4	4.8977E-11	167.3	9.73266E-11
	33	174.8	1.3152E-11	167.2	3.56836E-11	176.2	7.17631E-11
	34	251.9	1.95246E-11	229.3	6.0028E-11	225.5	1.21258E-10
	35	262.1	2.78462E-11	229.3	6.93206E-11	255.9	1.50451E-10
	36	272.7	2.81582E-11	250.1	7.16107E-11	259.7	1.44155E-10

	SDMA Coating Temp (C°)	**100 nm Core d_{RDG} Core + Coating (nm)**	**100 nm Core Coated Cross-Section (cm^2/particle)**	**150 nm Core d_{RDG} Core + Coating (nm)**	**150 nm Core Coated Cross-Section (cm^2/particle)**	**200 nm Core d_{RDG} Core + Coating (nm)**	**200 nm Core Coated Cross-Section (cm^2/particle)**
SDMA Results Experimental Data Coating Measurements Uses d_{RDG} as core size	RT	70.2	3.61981E-11	94.2	8.06215E-11	107.7	1.33899E-10
	19	88.0	3.72267E-11	126.0	8.49316E-11	169.0	1.42535E-10
	28	95.0	4.65004E-11	126.0	1.02558E-10	163.0	1.63362E-10
	30	177.9	4.68686E-11	196.5	1.0646E-10	231.1	1.83966E-10
	32	227.5	5.85951E-11	242.1	1.28359E-10	285.6	2.16822E-10
	33	251.1	5.62243E-11	267.4	1.29461E-10	315.7	2.21566E-10
	35	280.0	6.73947E-11	292.5	1.48678E-10	362.8	2.49557E-10

The data table below is the raw data acquired directly from the LabView data acquisition program written in order to collect the PAS signal as well as the CPC counts in order to calculate the particle absorption cross-section.

LIA "x" (V)	LIA "x0" (V)	LIA "y" (V)	LIA "y0" (V)	P-P Power (W)	LIA "R" (V)	Phase (Degrees)	Time Elapsed (s)	Counts Signal	Cal Con	Alpha	Alpha/part
-5.9192E-06	-1.422E-07	1.11655E-05	9.164E-07	0.211220138	1.17651E-05	117.9295282	31	80103.70082	20	2.78503E-06	3.47678E-11
-0.000005764	-1.422E-07	1.08787E-05	9.164E-07	0.21124426	0.000011439	117.9164449	94.3125	78154.34643	20	2.70753E-06	3.46434E-11
-5.6924E-06	-1.422E-07	1.07552E-05	9.164E-07	0.211222868	1.12963E-05	117.8911131	157.625	76695.42135	20	2.67402E-06	3.48655E-11
-5.6951E-06	-1.422E-07	1.07699E-05	9.164E-07	0.211198463	1.13104E-05	117.8697628	220.890625	77112.61428	20	2.67767E-06	3.47242E-11
-5.6539E-06	-1.422E-07	1.07034E-05	9.164E-07	0.211236399	1.12322E-05	117.8443978	284.171875	77245.83419	20	2.65868E-06	3.44184E-11
-5.5762E-06	-1.422E-07	1.05509E-05	9.164E-07	0.211240723	1.10613E-05	117.8567356	347.484375	76173.19485	20	2.61817E-06	3.43713E-11

References

1. Kosterev, A. A.; Tittel, F. K.; Serebryakov, D. V.; Malinovsky, A. L.; Morozov, I. V., Applications of quartz tuning forks in spectroscopic gas sensing. *Review of Scientific Instruments* **2005,** *76* (4).
2. Arnott, W. P., *Personal Communication* **2010**.
3. Arnott, W. P.; Moosmuller, H.; Rogers, C. F.; Jin, T. F.; Bruch, R., Photoacoustic spectrometer for measuring light absorption by aerosol: instrument description. *Atmospheric Environment* **1999,** *33* (17), 2845-2852.
4. Arnott, W. P.; Walker, J. W.; Moosmuller, H.; Elleman, R. A.; Jonsson, H. H.; Buzorius, G.; Conant, W. C.; Flagan, R. C.; Seinfeld, J. H., Photoacoustic insight for aerosol light absorption aloft from meteorological aircraft and comparison with particle soot absorption photometer measurements: DOE Southern Great Plains climate research facility and the coastal stratocumulus imposed perturbation experiments. *Journal of Geophysical Research-Atmospheres* **2006,** *111* (D5).
5. Trenberth, K. E.; Fasullo, J. T.; Kiehl, J., EARTH'S GLOBAL ENERGY BUDGET. *Bulletin of the American Meteorological Society* **2009,** *90* (3), 311-+.
6. Hansen, J.; Sato, M., Greenhouse gas growth rates. *Proceedings of the National Academy of Sciences of the United States of America* **2004,** *101* (46), 16109-16114.
7. Hansen, J.; Sato, M.; Ruedy, R.; Nazarenko, L.; Lacis, A.; Schmidt, G. A.; Russell, G.; Aleinov, I.; Bauer, M.; Bauer, S.; Bell, N.; Cairns, B.; Canuto, V.; Chandler, M.; Cheng, Y.; Del Genio, A.; Faluvegi, G.; Fleming, E.; Friend, A.; Hall, T.; Jackman, C.; Kelley, M.; Kiang, N.; Koch, D.; Lean, J.; Lerner, J.; Lo, K.; Menon, S.; Miller, R.; Minnis, P.; Novakov, T.; Oinas, V.; Perlwitz, J.; Rind, D.; Romanou, A.; Shindell, D.; Stone, P.; Sun, S.; Tausnev, N.; Thresher, D.; Wielicki, B.; Wong, T.; Yao, M.; Zhang, S., Efficacy of climate forcings. *Journal of Geophysical Research-Atmospheres* **2005,** *110* (D18).
8. Seinfeld, J. H.; Pandis, S. N., *Atmospheric Chemistry and Physics: From Air Pollution to Climate Change*. Wiley: New York, 1998.
9. Thomas, G. E.; Stamnes, K., *Radiative Transfer in the Atmosphere and Ocean*. Cambridge University Press: Cambridge, UK, 2002; p 517.
10. Novakov, T.; Ramanathan, V.; Hansen, J. E.; Kirchstetter, T. W.; Sato, M.; Sinton, J. E.; Sathaye, J. A., Large historical changes of fossil-fuel black carbon aerosols. *Geophysical Research Letters* **2003,** *30* (6).
11. Gillis, K. A.; Havey, D. K.; Hodges, J. T., Standard Photoacoustic Spectrometer: Model and Validation Using O2 A-band Spectra. *Review of Scientific Instruments* **2010,** *In Press*.
12. Allan, D. W., Statistics of Atomic Frequency Standards. *Proceedings of the Institute of Electrical and Electronics Engineers* **1966,** *54* (2), 221-&.
13. Toth, R. A.; Brown, L. R.; Miller, C. E.; Devi, V. M.; Benner, D. C., Spectroscopic database of CO2 line parameters: 4300-7000 cm(-1). *Journal of Quantitative Spectroscopy & Radiative Transfer* **2008,** *109* (6), 906-921.

14. Gebhart, J., Optical Direct-Reading Techniques: Light Intensity Systems. In *Aerosol Measurements: Principles, Techniques, and Applications*, Baron, P. A.; Willeke, K., Eds. Wiley-InterScience, Inc.: 2001.

15. Bohren, C. F.; Huffman, D. R., *Absorption and Scattering of Light by Small Particles*. Wiley-VCH: Weinheim, 2004.

16. Hansen, J.; Sato, M.; Ruedy, R.; Kharecha, P.; Lacis, A.; Miller, R.; Nazarenko, L.; Lo, K.; Schmidt, G. A.; Russell, G.; Aleinov, I.; Bauer, S.; Baum, E.; Cairns, B.; Canuto, V.; Chandler, M.; Cheng, Y.; Cohen, A.; Del Genio, A.; Faluvegi, G.; Fleming, E.; Friend, A.; Hall, T.; Jackman, C.; Jonas, J.; Kelley, M.; Kiang, N. Y.; Koch, D.; Labow, G.; Lerner, J.; Menon, S.; Novakov, T.; Oinas, V.; Perlwitz, J.; Rind, D.; Romanou, A.; Schmunk, R.; Shindell, D.; Stone, P.; Sun, S.; Streets, D.; Tausnev, N.; Thresher, D.; Unger, N.; Yao, M.; Zhang, S., Climate simulations for 1880-2003 with GISS modelE. *Climate Dynamics* **2007,** *29* (7-8), 661-696.

17. Chylek, P.; Videen, G.; Ngo, D.; Pinnick, R. G.; Klett, J. D., EFFECT OF BLACK CARBON ON THE OPTICAL-PROPERTIES AND CLIMATE FORCING OF SULFATE AEROSOLS. *Journal of Geophysical Research-Atmospheres* **1995,** *100* (D8), 16325-16332.

18. Satheesh, S. K.; Moorthy, K. K., Radiative effects of natural aerosols: A review. *Atmospheric Environment* **2005,** *39* (11), 2089-2110.

19. Bates, T. S.; Anderson, T. L.; Baynard, T.; Bond, T.; Boucher, O.; Carmichael, G.; Clarke, A.; Erlick, C.; Guo, H.; Horowitz, L.; Howell, S.; Kulkarni, S.; Maring, H.; McComiskey, A.; Middlebrook, A.; Noone, K.; O'Dowd, C. D.; Ogren, J.; Penner, J.; Quinn, P. K.; Ravishankara, A. R.; Savoie, D. L.; Schwartz, S. E.; Shinozuka, Y.; Tang, Y.; Weber, R. J.; Wu, Y., Aerosol direct radiative effects over the northwest Atlantic, northwest Pacific, and North Indian Oceans: estimates based on in-situ chemical and optical measurements and chemical transport modeling. *Atmospheric Chemistry and Physics* **2006,** *6*, 1657-1732.

20. Bond, T. C.; Habib, G.; Bergstrom, R. W., Limitations in the enhancement of visible light absorption due to mixing state. *Journal of Geophysical Research-Atmospheres* **2006,** *111* (D20).

21. Highwood, E. J.; Kinnersley, R. P., When smoke gets in our eyes: The multiple impacts of atmospheric black carbon on climate, air quality and health. *Environment International* **2006,** *32* (4), 560-566.

22. Bohren, C. F.; Huffman, D. R., *Absorption and Scattering of Light by Small Particles*. WILEY-VCH Verlag GmbH & Co. KGaA: Weinheim, 1983; p 530.

23. 2001, I., *Climate Change 2001: The Scientific Basis: Contributions of Working Group I to the Third Assessment Report of the Intergovernmental Panel on Climate Change*. Cambridge University Press: Cambridge, UK, 2001.

24. Haywood, J. M.; Ramaswamy, V., Global sensitivity studies of the direct radiative forcing due to anthropogenic sulfate and black carbon aerosols. *Journal of Geophysical Research-Atmospheres* **1998,** *103* (D6), 6043-6058; Haywood, J.; Boucher, O., Estimates of the direct and indirect radiative forcing due to tropospheric aerosols: A review. *Reviews of Geophysics* **2000,** *38* (4), 513-543; Cooke, W. F.; Liousse, C.; Cachier, H.; Feichter, J., Construction of a 1 degrees x 1 degrees fossil fuel emission data set for carbonaceous aerosol and implementation and radiative

impact in the ECHAM4 model. *Journal of Geophysical Research-Atmospheres* **1999,** *104* (D18), 22137-22162.

25. Jacobson, M. Z., A physically-based treatment of elemental carbon optics: Implications for global direct forcing of aerosols. *Geophysical Research Letters* **2000,** *27* (2), 217-220.

26. Cartwright, J.; Nagelschmidt, G.; Skidmore, J. W., The Study of Air Pollution with Electron Microscope *Quarterly Journal of the Royal Meteorological Society* **1956,** *82* (351), 82-86; Schneider, S. H., Atmospheric Particles and Climate: Can We Evaluate the Impact of Man's Activities *Institute of Environmental Sciences Proceedings* **1972,** *18*, 557-563.

27. Saathoff, H.; Mohler, O.; Schurath, U.; Kamm, S.; Dippel, B.; Mihelcic, D., The AIDA soot aerosol characterisation campaign 1999. *Journal of Aerosol Science* **2003,** *34* (10), 1277-1296; Schnaiter, M.; Horvath, H.; Mohler, O.; Naumann, K. H.; Saathoff, H.; Schock, O. W., UV-VIS-NIR spectral optical properties of soot and soot-containing aerosols. *Journal of Aerosol Science* **2003,** *34* (10), 1421-1444; Weingartner, E.; Saathoff, H.; Schnaiter, M.; Streit, N.; Bitnar, B.; Baltensperger, U., Absorption of light by soot particles: determination of the absorption coefficient by means of aethalometers. *Journal of Aerosol Science* **2003,** *34* (10), 1445-1463.

28. Cappa, C. D.; Lack, D. A.; Burkholder, J. B.; Ravishankara, A. R., Bias in filter-based aerosol light absorption measurements due to organic aerosol loading: Evidence from laboratory measurements. *Aerosol Science and Technology* **2008,** *42* (12), 1022-1032.

29. Chow, J. C.; Watson, J. G.; Doraiswamy, P.; Chen, L. W. A.; Sodeman, D. A.; Lowenthal, D. H.; Park, K.; Arnott, W. P.; Motallebi, N., Aerosol light absorption, black carbon, and elemental carbon at the Fresno Supersite, California. *Atmospheric Research* **2009,** *93* (4), 874-887.

30. Lack, D. A.; Quinn, P. K.; Massoli, P.; Bates, T. S.; Coffman, D.; Covert, D. S.; Sierau, B.; Tucker, S.; Baynard, T.; Lovejoy, E.; Murphy, D. M.; Ravishankara, A. R., Relative humidity dependence of light absorption by mineral dust after long-range atmospheric transport from the Sahara. *Geophysical Research Letters* **2009,** *36*.

31. Bond, T. C.; Anderson, T. L.; Campbell, D., Calibration and intercomparison of filter-based measurements of visible light absorption by aerosols. *Aerosol Science and Technology* **1999,** *30* (6), 582-600.

32. Gangl, M.; Kocifaj, M.; Videen, G.; Horvath, H., Light absorption by coated nano-sized carbonaceous particles. *Atmospheric Environment* **2008,** *42* (11), 2571-2581.

33. Khalizov, A. F.; Xue, H. X.; Wang, L.; Zheng, J.; Zhang, R. Y., Enhanced Light Absorption and Scattering by Carbon Soot Aerosol Internally Mixed with Sulfuric Acid. *Journal of Physical Chemistry A* **2009,** *113* (6), 1066-1074.

34. Schnaiter, M.; Linke, C.; Mohler, O.; Naumann, K. H.; Saathoff, H.; Wagner, R.; Schurath, U.; Wehner, B., Absorption amplification of black carbon internally mixed with secondary organic aerosol. *Journal of Geophysical Research-Atmospheres* **2005,** *110* (D19).

35. Slowik, J. G.; Cross, E. S.; Han, J. H.; Davidovits, P.; Onasch, T. B.; Jayne, J. T.; WilliamS, L. R.; Canagaratna, M. R.; Worsnop, D. R.; Chakrabarty, R. K.; Moosmuller, H.; Arnott, W. P.; Schwarz, J. P.; Gao, R. S.; Fahey, D. W.; Kok, G. L.;

Petzold, A., An inter-comparison of instruments measuring black carbon content of soot particles. *Aerosol Science and Technology* **2007,** *41* (3), 295-314.
36. Zhang, R. Y.; Khalizov, A. F.; Pagels, J.; Zhang, D.; Xue, H. X.; McMurry, P. H., Variability in morphology, hygroscopicity, and optical properties of soot aerosols during atmospheric processing. *Proceedings of the National Academy of Sciences of the United States of America* **2008,** *105* (30), 10291-10296.
37. Gustafsson, O.; Krusa, M.; Zencak, Z.; Sheesley, R. J.; Granat, L.; Engstrom, E.; Praveen, P. S.; Rao, P. S. P.; Leck, C.; Rodhe, H., Brown Clouds over South Asia: Biomass or Fossil Fuel Combustion? *Science* **2009,** *323* (5913), 495-498.
38. Dickerson, R. R.; Andreae, M. O.; Campos, T.; Mayol-Bracero, O. L.; Neusuess, C.; Streets, D. G., Analysis of black carbon and carbon monoxide observed over the Indian Ocean: Implications for emissions and photochemistry. *Journal of Geophysical Research-Atmospheres* **2002,** *107* (D19).
39. Santoro, R. J.; Semerjian, H. G.; Dobbins, R. A., Soot Particle Measurements in Diffusion Flames. *Combustion and Flame* **1983,** *51* (2), 203-218.
40. Liu, B. Y. H.; Lee, K. W., AEROSOL GENERATOR OF HIGH STABILITY. *American Industrial Hygiene Association Journal* **1975,** *36* (12), 861-865.
41. Fenn, J. B., ION FORMATION FROM CHARGED DROPLETS - ROLES OF GEOMETRY, ENERGY, AND TIME. *Journal of the American Society for Mass Spectrometry* **1993,** *4* (7), 524-535.
42. Dole, M.; Mack, L. L.; Hines, R. L., MOLECULAR BEAMS OF MACROIONS. *Journal of Chemical Physics* **1968,** *49* (5), 2240-&.
43. Knutson, E. O.; Whitby, K. T., Aerosol Classification by Electric Mobility: Apparatus, Theory and Applications. *Journal of Aerosol Science* **1975,** *6*, 9.
44. Knutson, E. O.; Whitby, K. T., Accurate Measurement of Aerosol Electric Mobility Moments. *Journal of Aerosol Science* **1975,** *6*, 8.
45. Hinds, W. C., *Aerosol Technology: Properties, Behavior, and Measurement of Airoborne Particles*. Second ed.; John Wiley & Sons, Inc.: New York, 1999; p 483.
46. McMurry, P. H., A review of atmospheric aerosol measurements. *Atmospheric Environment* **2000,** *34* (12-14), 1959-1999.
47. Brown, K. L.; Tautfest, G. W., Faraday-Cup Monitors for High Energy Electron Beams. *Review of Scientific Instruments* **1956,** *27* (9), 696-702.
48. Bell, A. G., On the Production and Reproduction of Sound by Light *American Journal of Science* **1880** *XX*, 305-324; Bell, A. G., Upon the Production of Sound by Radiant Energy *Philosophical Magazine Journal of Science* **1881,** *XI*, 510-528.
49. Adams, K. M., REAL-TIME INSITU MEASUREMENTS OF ATMOSPHERIC OPTICAL-ABSORPTION IN THE VISIBLE VIA PHOTOACOUSTIC-SPECTROSCOPY .1. EVALUATION OF PHOTOACOUSTIC CELLS. *Applied Optics* **1988,** *27* (19), 4052-4056; Harren, F. J. M.; Cotti, G.; Oomens, J.; Hekkert, S. t. L., Photoacoustic Spectroscopy in Trace Gas Monitoring. In *Encyclopedia of Analytical Chemistry*, Meyers, R. A., Ed. John Wiley & Sons Ltd: Chichester, 2000; pp 2203–2226.
50. Miklos, A.; Hess, P.; Bozoki, Z., Application of acoustic resonators in photoacoustic trace gas analysis and metrology. *Review of Scientific Instruments* **2001,** *72* (4), 1937-1955.

51. Chakrabarty, R. K.; Moosmuller, H.; Arnott, W. P.; Garro, M. A.; Slowik, J. G.; Cross, E. S.; Han, J. H.; Davidovits, P.; Onasch, T. B.; Worsnop, D. R., Light scattering and absorption by fractal-like carbonaceous chain aggregates: Comparison of theories and experiment. *Applied Optics* **2007,** *46* (28), 6990-7006.

52. Havey, D. K.; Bueno, P. A.; Gillis, K. A.; Hodges, J. T.; Mulholland, G. W.; van Zee, R. D.; Zachariah, M. R., Photoacoustic Spectrometer with a Calculable Cell Constant for Measurements of Gases and Aerosols. *Analytical Chemistry* **2010,** *82* (19), 7935-7942.

53. Murphy, D. M., The Effect of Water Evaporation on Photoacoustic Signals in Transition and Molecular Flow. *Aerosol Science and Technology* **2009,** *43* (4), 356-363.

54. Tian, G. X.; Moosmuller, H.; Arnott, W. P., Simultaneous Photoacoustic Spectroscopy of Aerosol and Oxygen A-Band Absorption for the Calibration of Aerosol Light Absorption Measurements. *Aerosol Science and Technology* **2009,** *42* (11), 1084-1090.

55. Luft, K. F.; Schaefer, W.; Wiegleb, G., 50 Years Ndir Gas-Analysis. *Technisches Messen* **1993,** *60* (10), 363-371.

56. Feher, M.; Martin, P. A., Tunable Diode-Laser Monitoring of Atmospheric Trace Gas Constituents. *Spectrochimica Acta Part a-Molecular and Biomolecular Spectroscopy* **1995,** *51* (10), 1579-1599; Linnerud, I.; Kaspersen, P.; Jaeger, T., Gas Monitoring in the Process Industry Using Giode Laser Spectroscopy. *Applied Physics B* **1998,** *67*, 297-305; Werle, P., A Review of Recent Advances in Semiconductor Laser based Gas Monitors. *Spectrochimica Acta A* **1998,** *54*, 197-236.

57. Lehmann, K. K. 1996; Romanini, D.; Gambogi, J.; Lehmann, K. K., Cavity Ring Down Spectroscopy With CW Diode Laser Excitation. In *50th International Symposium on Molecular Spectroscopy*, Miller, T. A., Ed. 1995; Romanini, D.; Kachanov, A. A.; Sadeghi, N.; Stoeckel, F., CW cavity ring down spectroscopy. *Chemical Physics Letters* **1997,** *264* (3-4), 316-322; Romanini, D.; Kachanov, A. A.; Stoeckel, F., Diode laser cavity ring down spectroscopy. *Chemical Physics Letters* **1997,** *270* (5-6), 538-545.

58. O'Keefe, A.; Scherer, J. J.; Paul, J. B., cw Integrated cavity output spectroscopy. *Chemical Physics Letters* **1999,** *307* (5-6), 343-349.

59. Arnott, W. P.; Moosmuller, H.; Sheridan, P. J.; Ogren, J. A.; Raspet, R.; Slaton, W. V.; Hand, J. L.; Kreidenweis, S. M.; Collett, J. L., Photoacoustic and filter-based ambient aerosol light absorption measurements: Instrument comparisons and the role of relative humidity. *Journal of Geophysical Research-Atmospheres* **2003,** *108* (D1); Lewis, K.; Arnott, W. P.; Moosmuller, H.; Wold, C. E., Strong spectral variation of biomass smoke light absorption and single scattering albedo observed with a novel dual-wavelength photoacoustic instrument. *Journal of Geophysical Research-Atmospheres* **2008,** *113* (D16).

60. Lack, D. A.; Lovejoy, E. R.; Baynard, T.; Pettersson, A.; Ravishankara, A. R., Aerosol absorption measurement using photoacoustic spectroscopy: Sensitivity, calibration, and uncertainty developments. *Aerosol Science and Technology* **2006,** *40* (9), 697-708.

61. Lack, D. A.; Cappa, C. D.; Cross, E. S.; Massoli, P.; Ahern, A. T.; Davidovits, P.; Onasch, T. B., Absorption Enhancement of Coated Absorbing Aerosols:

Validation of the Photo-Acoustic Technique for Measuring the Enhancement. *Aerosol Science and Technology* **2009,** *43* (10), 1006-1012.

62. Gyawali, M.; Arnott, W. P.; Lewis, K.; Moosmuller, H., In situ aerosol optics in Reno, NV, USA during and after the summer 2008 California wildfires and the influence of absorbing and non-absorbing organic coatings on spectral light absorption. *Atmospheric Chemistry and Physics* **2009,** *9* (20), 8007-8015.

63. Massoli, P.; Murphy, D. M.; Lack, D. A.; Baynard, T.; Brock, C. A.; Lovejoy, E. R., Uncertainty in Light Scattering Measurements by TSI Nephelometer: Results from Laboratory Studies and Implications for Ambient Measurements. *Aerosol Science and Technology* **2009,** *42* (11), 1064-1074.

64. Adams, K. M.; Davis, L. I.; Japar, S. M.; Pierson, W. R., Real-Time, Insitu Measurements of Atmospheric Optical-Absorption in the Visible Via Photoacoustic-Spectroscopy .2. Validation for Atmospheric Elemental Carbon Aerosol. *Atmospheric Environment* **1989,** *23* (3), 693-700.

65. Orphal, J., A critical review of the absorption cross-sections of O-3 and NO2 in the ultraviolet and visible. *Journal of Photochemistry and Photobiology a-Chemistry* **2003,** *157* (2-3), 185-209.

66. Robichaud, D. J.; Hodges, J. T.; Brown, L. R.; Lisak, D.; Maslowski, P.; Yeung, L. Y.; Okumura, M.; Miller, C. E., Experimental intensity and lineshape parameters of the oxygen A-band using frequency-stabilized cavity ring-down spectroscopy. *Journal of Molecular Spectroscopy* **2008,** *248* (1), 1-13.

67. Havey, D. K.; Long, D. A.; Okumura, M.; Miller, C. E.; Hodges, J. T., Ultra-sensitive optical measurements of high-J transitions in the O-2 A-band. *Chemical Physics Letters* **2009,** *483* (1-3), 49-54.

68. Kosterev, A. A.; Mosely, T. S.; Tittel, F. K., Impact of humidity on quartz-enhanced photoacoustic spectroscopy based detection of HCN. *Applied Physics B-Lasers and Optics* **2006,** *85* (2-3), 295-300; Wysocki, G.; Kosterev, A. A.; Tittel, F. K., Influence of molecular relaxation dynamics on quartz-enhanced photoacoustic detection of CO2 at lambda=2 mu m. *Applied Physics B-Lasers and Optics* **2006,** *85* (2-3), 301-306; Schilt, S.; Besson, J. P.; Thevenaz, L., Near-infrared laser photoacoustic detection of methane: the impact of molecular relaxation. *Applied Physics B-Lasers and Optics* **2006,** *82* (2), 319-328; Hammerich, M.; Olafsson, A.; Henningsen, J., Photoacoustic Study of Kinetic Cooling. *Chemical Physics* **1992,** *163* (2), 173-178.

69. Schafer, S.; Miklos, A.; Hess, P., Quantitative signal analysis in pulsed resonant photoacoustics. *Applied Optics* **1997,** *36* (15), 3202-3211.

70. Galatry, L., Simultaneous Effect of Doppler and Foreign Gas Broadening on Spectral Lines. *Physical Review* **1961,** *122* (4), 1218-&.

71. Wiedensohler, A., An Approximation of the Bipolar Charge-Distribution for Particles in the Sub-Micron Size Range. *Journal of Aerosol Science* **1988,** *19* (3), 387-389.

72. Mulholland, G. W.; Donnelly, M. K.; Hagwood, C. R.; Kukuck, S. R.; Hackley, V. A.; Pui, D. Y. H., Measurement of 100 nm and 60 nm particle standards by differential mobility analysis. *Journal of Research of the National Institute of Standards and Technology* **2006,** *111* (4), 257-312.

73. Pushkarsky, M. B.; Webber, M. E.; Patel, C. K. N., Ultra-sensitive ambient ammonia detection using CO2-laser-based photoacoustic spectroscopy. *Applied Physics B-Lasers and Optics* **2003,** *77* (4), 381-385.
74. Miklos, A.; Pei, S. C.; Kung, A. H., Multipass acoustically open photoacoustic detector for trace gas measurements. *Applied Optics* **2006,** *45* (11), 2529-2534.
75. Hodges, J. T.; Layer, H. P.; Miller, W. W.; Scace, G. E., Frequency-stabilized single-mode cavity ring-down apparatus for high-resolution absorption spectroscopy. *Review of Scientific Instruments* **2004,** *75* (4), 849-863.
76. Xue, H. X.; Khalizov, A. F.; Wang, L.; Zheng, J.; Zhang, R. Y., Effects of dicarboxylic acid coating on the optical properties of soot. *Physical Chemistry Chemical Physics* **2009,** *11* (36), 7869-7875; Xue, H. X.; Khalizov, A. F.; Wang, L.; Zheng, J.; Zhang, R. Y., Effects of Coating of Dicarboxylic Acids on the Mass-Mobility Relationship of Soot Particles. *Environmental Science & Technology* **2009,** *43* (8), 2787-2792.
77. Shiraiwa, M.; Kondo, Y.; Iwamoto, T.; Kita, K., Amplification of Light Absorption of Black Carbon by Organic Coating. *Aerosol Science and Technology* **2010,** *44* (1), 46-54.
78. Nagele, M.; Sigrist, M. W., Mobile laser spectrometer with novel resonant multipass photoacoustic cell for trace-gas sensing. *Applied Physics B-Lasers and Optics* **2000,** *70* (6), 895-901; Rey, J. M.; Marinov, D.; Vogler, D. E.; Sigrist, M. W., Investigation and optimisation of a multipass resonant photoacoustic cell at high absorption levels. *Applied Physics B-Lasers and Optics* **2005,** *80* (2), 261-266.
79. Jacobson, M. Z., Strong radiative heating due to the mixing state of black carbon in atmospheric aerosols. *Nature* **2001,** *409* (6821), 695-697.
80. IPCC, *Climate Change 2007: The Physical Science Basis. Contribution of Working Group I to the Fourth Assessment Report of the Intergovernmental Panel on Climate Change*. Cambridge University Press: Cambridge, 2009.
81. Schmid, O.; Schaniter, M.; Andeae, M. O.; Linke, C.; Moehler, O.; Saathoff, H.; Schoeck, W.; Wagner, U., Absorption Properties of Black Carbon with Refractive Coatings: Intercomparison of Different Instruments. *Geophysical Research Abstracts* **2004,** *6*.
82. Net, S.; Nieto-Gligorovski, L.; Gligorovski, S.; Temime-Rousell, B.; Barbati, S.; Lazarou, Y. G.; Wortharn, H., Heterogeneous light-induced ozone processing on the organic coatings in the atmosphere. *Atmospheric Environment* **2009,** *43* (9), 1683-1692.
83. Hallett, J.; Hudson, J. G.; Rogers, C. F., CHARACTERIZATION OF COMBUSTION AEROSOLS FOR HAZE AND CLOUD FORMATION. *Aerosol Science and Technology* **1989,** *10* (1), 70-83; Schumann, U.; Strom, J.; Busen, R.; Baumann, R.; Gierens, K.; Krautstrunk, M.; Schroder, F. P.; Stingl, J., In situ observations of particles in jet aircraft exhausts and contrails for different sulfur-containing fuels. *Journal of Geophysical Research-Atmospheres* **1996,** *101* (D3), 6853-6869; Saathoff, H.; Naumann, K. H.; Schnaiter, M.; Schock, W.; Mohler, O.; Schurath, U.; Weingartner, E.; Gysel, M.; Baltensperger, U., Coating of soot and (NH4)(2)SO4 particles by ozonolysis products of alpha-pinene. *Journal of Aerosol Science* **2003,** *34* (10), 1297-1321.

84. Gangopadhyay, S., I. Elminyawi and C. M. Sorenson, Optical structure factor measurements of soot particles in a premixed flame. *Applied Optics* **1991,** *30* (33), 4859-4864.

85. Seinfeld, J. H., Pandis, S.N., *Atmospheric Chemistry and Physics: From Air Pollution to Climate Change*. John Wiley & Sons, Inc.: New York, 1998.

86. Chang, S. G., Chemical and Catalytic Properties of Elemental Carbon. In *Particulate Carbon: Atmospheric Life Cycle*, Wolff, G. T. a. K., R.L., Ed. Plenum Press: New York, 1982; pp 158-181.

87. Jacobson, M. Z., Strong radiative heating due to the mixing state of black carbon in atmospheric aerosols. **2001,** *409* (6821), 695-697.

88. Kim, S. H.; Fletcher, R. A.; Zachariah, M. R., Understanding the difference in oxidative properties between flame and diesel soot nanoparticles: The role of metals. *Environmental Science & Technology* **2005,** *39* (11), 4021-4026.

89. Park, K.; Cao, F.; Kittelson, D. B.; McMurry, P. H., Relationship between particle mass and mobility for diesel exhaust particles. *Environmental Science & Technology* **2003,** *37* (3), 577-583.

90. Farias, T. L.; Koylu, U. O.; Carvalho, M. G., Range of validity of the Rayleigh-Debye-Gans theory for optics of fractal aggregates. *Applied Optics* **1996,** *35* (33), 6560-6567.

91. Zhu, J. Y.; Choi, M. Y.; Mulholland, G. W.; Manzello, S. L.; Gritzo, L. A.; Suo-Antila, J., Measurement of visible and near-IR optical properties of soot produced from laminar flames. *Proceedings of the Combustion Institute* **2002,** *29*, 2367-2374.

92. Mullins, J.; Williams, A., The Optical Properties of Soot: A Comparison Between Experimental and Theoretical Values. *Fuel* **1987,** *66* (2), 277-280.

93. Choi, M. Y.; Mulholland, G. W.; Hamins, A.; Kashiwagi, T., Comparison of the Soot Volume Fraction using Gravimetric and Light Extinction Techniques. *Combustion and Flame* **1995,** *102* (1-2), 161-169.

94. Carslaw, H. S.; Jaeger, J. C., *Conduction of Heat in Solids*. Second ed.; Clarendon Press: Oxford, 1959.

95. Friedlander, S. K., *Smoke, Dust and Haze: Fundamentals of Aerosol Behavior*. John Wiley & Sons: New York, 1977; p 317.

96. Bond, T. C.; Bergstrom, R. W., Light absorption by carbonaceous particles: An investigative review. *Aerosol Science and Technology* **2006,** *40* (1), 27-67.

97. Slowik, J. G.; Cross, E. S.; Han, J. H.; Kolucki, J.; Davidovits, P.; Williams, L. R.; Onasch, T. B.; Jayne, J. T.; Kolb, C. E.; Worsnop, D. R., Measurements of morphology changes of fractal soot particles using coating and denuding experiments: Implications for optical absorption and atmospheric lifetime. *Aerosol Science and Technology* **2007,** *41* (8), 734-750.

98. Choi, M. Y.; Mulholland, G. W.; Hamins, A.; Kashiwagi, T., COMPARISONS OF THE SOOT VOLUME FRACTION USING GRAVIMETRIC AND LIGHT EXTINCTION TECHNIQUES. *Combustion and Flame* **1995,** *102* (1-2), 161-169.

99. Park, K.; Kittelson, D. B.; McMurry, P. H., Structural properties of diesel exhaust particles measured by transmission electron microscopy (TEM):

Relationships to particle mass and mobility. *Aerosol Science and Technology* **2004,** *38* (9), 881-889.
100. Friedlander, S. K., *Smoke, Dust and Haze: Fundamentals of Aerosol Behavior*. Second ed.; Oxford University Press: New York, 2000; p 407.